Crustal Velocity Structure of the Southern Nechako Basin, British Columbia, from Wide-Angle Seismic Traveltime Inversion

by

Andrew Stephenson
BSc, University of Victoria, 2008

A Thesis Submitted in Partial Fulfillment
of the Requirements for the Degree of

MASTER OF SCIENCE

in the School of Earth and Ocean Sciences

Supervisory Committee

Crustal Velocity Structure of the Southern Nechako Basin, British Columbia, from Wide-Angle Seismic Traveltime Inversion

by

Andrew Stephenson
BSc, University of Victoria, 2008

Supervisory Committee

Dr. George D. Spence, (School of Earth and Ocean Sciences)
Supervisor

Dr. John F. Cassidy (School of Earth and Ocean Sciences; Geological Survey of Canada)
Departmental Member

Dr. Stan E. Dosso (School of Earth and Ocean Sciences)
Departmental Member

Abstract

Supervisory Committee
Dr. George D. Spence, (School of Earth and Ocean Sciences)
Supervisor
Dr. John F. Cassidy (School of Earth and Ocean Sciences; Geological Survey of Canada)
Departmental Member
Dr. Stan E. Dosso (School of Earth and Ocean Sciences)
Departmental Member

In the BATHOLITHS*onland* seismic project, a refraction - wide-angle reflection survey was shot in 2009 across the Coast Mountains and Interior Plateau of central British Columbia. Part of the seismic profile crossed the Nechako Basin, a Jurassic-Cretaceous basin with potential for hydrocarbons within sedimentary rocks that underlie widespread volcanics. Along this 205-km-long line segment, eight explosive shots averaging 750 kg were fired and recorded on 980 seismometers. Forward and inverse modelling of the traveltime data were conducted with two independent methods: ray-tracing based modelling of first and secondary arrivals, and a higher resolution wavefront-based first-arrival seismic tomography. Gravity modelling was utilized as a means of evaluating the density structure corresponding to the final velocity model.

Material with velocities less than 5.0 km/s is interpreted as sedimentary rocks of the Nechako Basin, while velocities from 5.0-6.0 km/s may correspond to interlayered sediments and volcanics. The greatest thickness of sedimentary rocks in the basin is found in the central 110 km of the profile. Two sub-basins were identified in this region, with widths of 20-50 km and maximum sedimentary depths of 2.5 km and 3.3 km. Such features are well-defined in the velocity model, since resolution tests indicate that features with widths greater than ~13 km are reliable. Beneath the sedimentary rocks,

seismic velocities increase more slowly with depth – from 6.0 km/s just below the basin to 6.3 km/s at ~17 km depth, and then to 6.8-7.0 km/s at the base of the crust. The Moho is interpreted at a depth of 33.5-35 km along the profile, and mantle velocities are high at 8.05-8.10 km/s.

Table of Contents

List of Tables

List of Figures

Acknowledgments

I would like to thank my supervisor Dr. George Spence for providing me with the opportunity to be involved with such a comprehensive and interesting geoscience project, as well as for his continual support and direction over the past two years.

I would also like to thank the members of my committee, Dr. John Cassidy and Dr. Stan Dosso, for helping to guide the direction of my research, while providing valuable input and encouragement. Thanks to Dr. John Hole and Dr. Ron Clowes for taking the time to review the initial manuscript. I would like to thank my external examiner, Dr. Andy Calvert, as well as the many friendly and helpful people I have met within the School of Earth and Ocean Sciences.

The BATHOLITHS*onland* seismic survey was funded by grants to Dr. George Spence and Dr. Ron Clowes from the Natural Sciences and Engineering Research Council (NSERC) in Canada and to Dr. John Hole and Dr. Kate Miller from the Continental Dynamics Program of the National Science Foundation (NSF) in the USA. We gratefully acknowledge the Incorporated Research Institutes for Seismology (IRIS/PASSCAL) for providing the seismic instruments and for the expertise in managing this equipment. Thanks to the numerous contractors involved with explosives, boats, drilling, and storage facilities, as well as First Nations and government agencies for use of the land. Finally, thanks to the many volunteers who were integral to the successful acquisition of these large amounts of data in the field.

Dedication

This thesis is dedicated to my Grandma Eileen, who instilled in me the value of education while providing moral and financial support, and a constant source of motivation.

Chapter 1 Introduction

1.1 Purpose and Objectives

The BATHOLITHS*onland* seismic survey, presented in this paper, represents a key seismic component of the BATHOLITHS program, an interdisciplinary earth science study aimed at understanding the processes behind the formation of continental crust.

When continental crust such as the Coast Mountain Batholith is fully formed, it is andesitic or felsic in composition. This is in strong contrast to the character of the mafic melt in the mantle beneath the arc, from which it is derived. It is believed that a magmatic differentiation process takes place during the generation of the crust above subduction zones, with an ultramafic residue being extracted and leading to the observed intermediate-felsic crustal composition (Ducea, 2002; Zandt et al., 2004). Exactly what happens to this residual ultramafic material is uncertain, although due to its high density it is eventually likely to delaminate from the base of the crust via a combined dripping and peeling process (Zandt et al., 2004). Examining the nature of the Moho discontinuity beneath the Coast Mountain Belt (Fig. 1.1) by means of wide-angle seismic refraction and reflection data should give some indication as to the presence, or absence, of this leftover material and its character. This, in conjunction with other geophysical, geological and geochemical studies of the BATHOLITHS project, should provide a "snapshot" of a stage in the production of continental crust, and hence reveal some of the complex mechanisms involved in its formation.

The 400-km-long BATHOLITHS*onland* seismic survey, acquired in the summer of 2009, crossed the Coast Mountains and Interior Plateau (Fig. 1.2). We focus only on

the eastern 205 km of the seismic profile, which crosses the Nechako Basin within the Intermontane Belt (Fig. 1.3). Chilcotin forestry along this part of the survey line has been negatively impacted by the effects of the Mountain Pine Beetle, and as a result, recent research has focused on evaluation of potential petroleum and mineral resources within the Nechako Basin. The primary goal of our study is to build a well-resolved seismic velocity model that delineates the subsurface extent of sedimentary rock and provides the structural framework for the formation of the Nechako Basin. By doing so, we will also provide upper-crustal constraints for subsequent velocity modelling of full-line data beneath the Coast Mountain Batholith.

1.2 Geology

1.2.1 Regional Tectonics

The Intermontane Belt is a large geological superterrane within the Western Canadian Cordillera. It is primarily composed of three tectonostratigraphic accreted terranes: the Stikine and Quesnel volcanic arc terranes, and the oceanic Cache Creek Terrane (Fig. 1.1*a*). The terranes represent a fault-bounded assortment of oceanic, island-arc, foredeep, and clastic wedge assemblages (Gabrielse et al., 1991), enigmatic because of their contrasting faunal and lithologic nature relative to that of continental North America (Jackson et al., 1991).

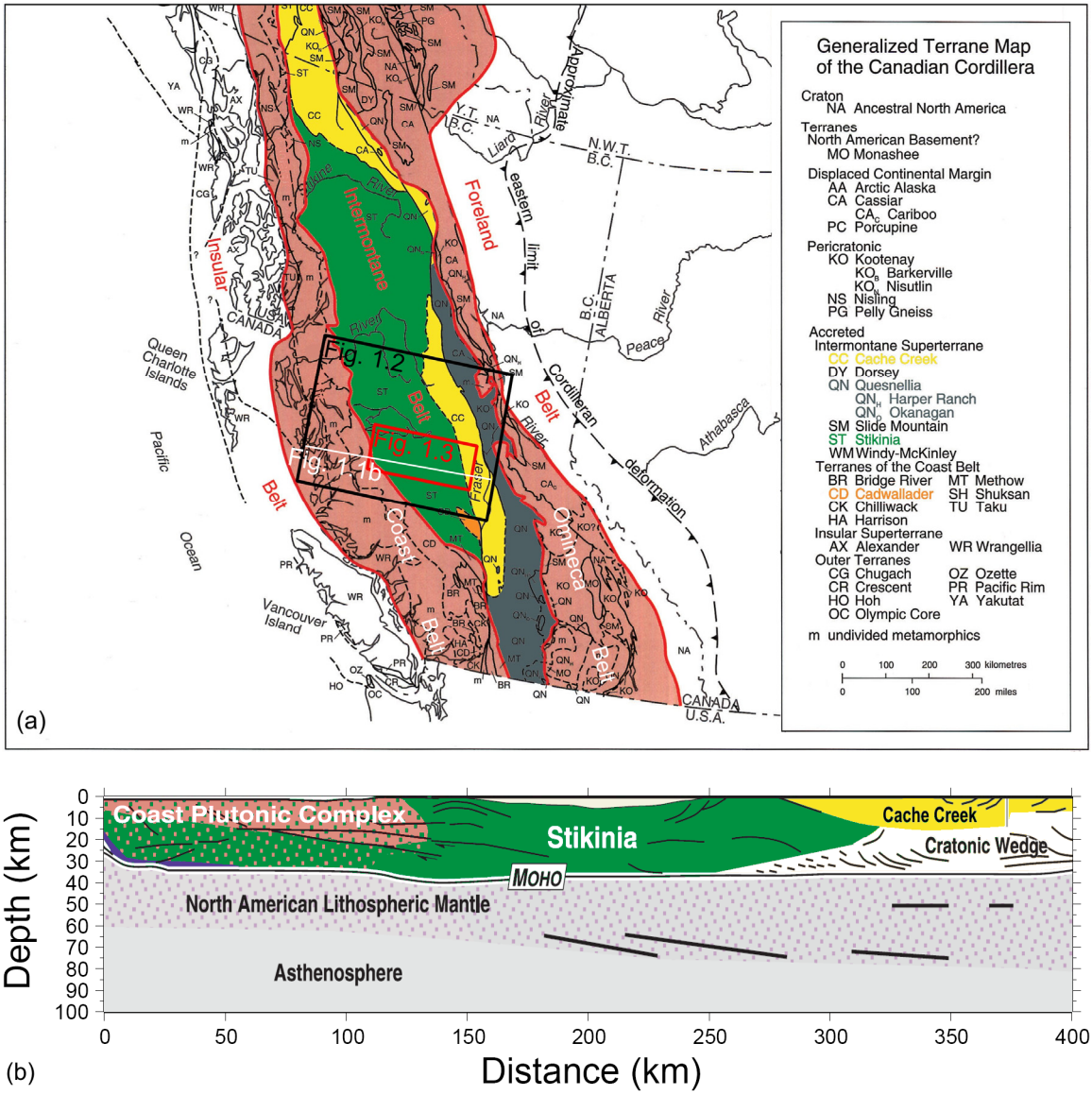

Figure 1.1. (*a)* Morphogeological belts and terranes of the Canadian Cordillera (modified from Gabrielse and Yorath, 1989; Wheeler et al., 1991). The Coast Belt, Intermontane Belt, and Omineca Belt are given in colour. Black and red boxes indicate the survey location, corresponding to Figure 1.2 and Figure 1.3, respectively. The white line corresponds to the approximate location of *(b)*, a simplified depth profile across the terranes of this study (modified from Hammer and Clowes, 2004). Colour-coded terranes within the Intermontane Belt include the Stikine (ST - green), Cache Creek (CC - yellow), Quesnel (QN – blue), and Cadwallader (CD - orange).

The Stikine Terrane is the largest of the exotic terranes within the Western Canadian Cordillera. It is defined by a Carboniferous volcanic island-arc basement underlying Middle-Late Triassic Lewes River volcanic arc (Harris et al., 1998). Above, two sedimentary packages representing up to 7 km of strata were accumulated in the Whitehorse Trough marginal basin, with Lewes River Group volcanics and carbonates underlying intrusive-loaded clastics of the Jurassic Laberge Group (Hart, 1996). Early Jurassic ammonite fauna of Tethyan origin suggest that the Stikine Terrane evolved in the East Pacific, and moved northward to collide with North America in the Middle Jurassic (MacIntyre et al., 2001). The Stikine Terrane is inferred to comprise the entire ~35 km thickness of the continental crust (Fig. 1.1*b*) in the northern Cordillera (Cook et al., 2004).

The Cache Creek Terrane is interpreted as an oceanic crustal and accretionary complex generally defined by ultramafic, metavolcanic, and metasedimentary rocks (MacIntyre et al., 2001). Melange belts, mafic plutonic complexes, and large sequences of intact shallow water reef-derived carbonates highlight the geological variety encompassed by the assemblage (Johnston and Borel, 2007). Geology of the Cache Creek Terrane is dominated by the Cache Creek Complex, which includes Carboniferous to Early Jurassic chert, siltstone, limestone, metabasalt, ultramafite, and gabbroic intrusives. These units, as well as Late Permian to Early Triassic metavolcanic and metaplutonic rocks are overlain by the Sitlika assemblage consisting of Late Triassic to Early Jurassic clastics (MacIntyre et al., 2001). Permian limestone bearing fauna of exotic Tethyan affinity suggest that the Cache Creek Terrane may include components which originated a great distance from their final accreted location (Jackson et al., 1991). Specifically, the terrane consists of accreted seamounts and oceanic plateaus encircled by

carbonate reefs, originating on the opposite side of the Panthalassic Ocean, within or adjacent to the Tethys Ocean (Johnston and Borel, 2007). The Cache Creek Terrane is comparatively thin relative to the Stikine Terrane (Fig. 1.1*b*), with an estimated thickness of ~7.5 km (Evenchick et al., 2007).

Oceanic crust of the Cache Creek Terrane is bounded on either side by the Stikine and Quesnel volcanic arc terranes (Fig. 1.1*a*). The Stikine and Quesnel terranes are interpreted to have originated in the Paleozoic-Early Mesozoic as a unified volcanic arc located east of the Cache Creek Terrane (Johnston and Borel, 2007). The Cache Creek Terrane, being overthrust by the Stikine volcanic arc terrane, is interpreted to represent the accretionary wedge that formed during eastward subduction beneath the arc (Johnston and Borel, 2007). Relocation of the Stikine Terrane to the western margin of the Cache Creek Terrane is thought to have transpired via strike-slip faulting or oroclinal bending during syn- to post-accretion deformation (Johnston and Borel, 2007). Amalgamation of the terranes to form the primitive Intermontane Belt is estimated to have occurred in the Early Mesozoic, around 210 Ma. It is inferred that the loosely-joined terranes were carried east to southeast across the Pacific, through the Jurassic, by the Farallon Plate, at which point the Pacific Plate fractured and the terranes moved northward obliquely into the North American craton (Harris et al., 1998). Eastward thrusting at 175 Ma juxtaposed the newly-formed belt to the western margin of the craton (Monger et al., 1982). It is suggested that the amalgamated terranes composing the Intermontane Belt are best characterized as a coherent microplate, having behaved as such since the Early Jurassic (Johnston and Borel, 2007).

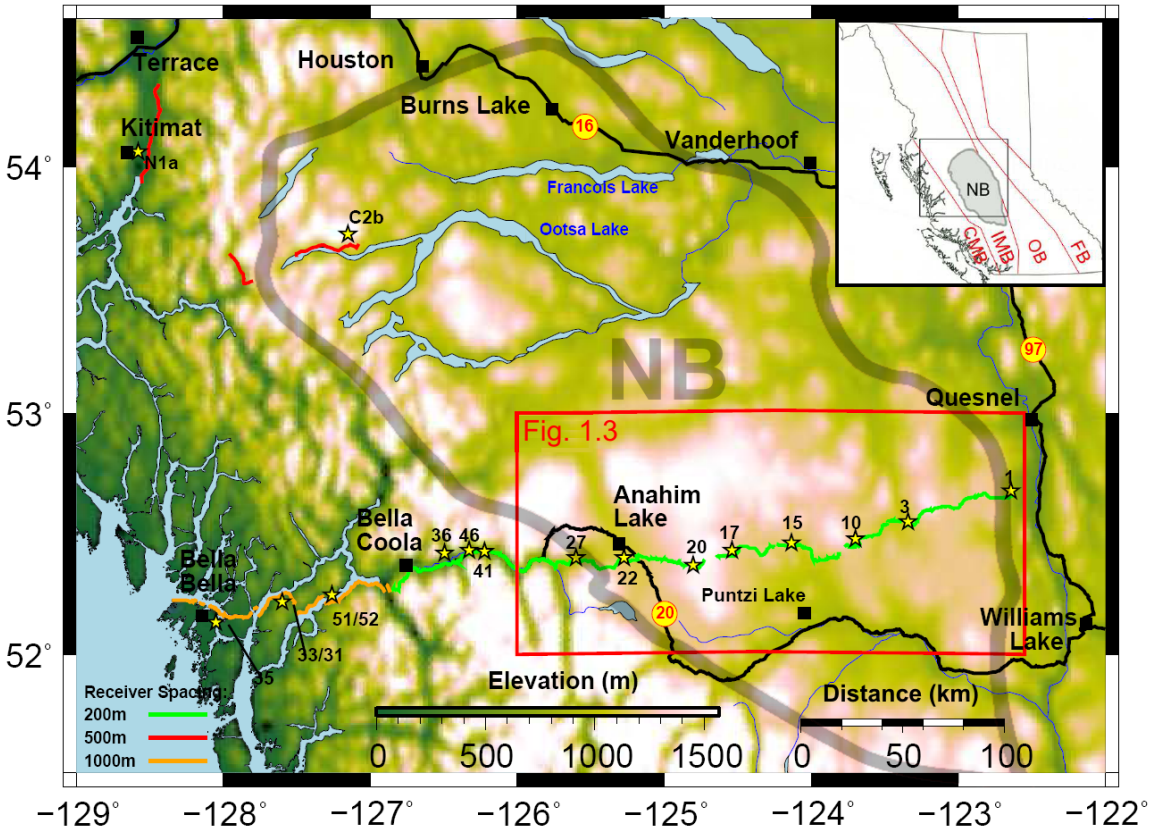

Figure 1.2. Topographical map showing the location of the BATHOLITHS*onland* refraction/wide-angle reflection profile. The numbered stars are shot sites, and the green, red and orange lines indicate the receiver profiles. The red box corresponding to Figure 1.3 indicates the region where seismic structure is interpreted in the current study. The gray polygon delineates the approximate extent of the Nechako Basin (BC Ministry of Energy, Mines and Petroleum Resources, 2002). Inset shows morphological belts of the Canadian Cordillera, and the location of the Nechako Basin. NB, Nechako Basin; CMB, Coast Mountain Belt; IMB, Intermontane Belt; OB, Omineca Belt; FB, Foreland Belt.

Dominant structures within the Intermontane Belt are described by subduction zone deformation regimes, typified by accretionary wedges from the Early Mesozoic. Block faulting from the same time period, as well as later arc volcanism, characterize much of the Stikine Terrane (Gabrielse et al., 1991). Most deformation within the Intermontane Belt occurred during the Middle-Late Jurassic terrane juxtaposition. Through the late Mesozoic to Early Cenozoic time, folding resulting from uplift of the adjacent Coast and Omineca belts, as well as dextral strain regimes, define structure of

the belt (Gabrielse et al., 1991). Rocks of the Stikine Terrane exhibit wide-open fold patterns, with deformation increasing with increased proximity to the Cache Creek Terrane boundary, a zone of thrust faulting which occurred prior to 165 Ma (MacIntyre et al., 2001).

1.2.2 The Nechako Basin

The Nechako Basin is a large Jurassic-Cretaceous forearc sedimentary basin within the Intermontane Belt of British Columbia (Fig. 1.2). Following the accretion of the Intermontane Belt in the mid Jurassic, thrust faulting coincided with the transpressional beginnings of basin formation. This contraction produced uplift and erosion, supplying sedimentary infill to what would become the depocentre (Gabrielse et al., 1991). Extensional tectonics took over in the Eocene, producing a number of segmented sub-basins – possibly including remnants of the Mesozoic paleobasin - separated by north to northwest trending strike-slip faults (Hayward and Calvert, 2010*b*). These Eocene sedimentary sub-basins are interpreted to dominate the modern-day extent of what is referred to in this paper as the Nechako Basin, with much of the larger paleobasin likely having been removed by shortening (A.J. Calvert, personal communication, 2010). Widespread Eocene-Neogene volcanism resulted in a layer of volcanic cover over large amounts of the Nechako Basin (Hayward and Calvert, 2010*b*). Much of the volcanics were subsequently buried by Quaternary till (Fig. 1.3).

The south-central part of the basin is bounded by the Omineca Crystalline Belt to the east and the Coast Plutonic Complex of the Coast Mountain Belt to the west (Fig. 1.2). Sedimentary rock exposed within this part of the basin includes Cretaceous

sandstones and conglomerates of the Taylor Creek Group (Fig. 1.3). Potentially hydrocarbon-bearing Jurassic-Cretaceous clastic sedimentary rock is observed at a limited number of outcrops and is expected to underlie the surface cover, although its exact spatial extent is not well known (Calvert et al., 2009). These units represent the best potential reservoir in the Nechako Basin (Osadetz et al., 2007).

The Nechako Basin has seen limited petroleum exploration over the past 80 years, consisting of 12 exploratory wells drilled from 1931 to 1986 (Osadetz et al., 2007). In addition, 1300 line-kilometres of reflection seismic data were shot by Canadian Hunter in the 1980's, supplemented by 330 line-kilometres acquired by Geoscience BC in 2008 (Calvert et al., 2009). Exploration has been hampered by both poor documentation of borehole and outcrop data, and complex structural relationships among prospective units (Riddell, 2009). Quaternary glacial till, which covers much of the basin and limits surface exposures, further impedes geological mapping. Borehole oil staining and gas observed in drill stem tests confirm the presence of hydrocarbons, with maturation data indicating that Mid-Late Cretaceous units are found within the oil window. Both potential source rock and reservoir facies have been identified within Cretaceous sediments (BC Ministry of Energy, Mines and Petroleum Resources, 2002). Hannigan et al. (1994) estimated the total oil and gas potential for five conceptual plays of the Nechako region to be 5.10 billion barrels and 9.56 TCF, respectively, although these estimates are highly uncertain. Five additional speculative plays are described by geological information that is insufficient for developing an assessment of potential reserves (Hannigan et al., 1994).

1.2.3 Surface Geology

Present-day geology of the southern half of the frontier basin is dominated by layers of highly faulted Tertiary volcanic rock - the Eocene Endako and Ootsa Lake groups, and the Miocene-Pliocene Chilcotin Group basalts (Fig. 1.3).

The Eocene Endako Group (51-45 Ma) and Ootsa Lake Group (53-48 Ma) unconformably overlie the volcanic basement of the Stikine and Cache Creek terranes (MacIntyre et al., 2001). Geological mapping has revealed that the Endako Group consists of vesicular basaltic to andesitic flows containing tuff, breccia, and some sedimentary rocks (Riddell, 2006). Boreholes sample Endako Group with thicknesses ranging from 44-517 m. The Ootsa Lake Group also includes a wide range of lithologies, comprised of intermediate to felsic volcanic flows, with tuff, breccia, and sedimentary rocks (Riddell, 2006). A potential Ootsa Lake Group thickness of 477 m is pierced by borehole B-22-K (Hayward and Calvert, 2010*a*). Lack of a direct correlation between surface lithology and seismic reflection data, due to poor data quality, results in considerable variability in the estimated thickness and structure of the surface volcanics, as well as wide lithological variation within groups (Hayward and Calvert, 2010*a*).

The Neogene Chilcotin Group contains vesicular columnar olivine basalt, with flows, andesite, rhyolite ash, tuff, breccia, and sedimentary rocks (Riddell, 2006). Previously, Chilcotin Group basalts were generally interpreted to be several hundred metres thick, similar to the Eocene volcanics, as evidenced by borehole data. More recently, however, the volcanic packages are interpreted to be much thinner (~20-50 m) and less widely distributed than originally inferred (Fig. 1.3), although thick localized sections are observed to coincide with paleo-river valleys (Andrews and Russell, 2007).

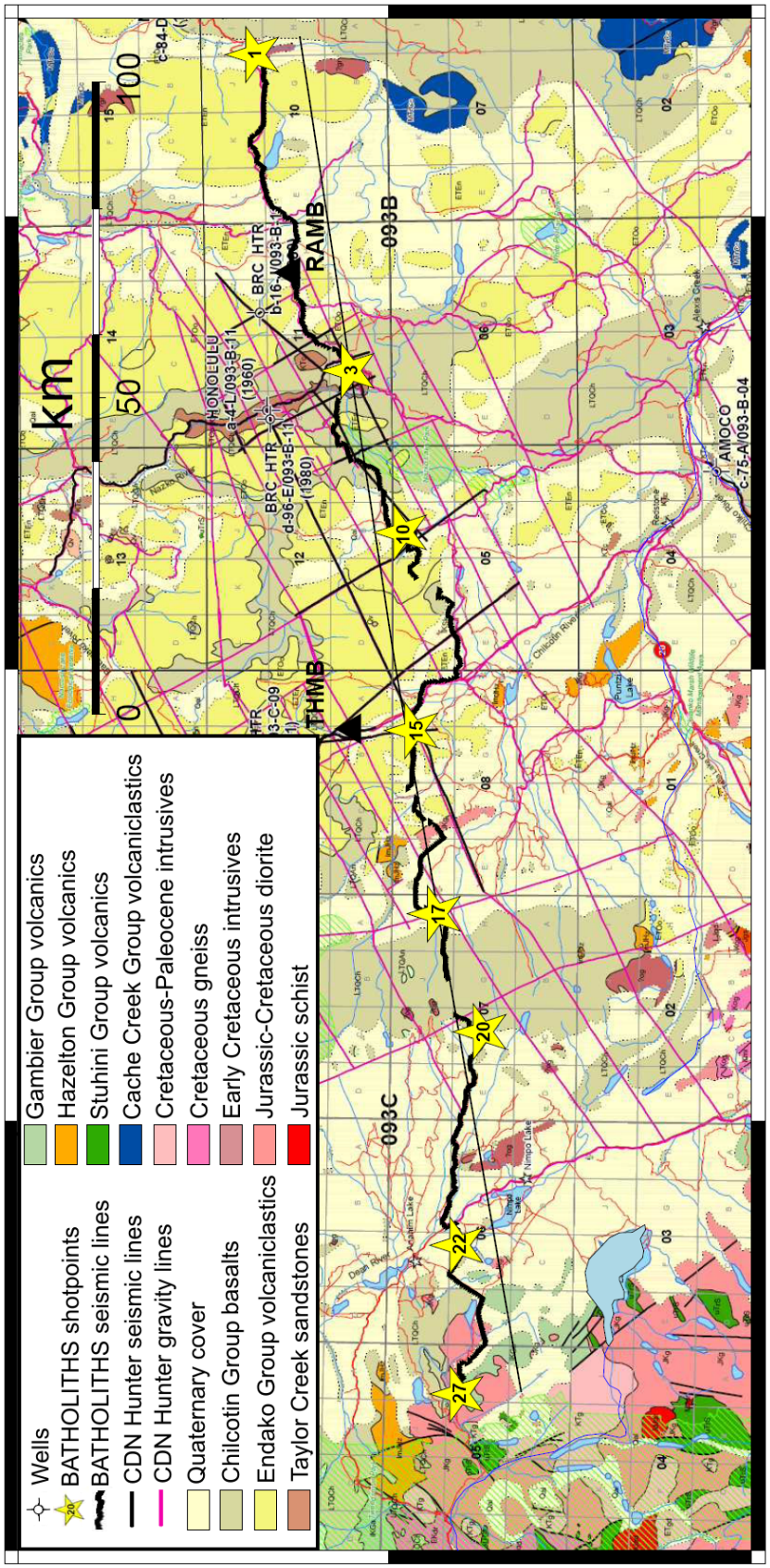

Figure 1.3. Comprehensive surface geology map including shotpoints and receiver lines of the BATHOLITHS*onland* survey analysed in this study (modified from Riddell, 2006).

The highly reflective character of extensive volcanic cover, and possible clastic interbedding can render standard seismic reflection methods ineffective at defining subsurface structure. Seismic refraction methods, such as those employed by this study, prove useful in such instances, enabling one to image under the volcanic blanket.

1.3 Other Geophysical Investigations

Although under-explored, the Intermontane Belt of the southern Canadian Cordillera has been the site of numerous past geophysical studies carried out both by research groups and by industry. These include, but are far from limited to, active and passive seismic surveys, potential field and magnetotelluric data acquisition, and analysis of near-surface rock properties via borehole logging. Coherent integration of the wide variety of datasets is necessary for revealing the full array of subsurface information which they contain.

1.3.1 Seismic Refraction

The first large-scale seismic refraction experiment conducted in the Western Canadian Cordillera was recorded from 1967 to 1971, although refraction studies had been undertaken as far back as 1953 (Berry and Forsyth, 1975). The survey consisted of seven long profiles located almost entirely within the Intermontane Belt. A Moho depth of 35 (±2) km and crustal velocity structure within the belt were interpreted by White et al. (1968) and Berry and Forsyth (1975).

Another early seismic experiment conducted within the Intermontane Belt consisted of a 440 km seismic refraction which was shot from 1973-1975, with its

western ~120 km transecting the Intermontane Belt in south-central British Columbia. Cumming et al. (1979) studied the lithospheric structure using ray tracing techniques, mapping the Moho at a depth of ~33 km and finding a close correlation between the shallow seismic velocity structure and regional geology.

More recently as part of the LITHOPROBE crustal research project, the 1989 and 1990 Southern Cordillera refraction experiments (SCoRE '89 and '90) included three transects which crossed the Intermontane Belt in the south-central part of the province. Zelt et al. (1992, 1996), Burianyk and Kanasewich (1995), and Spence and McLean (1998) discuss crustal velocity structure obtained by applying ray-tracing methodology to primary and secondary arrivals. The Moho depth was typically 34-35 km.

1.3.2 Seismic Reflection

Canadian Hunter Petroleum gathered seismic reflection data in the early 1980's across the southern Nechako Basin, although imaging was poor due to scattering of energy by near-surface volcanic layers. The 2D vibroseis data taken at maximum shot intervals of 100 m were recently reprocessed, resulting in enhanced coherency of sedimentary horizons, although near-surface resolution remains low (Hayward and Calvert, 2009*b*).

A 1988 component of the LITHOPROBE program included several reflection profiles within the Intermontane Belt, southeast of the Nechako Basin. An analysis and interpretation of the reflectivity features, including a distinctly imaged Moho, was detailed by Cook et al. (1992).

In 2008, a vibroseis reflection survey in the southern Nechako Basin was conducted by Geoscience BC. 330 line-kilometres of seismic reflection data at shot

intervals of 40 m were acquired as a complement to the pre-existing Canadian Hunter data. A tomographic inversion of first-arrivals and the derived shallow (<1 km) velocity structure are presented by Hayward and Calvert (2008, 2009*a*, 2010*a*), and Smithyman and Clowes (2010).

1.3.3 Passive Source Seismology

Wickens (1977) recorded seismic events with a network that included several stations within the Intermontane Belt. Rayleigh and Love surface wave arrival times were used to generate shear wave velocity-depth profiles averaged over each inter-station segment.

In 2006, a passive-source seismic investigation took place in the Nechako Basin with the goal of evaluating the hydrocarbon and mineral potential of the region. The network consisted of seven seismic stations which recorded large distant earthquakes, with a receiver function analysis being used to produce site-specific shear-wave velocity-depth profiles (Kim et al., 2009). Estimates of surface volcanic, sedimentary layer, and crustal thickness were made by Idowu (2009) and Cassidy et al. (2010) using ambient noise tomography.

1.3.4 Gravity

Initial gravity mapping of the southern Cordillera was presented by Stacey (1973). Bouguer anomaly data were used to estimate crustal thickness for a transect across southern British Columbia, including the Intermontane Belt. 3000 line-kilometres of gravity data were acquired by Canadian Hunter in 1981, to coincide with and

complement seismic reflection data in the Nechako Basin (Calvert et al., 2009). Recently, Geoscience BC's QUEST Project has collected airborne gravity data of the Cache Creek and Quesnel terranes of the Intermontane Belt, with a goal of encouraging mineral exploration. Gridded gravity data also exists in the Geoscience Data Repository of Natural Resources Canada, including the entire region at 2 km spacing, compiled from gravity observations acquired between 1944 and 2005.

1.3.5 Magnetotelluric

Magnetotelluric methods can map subsurface conductivity, as an indicator of basin thickness and extent. Twenty-year-old data were re-interpreted by Spratt et al. (2007), with the Nechako Basin and Cache Creek Terrane being delineated by zones of high and low conductivity, respectively. Even thin surface volcanic layers can be imaged using magnetotelluric techniques, indicated by a narrow zone of high resistivity from the surface to <200 m depth (Spratt et al., 2008). Greater porosity in the sedimentary basin rock contains more fluid content, giving higher conductivity, while the dense igneous basement rock and surface volcanics are much more resistive.

A magnetotelluric survey consisting of 7 profiles representing 300 km of data within the Nechako Basin was conducted in 2007. The survey aimed to characterize the conductivity structure of the basin, and evaluate the applicability of the method in petroleum exploration (Spratt and Craven, 2009). Spratt and Craven (2009) concluded that the magnetotelluric method was sensitive to the base of the sedimentary basin, and capable of defining its structural boundaries.

1.3.6 Borehole and Geological Mapping

Boreholes within the Nechako Basin date back to 1931, with several drilled through the 1950's, 1960's, and 1970's. In the 1980's, Canadian Hunter Petroleum drilled five wells within the basin as part of an exploration program that included seismic and gravity data (Calvert et al., 2009). Coincidence of borehole locations and seismic reflection profiles permitted correlation between horizon markers in the seismic data and actual geological units.

Borehole sonic logs provide upper-crustal constraint for velocity models, while geological analysis reveals thickness and composition of geological units. Core data are also useful for assessing potential source and reservoir facies within the borehole (e.g. Riddell, 2009), and for tying subsurface structure to mapped outcrops. A limited number of boreholes fully penetrate the Nechako Basin sedimentary package, continuing into several hundred metres of underlying basement rock and providing firm control points to aid interpretation of the basin's structural boundaries elsewhere.

Chapter 2 Data

2.1 Acquisition

In the principal 400-km-long transect of BATHOLITHS*onland*, sixteen explosive shotpoints were discharged at fourteen locations (Fig. 1.2). Along the western ~100 km of the survey line, receivers were deployed along fiords by boat, at an average spacing of 1 km. Receivers comprising the eastern ~300 km of the survey line were deployed on land at a spacing of 200 m. A northern line segment consisting of two shotpoints and 104 receivers at 500 m spacing was also included in the survey (Fig. 1.2), to provide 3D structural control. This paper focuses solely on the eastern eight shots of the main transect (Fig. 2.1), detonated over 205 km at an average inter-shot spacing of 29 km. The seismic shotpoints located along this segment varied in size between 500 kg and 940 kg of explosives, buried in drill holes with a top depth near 15 m and a bottom depth ranging from 25 m to 46 m (Table 2.1).

Shots were recorded by 980 vertical-component seismometers at a spacing of 200 m, with 3-component instruments also included at a spacing of 2 km. In this study, only the vertical-component data are considered. Instrumentation consisted of RefTek RT125A (Texan) data loggers recording information from OYO Geospace GS-One and GS-One 3-C geophones. Although access was difficult and receivers were placed along many segments of rough logging roads, there were only two significant breaks in receiver coverage, measuring 5.5 km and 2.0 km in length (Fig. 2.1).

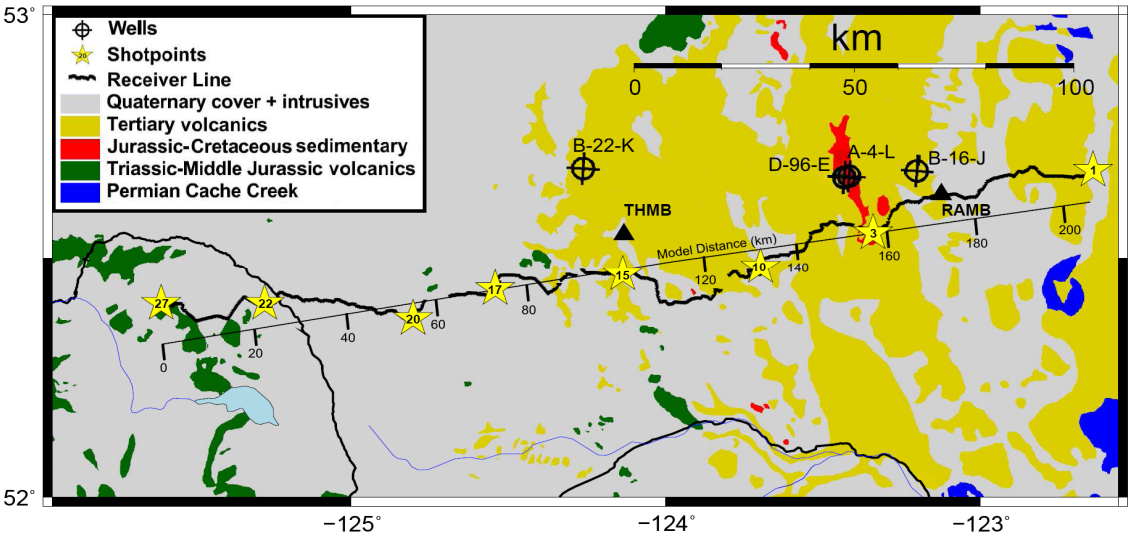

Figure 2.1. Geological map of the study area (modified from Hayes et al., 2003). Boreholes drilled in the early 1980's are labelled B-22-K, D-96-E, A-4-L, and B-16-J. Approximate model distances are indicated along a linear profile. THMB, Thunder Mountain broadband seismic station; RAMB, southwest Quesnel broadband seismic station.

Topographic relief across the plateau is relatively low, with receiver elevations ranging from 824 m to 1554 m, and averaging 1190 m above sea level. Most shot and receiver locations were determined using high-precision differential GPS measurements, which provided horizontal positional accuracy of less than 2 m and elevation accuracy of a few metres. Errors resulting from positional uncertainties of sources and receivers are considered negligible relative to other errors.

TABLE 2.1. Size of charge, charge depth and number of usable traces for the Nechako Basin segment of the BATHOLITHSonland seismic survey line.

Shotpoint	Charge size (kg)	Top of charge (m)	# of usable traces
1	800	18.3	980
3	780	15.2	980
10	580	18.9	991
15	800	15.2	988
17	500	15.2	985
20	700	15.2	980
22	940	15.2	980
27	880	15.2	980

2.2 Data Quality and Processing

The raw unprocessed data sampled at 4 ms were of good quality (Figs. 2.2*a*, 2.3). Background noise was greater over model distance 170-185 km, likely due to localized active logging, and near model distance 20 km, likely due to road traffic near a sawmill (Figs. 2.2*a*, 2.3). Most noise was easily removed after application of a zero-phase bandpass filter with limits 0.5 Hz to 15 Hz (Figs. 2.2*b*, 2.4). In total, 133 dead or noisy traces were removed from the 8 shot gathers, ranging from 9 to 22 traces per shot (Table 2.2). This represented less than 2% of the seismic dataset.

To avoid possible time shifts due to filter side lobes, picks were initially made with no processing applied. Observed phases included first-arrivals through the surface layer (Ps), upper crust (Pg), lower crust (Pc) and upper mantle (Pn), and secondary-arrivals reflecting from the base of crust (PmP). Table 2.3 quantifies the number of observations of each phase made in each shot gather. In regions of very weak first-arrivals (e.g., Figs. 2.4*a*, 2.4*c* - inset), increased gain levels were applied for improved identification of picks (Fig. 2.5). For arrivals at larger offsets (Pc and Pn) and for secondary-arrivals (PmP), pick identification improved using the bandpass filtered data in conjunction with average-amplitude trace balancing, which scales the traces to have equivalent average amplitudes. This resulted in improved phase coherency and clarity of first-arrivals for the noisier sections (Fig. 2.4). Automated picking of first-arrivals was possible to offsets of more than 50 km. At greater distances and for secondary-arrivals, manual picking was necessary. The estimated picking error was 65 ms for first-arrivals and 100 ms for secondary-arrivals. Figure 2.5 demonstrates the variable-gain approach

used for phase picking, as well as for clear concurrent display of both primary and secondary arrivals within the shot gathers of figures 2.6*a*-2.13*a*.

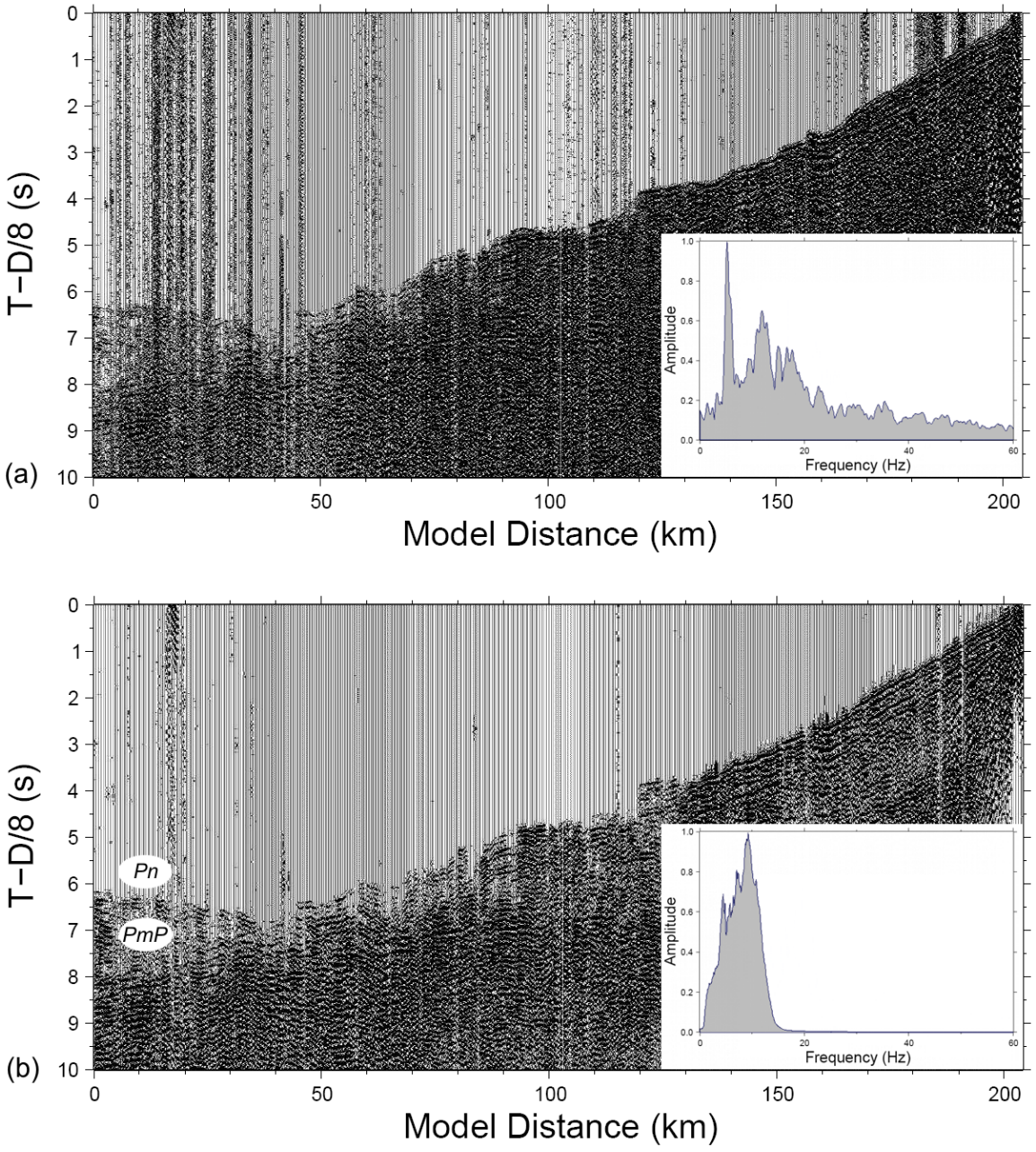

Figure 2.2. Sample trace-equalized data from shotpoint 1 before *(a)* and after *(b)* the application of a 0.5-15 Hz bandpass filter. High frequencies have been removed as indicated by the inset amplitude plots, resulting in greatly reduced noise along the western ~50 km and eastern ~25 km of the survey line. Improved clarity of first-arrival refracted (Pn) and secondary-arrival reflected (PmP) energy from the Moho is evident in *(b)*. Plotted with a reducing velocity of 8.0 km/s.

TABLE 2.2 Number of traces removed from each shot gather, due to high noise levels or dead traces. The corresponding percentage of traces removed for a particular shot gather is also given.

Shotpoint	Number of traces removed (% of total)
1	22 (2.2%)
3	20 (2.0%)
10	9 (0.9%)
15	14 (1.4%)
17	15 (1.5%)
20	14 (1.4%)
22	18 (1.8%)
27	21 (2.1%)

TABLE 2.3. Number of observations of each phase made for each shot gather, and total number of picks made for each shot. Pick uncertainty is given beneath each phase.

Shotpoint	Observed phases	Ps (65ms)	Pg (65ms)	Pc (65ms)	PmP (100ms)	Pn (65ms)	Total
1	Ps, Pg, Pc, PmP, Pn	18	441	178	173	118	928
3	Ps, Pg, Pc, PmP	23	713	156	247		1139
10	Ps, Pg, Pc, PmP	71	667	147	263		1148
15	Ps, Pg, PmP	58	888		314		1260
17	Ps, Pg, PmP	99	866		310		1275
20	Ps, Pg, PmP	47	899		223		1169
22	Ps, Pg, Pc, PmP, Pn	51	631	220	349	103	1354
27	Ps, Pg, Pc, PmP, Pn	5	601	382	460	63	1511

2.3 Data Analysis

Ps apparent velocity varies from 3.3 km/s to 4.8 km/s. The fastest apparent velocities are observed near shotpoints 1 (Figs. 2.3*a*, 2.6*a*) and 27 (Fig. 2.13*a*) at either end of the seismic line, while shotpoints 17 (Fig. 2.10*a*) and 3 (Fig. 2.7*a*) in the central region produce the slowest apparent velocities for near-offset rays turning within the surface layer. Ps amplitudes are very large due to short offsets and strong vertical velocity gradients near the surface.

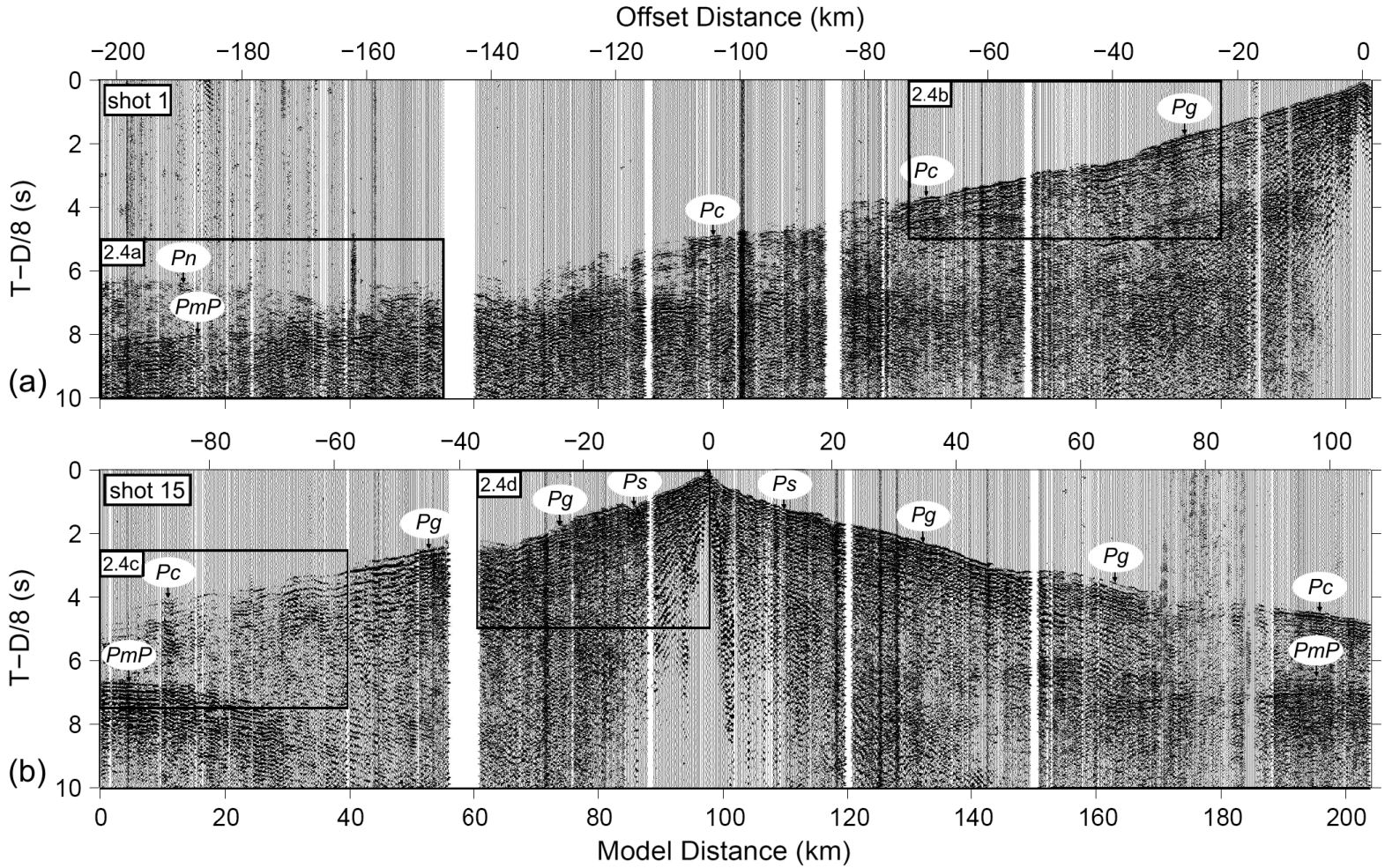

Figure 2.3. Refraction – wide-angle reflection data for *(a)* shotpoint 1 and *(b)* shotpoint 15. Interpreted first and secondary-arrival phases are identified. Ps, refraction through the surface layer; Pg, refraction through the upper crust; Pc, refraction through the middle crust; Pn, refraction from the upper mantle; PmP, reflection from the Moho. Shot gathers are plotted with a reducing velocity of 8.0 km/s, with average-amplitude trace balancing applied. Boxes indicate enlargements shown in Fig. 2.4.

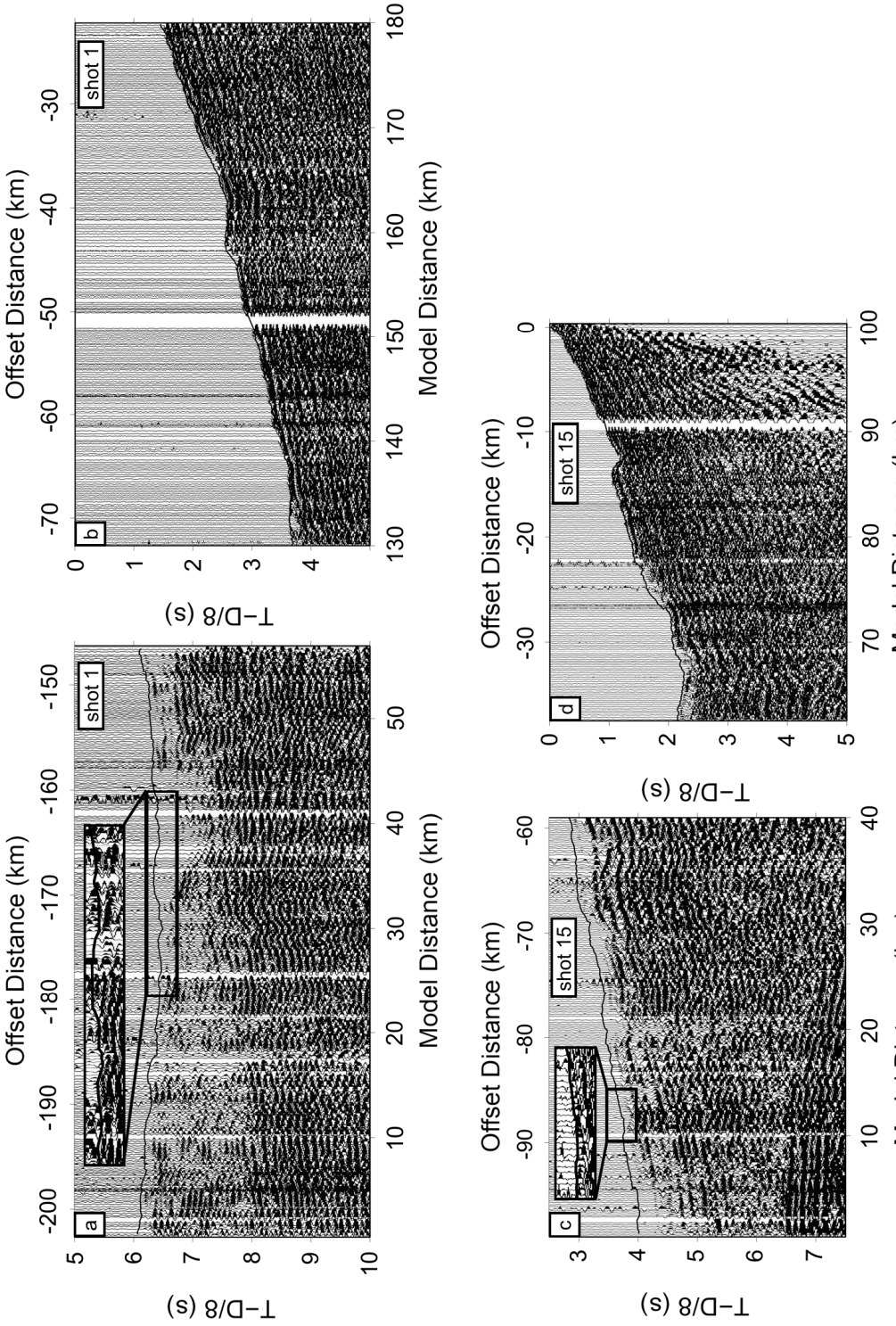

Figure 2.4. First-arrival picks (thin black line) for shotpoint 1 (a, b) and shotpoint 15 (c, d). Inset boxes show low-amplitude first arrivals. Data are plotted with a reducing velocity of 8.0 km/s, filtered (0.5-15 Hz), and scaled with average-amplitude trace balancing.

The Ps-Pg crossover distance ranges from 3 km to 15 km, becoming less distinct toward the east. This indicates a sharper velocity contrast at the base of the surface layer in the west, with a smoother velocity gradient towards the east. The crossover distance is generally greater in the east, indicating larger thickness of lower-velocity material. A notable exception is shotpoint 1 (Fig. 2.6*a*), where Pg phases are observed at short offsets (Fig. 2.3*a*).

Apparent velocities of Pg turning rays range from 5.7 km/s to 6.3 km/s. Deeper Pc refractions exhibit slightly higher apparent velocities, varying from 6.1 km/s to 6.5 km/s. The small Pg-Pc velocity contrast (ie. Fig. 2.3*b*), in comparison to the larger Ps-Pg disparity, is representative of significantly reduced velocity gradient with depth in the crust below the surface layer.

PmP arrivals, or waves reflected off the Moho, are identified on all 8 shot records. Reflected energy from the base of the crust is recorded at near-offset distances ranging from 37 km to 73 km with an average of 60 km. The large PmP amplitudes (ie. Fig. 2.3) are representative of the strong positive velocity discontinuity between the base of the crust and the upper mantle.

Pn arrivals, or refractions through the uppermost mantle, are observed as first-arrivals at a minimum distance of ~170 km. Pn is observed only for shots 1 (Figs. 2.3*a,* 2.6*a*), 22 (Fig. 2.12*a*), and 27 (Fig. 2.13*a*). Pn refractions from all eight shots were recorded by receivers within the Coast Belt, and the six shotpoints in the Coast Belt (Fig. 1.2) produced refractions on receivers in the Intermontane Belt. However, these data are not included in this initial analysis, as they are dependent on velocity structure from outside the model boundaries. Mantle turning rays are relatively weak in amplitude (Figs. 2.3*a*, 2.4*a*), but they are still assigned an uncertainty of 65 ms due to their readily

identifiable first-arrival nature. Refracted energy from the upper mantle exhibits apparent velocities of 8.2-8.4 km/s.

Figure 2.5. Sample combination of high and low-amplitude shot gathers for purpose of output display in figures 2.6*a*-2.13*a*. Because first-arrival amplitudes varied so much across the survey line, beyond the capability of offset-based trace balancing, it was necessary to amalgamate high and low amplitude shot gathers for coincident display of primary and secondary arrivals. The low amplitude plot in *(a)* is useful for identification of short-offset (Ps, Pg) and long-offset (Pn) first arrivals, and strong secondary arrivals (PmP). The low amplitude plot is poor for identification of medium-offset first arrivals (Pg, Pc), which have low trace-balanced amplitudes because of the large PmP amplitudes at later arrival times. The higher amplitude plot in *(b)* clarifies these mid-to-deep-crustal turning ray arrivals. The final combined display in *(c)* contains the above plots overlain at 50% opacity, clearly displaying all primary and secondary arrivals. Plotted with a reducing velocity of 8.0 km/s.

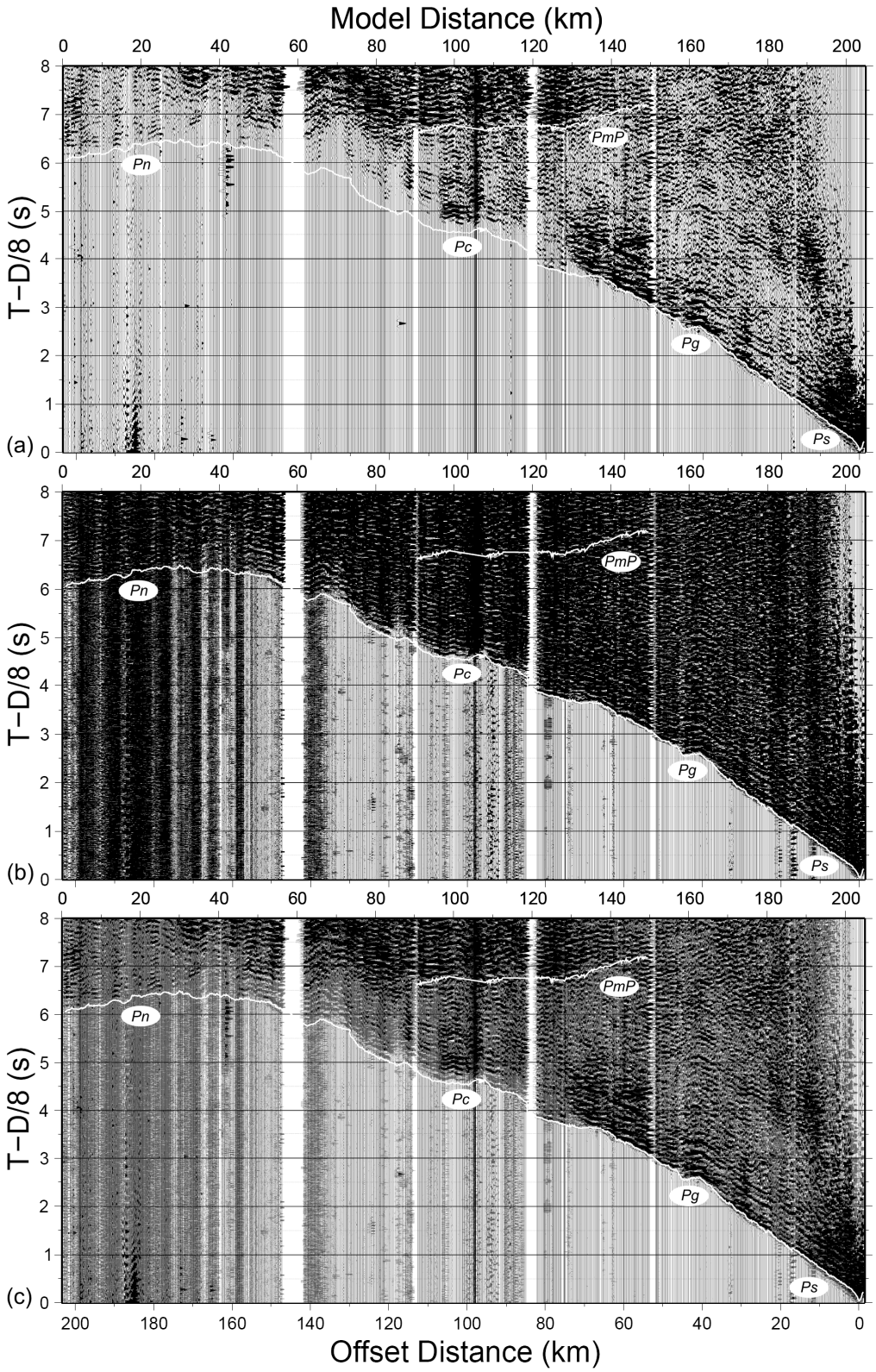
Model Distance (km)
T−D/8 (s)
Pn
Pc
PmP
Pg
Ps
(a)
(b)
(c)
Offset Distance (km)

Figures 2.6-2.13. *(a)* Seismic traveltime data with labelled phases. Observed arrival picks are indicated by overlain white lines. For some shot gathers, the high gain plot contributes very large amplitudes at small offsets, which misleadingly appear to be pre-first-arrival energy. *(b)* Comparison of traveltime picks (vertical bars) and calculated traveltimes (solid lines). Ps, Pg, Pc and Pn primary arrivals are those produced by the gridded first-arrival algorithm, while PmP secondary arrivals are from the layered block-model. The heights of the vertical bars are equal to twice the pick uncertainty. Plotted with a reducing velocity of 8.0 km/s.

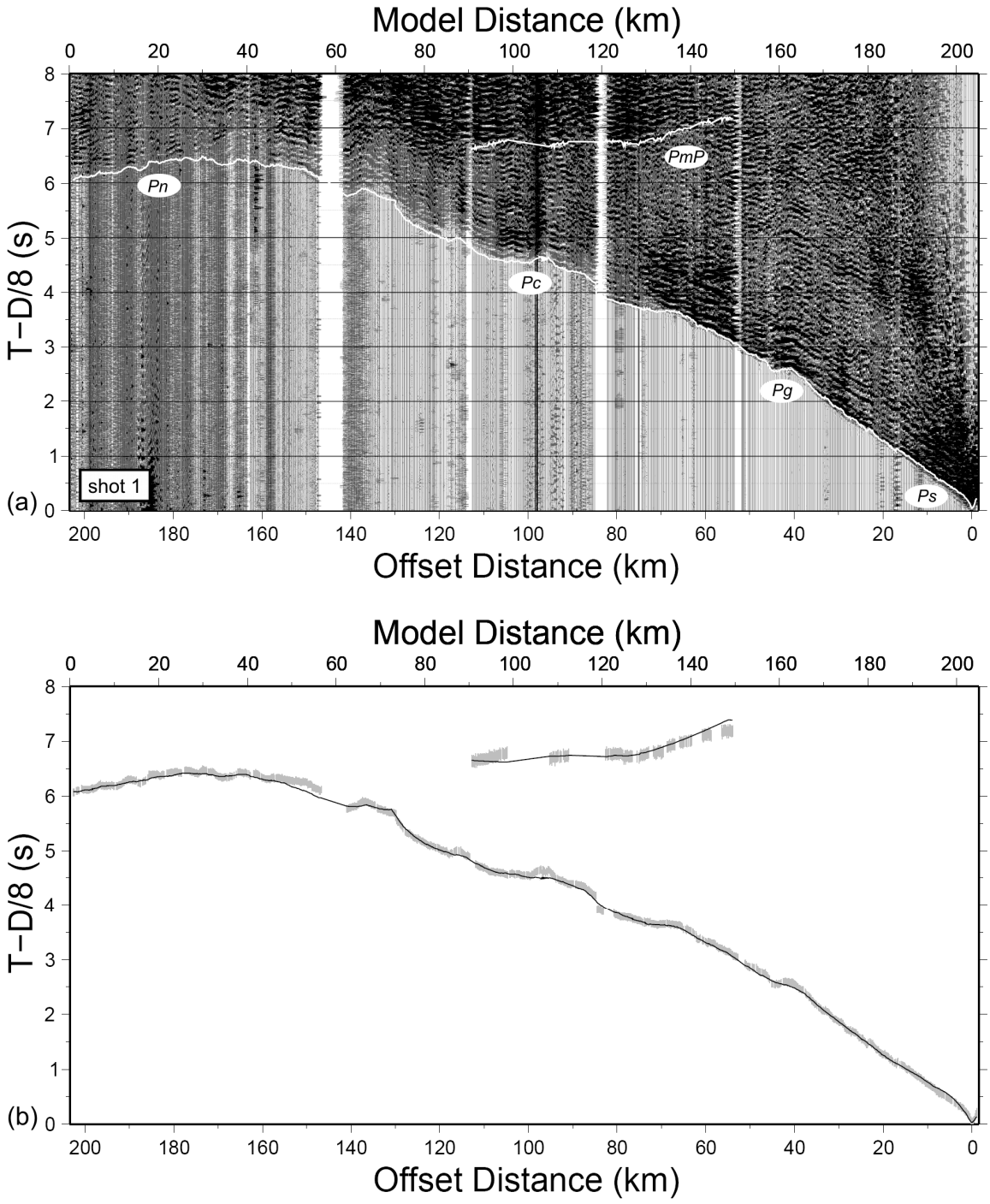
Model Distance (km)
0 20 40 60 80 100 120 140 160 180 200
T−D/8 (s)
8 7 6 5 4 3 2 1 0
Pn
PmP
Pc
Pg
Ps
shot 1
(a)
200 180 160 140 120 100 80 60 40 20 0
Offset Distance (km)
Model Distance (km)
0 20 40 60 80 100 120 140 160 180 200
T−D/8 (s)
8 7 6 5 4 3 2 1 0
(b)
200 180 160 140 120 100 80 60 40 20 0
Offset Distance (km)

Figure 2.6.

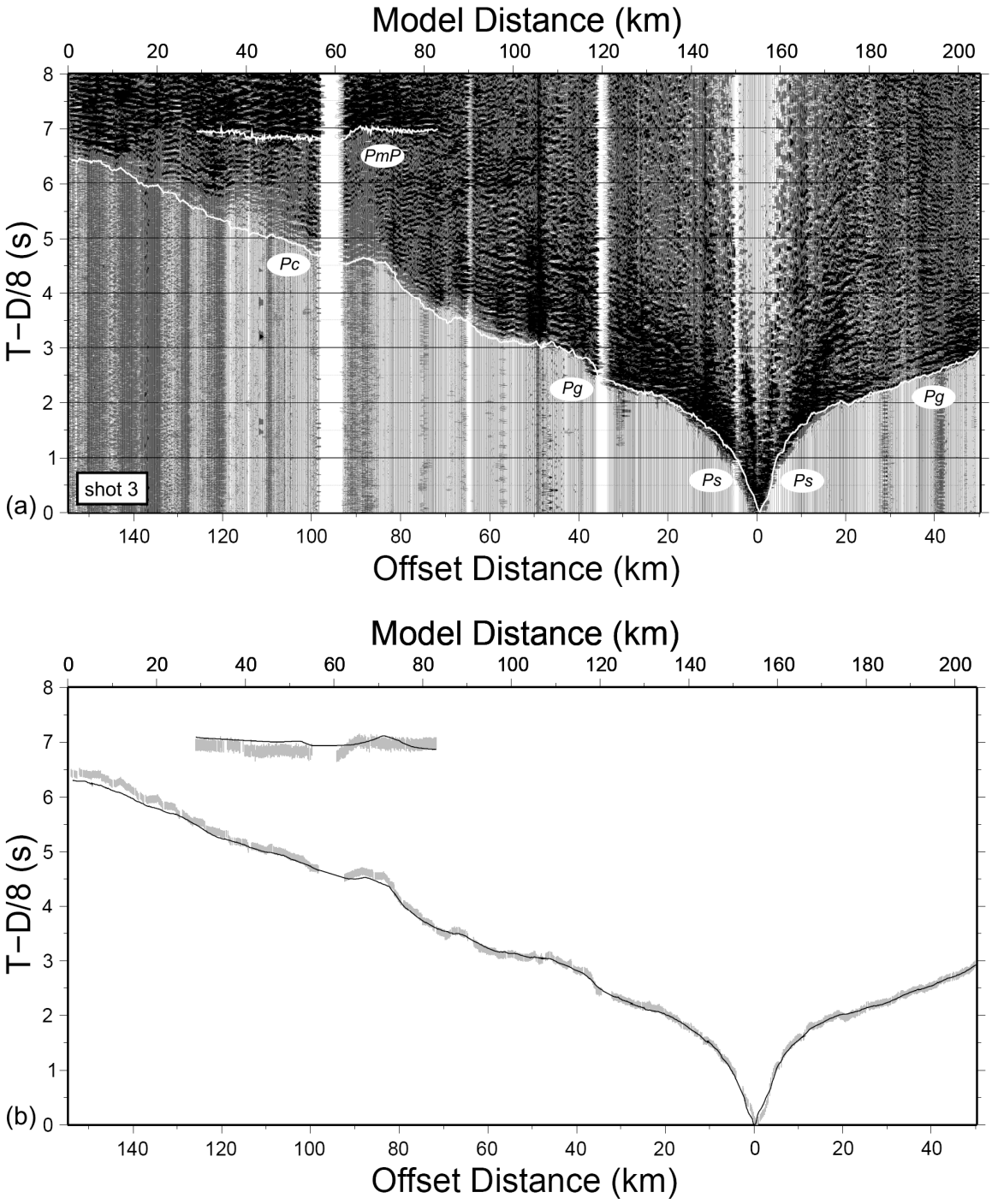
Model Distance (km)
0 20 40 60 80 100 120 140 160 180 200
T−D/8 (s)
8 7 6 5 4 3 2 1 0
PmP
Pc
Pg
Pg
Ps
Ps
shot 3
(a)
140 120 100 80 60 40 20 0 20 40
Offset Distance (km)
Model Distance (km)
0 20 40 60 80 100 120 140 160 180 200
T−D/8 (s)
8 7 6 5 4 3 2 1 0
(b)
140 120 100 80 60 40 20 0 20 40
Offset Distance (km)

Figure 2.7.

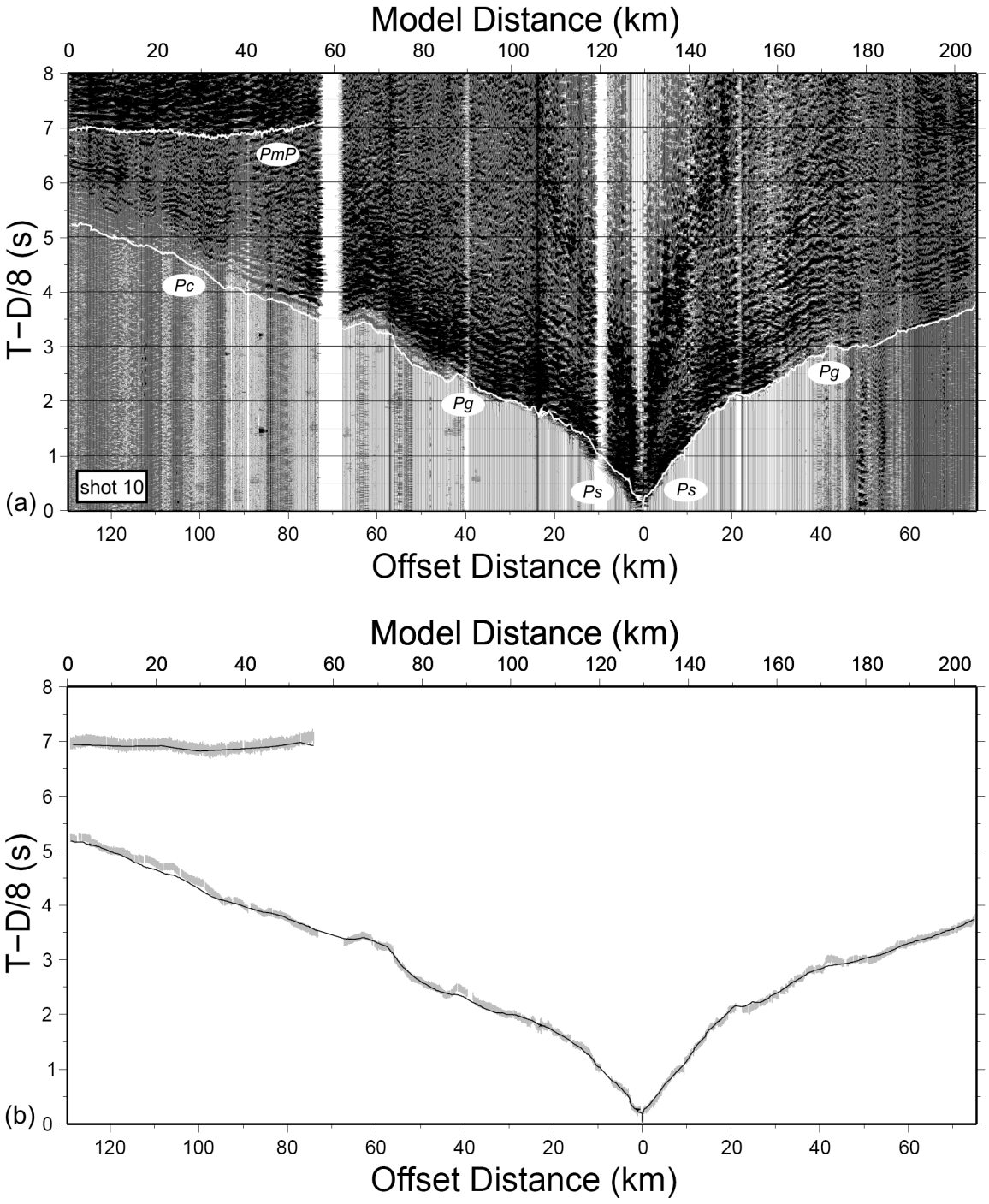
Model Distance (km)
0 20 40 60 80 100 120 140 160 180 200
T−D/8 (s)
PmP
Pc
Pg
Pg
Ps
Ps
shot 10
(a)
120 100 80 60 40 20 0 20 40 60
Offset Distance (km)
Model Distance (km)
0 20 40 60 80 100 120 140 160 180 200
T−D/8 (s)
(b)
120 100 80 60 40 20 0 20 40 60
Offset Distance (km)

Figure 2.8.

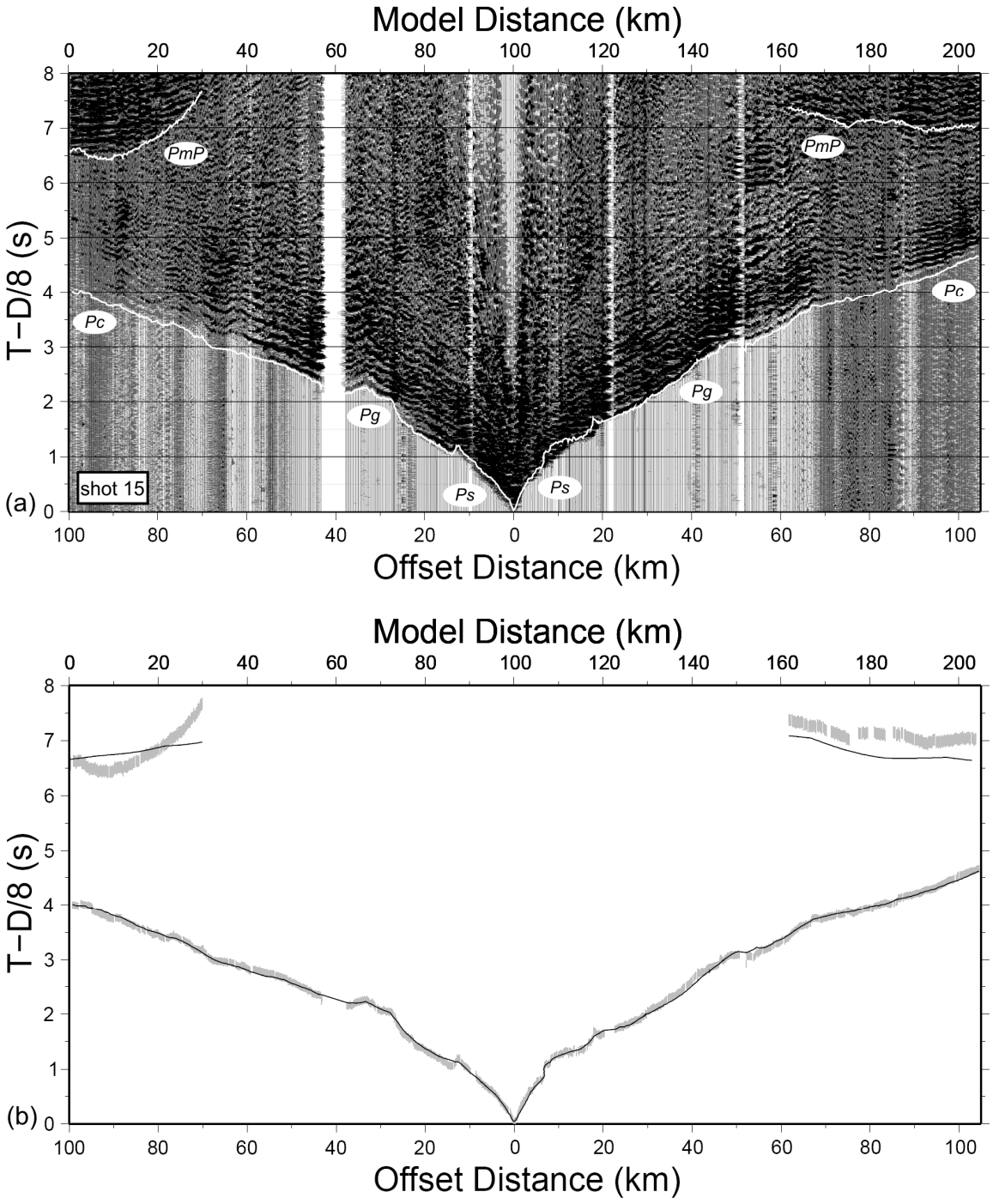
Model Distance (km)
0
20
40
60
80
100
120
140
160
180
200
T−D/8 (s)
PmP
PmP
Pc
Pc
Pg
Pg
Ps
Ps
shot 15
(a)
Offset Distance (km)
Model Distance (km)
T−D/8 (s)
(b)
Offset Distance (km)

Figure 2.9.

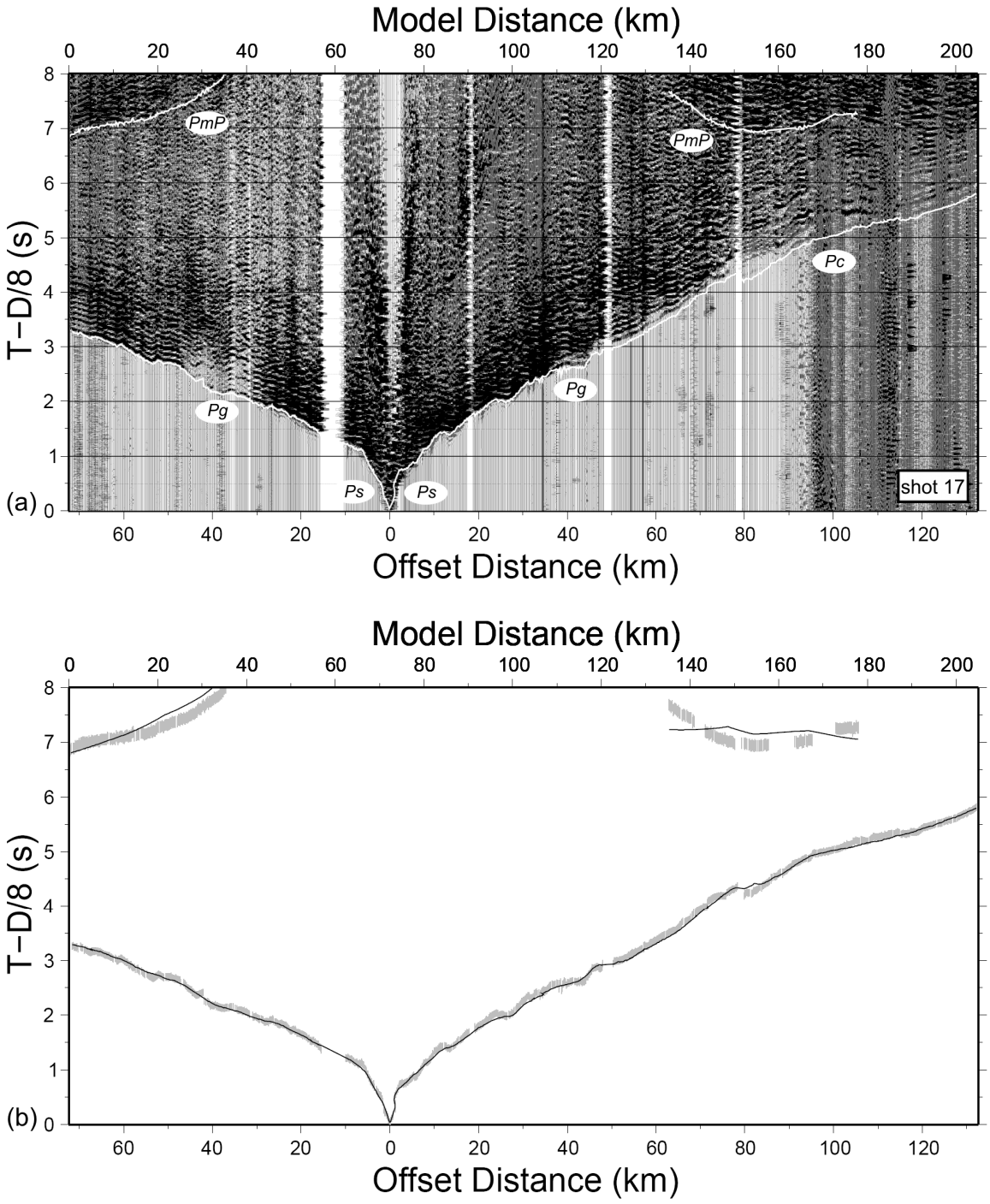
Model Distance (km)
0 20 40 60 80 100 120 140 160 180 200
T−D/8 (s)
0 1 2 3 4 5 6 7 8
PmP
PmP
Pc
Pg
Pg
Ps
Ps
shot 17
(a)
60 40 20 0 20 40 60 80 100 120
Offset Distance (km)
Model Distance (km)
0 20 40 60 80 100 120 140 160 180 200
T−D/8 (s)
0 1 2 3 4 5 6 7 8
(b)
60 40 20 0 20 40 60 80 100 120
Offset Distance (km)

Figure 2.10.

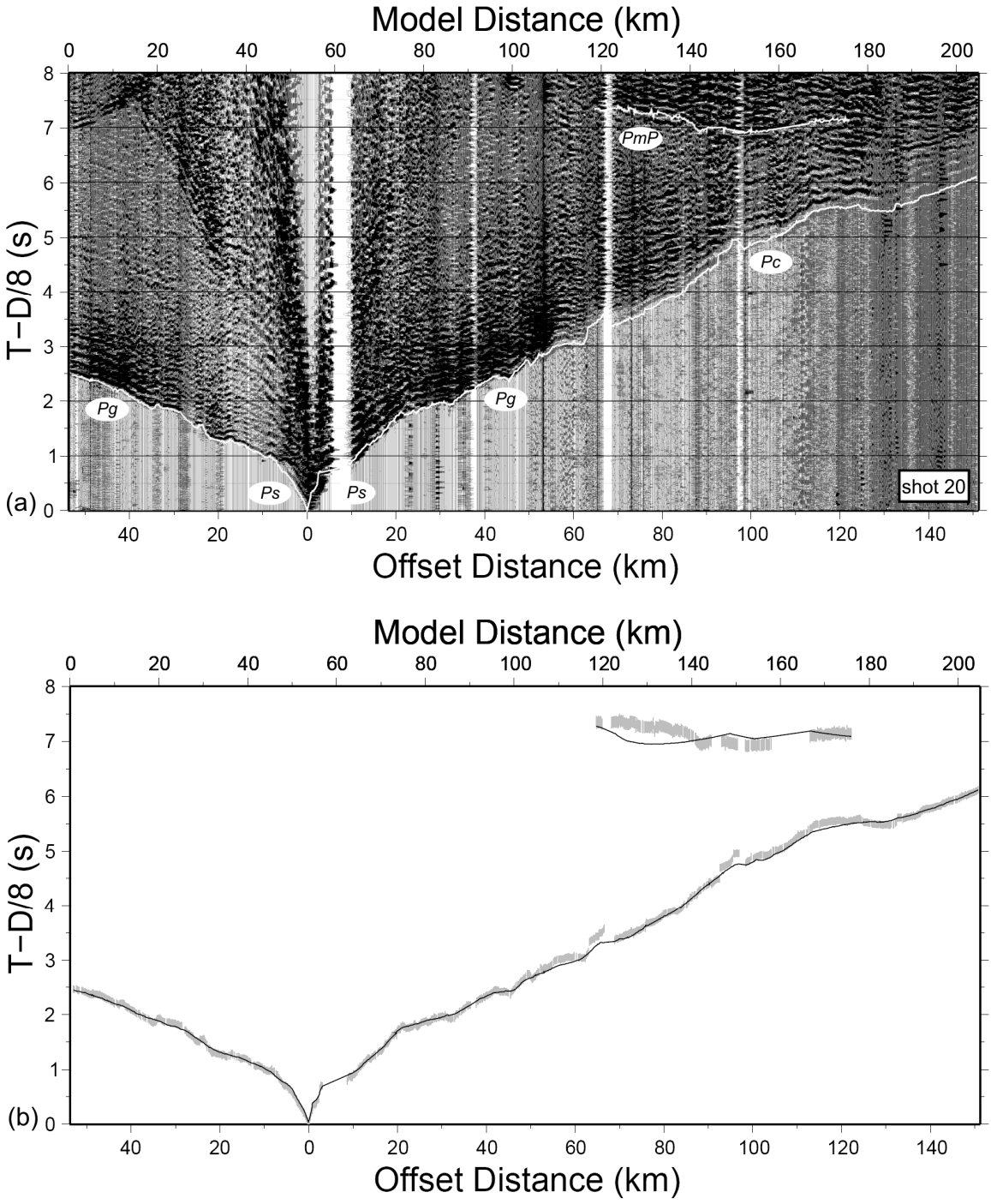
Model Distance (km)
0 20 40 60 80 100 120 140 160 180 200
T–D/8 (s)
0 1 2 3 4 5 6 7 8
PmP
Pc
Pg
Pg
Ps
Ps
shot 20
(a)
40 20 0 20 40 60 80 100 120 140
Offset Distance (km)
Model Distance (km)
0 20 40 60 80 100 120 140 160 180 200
T–D/8 (s)
0 1 2 3 4 5 6 7 8
(b)
40 20 0 20 40 60 80 100 120 140
Offset Distance (km)

Figure 2.11.

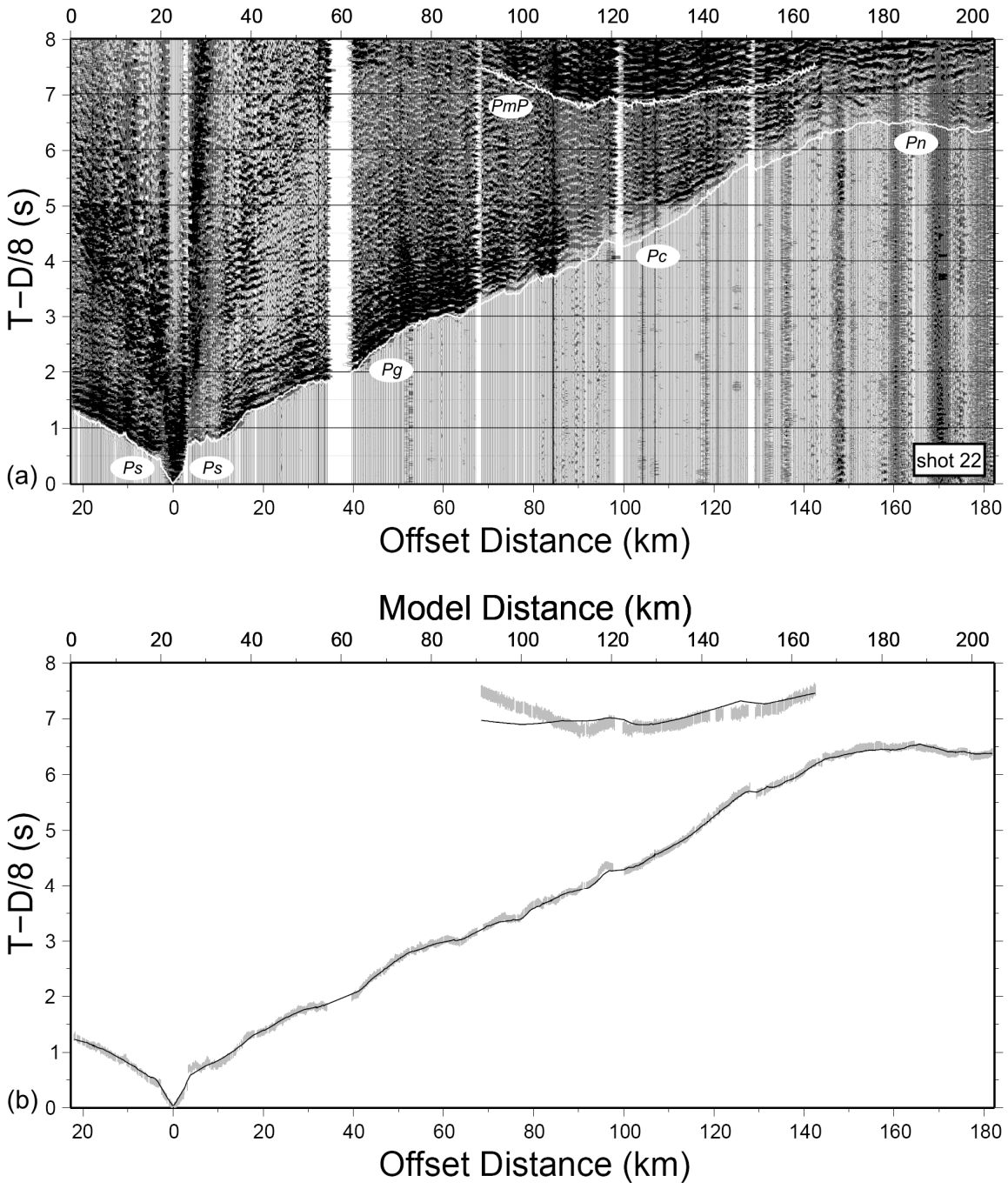
T−D/8 (s)
Offset Distance (km)
PmP
Pn
Pc
Pg
Ps
Ps
shot 22
(a)
Model Distance (km)
T−D/8 (s)
Offset Distance (km)
(b)

Figure 2.12.

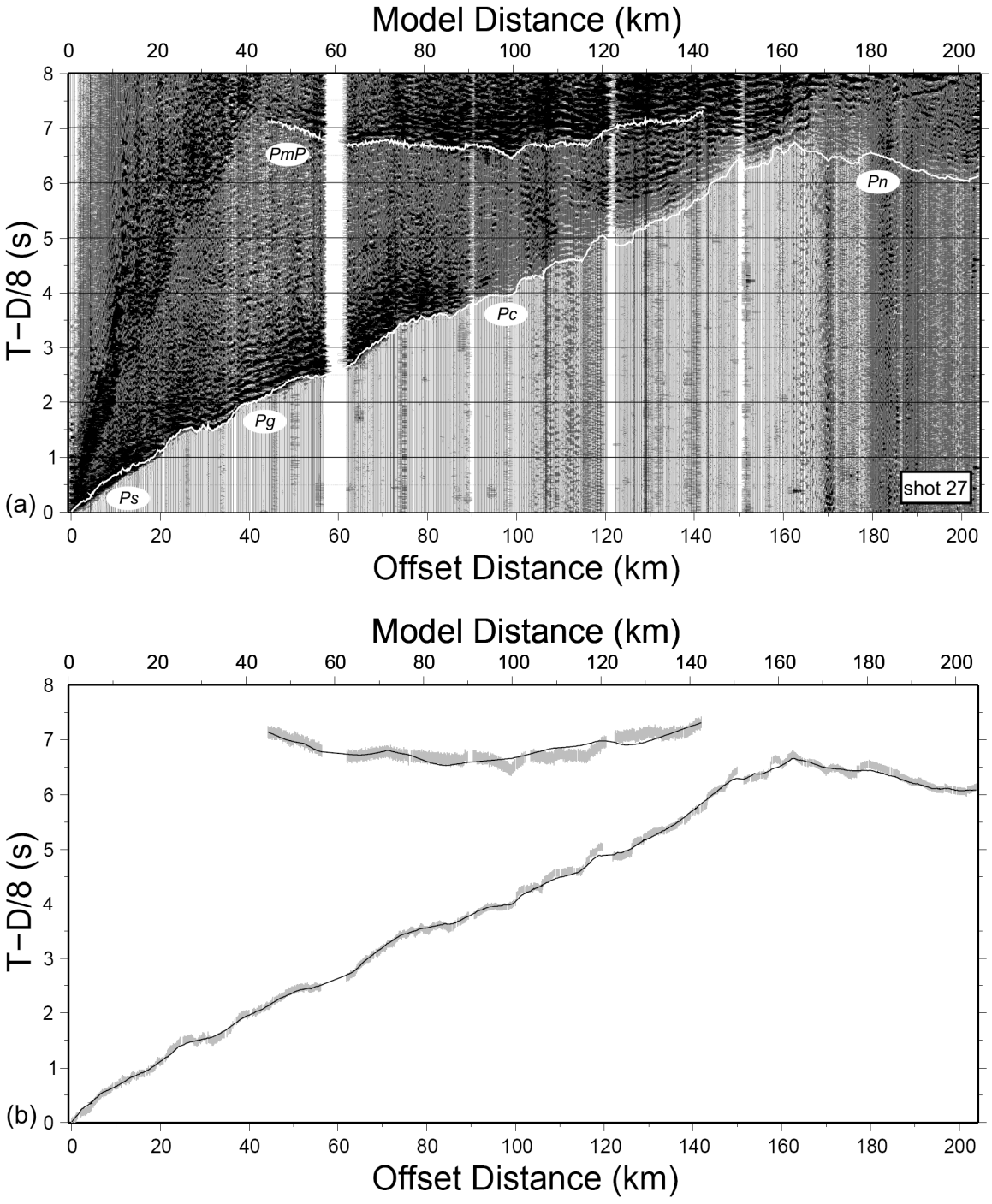
Model Distance (km)
0
20
40
60
80
100
120
140
160
180
200
T−D/8 (s)
0
1
2
3
4
5
6
7
8
PmP
Pn
Pc
Pg
Ps
(a)
shot 27
Offset Distance (km)
Model Distance (km)
T−D/8 (s)
(b)
Offset Distance (km)

Figure 2.13.

Chapter 3 Modelling of Refraction/Reflection Data

3.1 Traveltime inversion of first and secondary-arrivals using a block model

Two distinct seismic traveltime inversion algorithms were utilized to build lithospheric velocity models describing the acquired refraction data. Traveltimes were modelled using the RAYINVR ray-tracing algorithm of Zelt and Smith (1992), which allows for iterative forward modelling and inversion of layer depths and velocities. This inversion algorithm models first-arrivals and secondary phases, either refractions or reflections, using a block model. The block model is defined by depth and velocity boundary nodes, with velocities linearly interpolated between specified control points. Explicit identification of ray phases is required for association of an arrival with a specific block or interface in the model; this requires experience and hence subjective input. Since the algorithm is inherently 2D, shots along the crooked line must be projected onto a single 2D profile, while maintaining the correct shot-receiver offset (Fig. 3.1). A model distance of 0 km corresponds to the projected position of the westernmost shotpoint 27 (Fig. 2.1).

The starting model was a 1D velocity profile based on *a-priori* data. Synthetic traveltimes that fit the general slopes of the Ps and early Pg arrivals were generated via extensive trial-and-error forward modelling facilitated by the ray-tracing inversion program. Next, inversion was undertaken to allow for fine-tuning of the fit between observed and modelled traveltimes. Forward and inverse modelling were performed via a layer-stripping approach, with the objective of fitting the shallowest arrivals first, on the

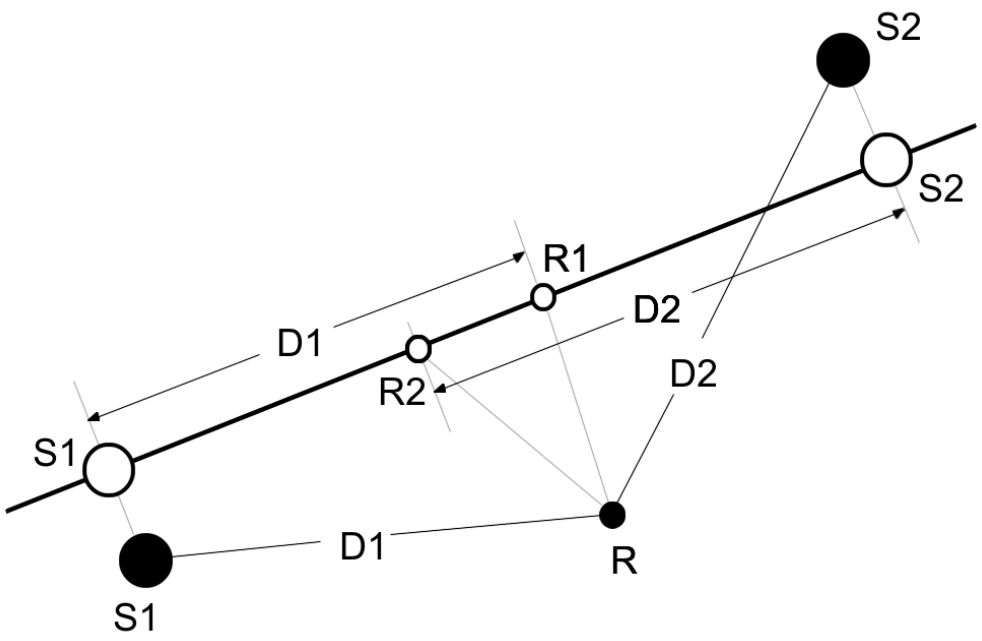

Figure 3.1. Method for projecting crooked-line geometry onto a straight line, required for the 2D layered block model (redrawn from Zelt, 1999). Shots S1 and S2 project perpendicularly onto the straight line. Receiver R projects onto two separate locations on the straight line (R1 and R2), maintaining the correct shot-receiver offsets (D1 and D2) relative to each projected shotpoint.

basis that all later arrivals are influenced by the near-surface velocity structure. The procedure consisted of manual velocity perturbation and forward modelling, inversion for velocity and depth nodes of a single layer while holding all other layer parameters fixed, and then tracing of rays through the improved model. This method proved effective in gradually reducing the misfit between observed and synthetic traveltimes, first satisfying the general traveltime slopes at small offsets, and then allowing increasingly localized lateral velocity structure to develop to progressively larger offsets. Once the iterative modelling technique had been completed for each of the five layers and traveltimes fit individually, a complete inversion for all model parameters was conducted, and rays were traced through the output velocity structure. Raypaths calculated by the layered block model inversion algorithm are shown in gray in figures 3.2-3.9.

Figures 3.2-3.9. Ray coverage by shotpoint. Primary and secondary arrival ray-traces used for the layered block model are shown in gray, while primary arrival raypaths traced by the first-arrival grid-based model are plotted in black. Model boundaries of the layered block model are indicated by thin horizontal lines.

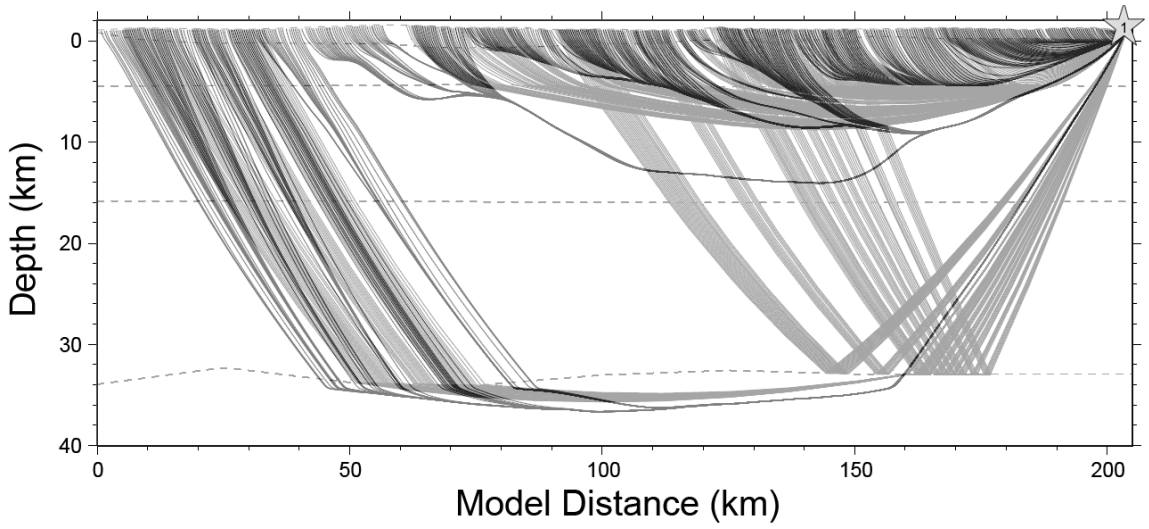

Figure 3.2.

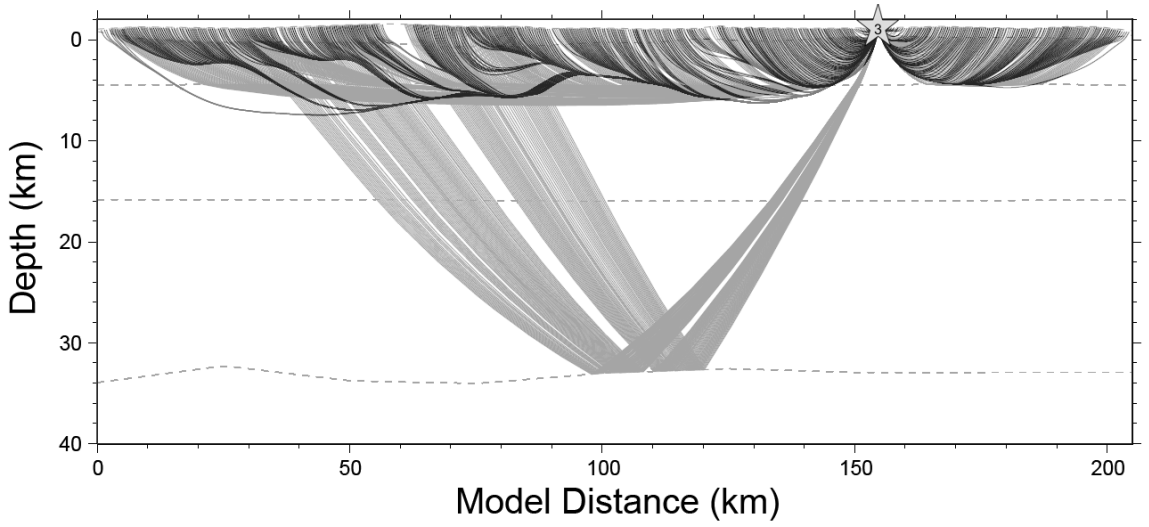

Figure 3.3.

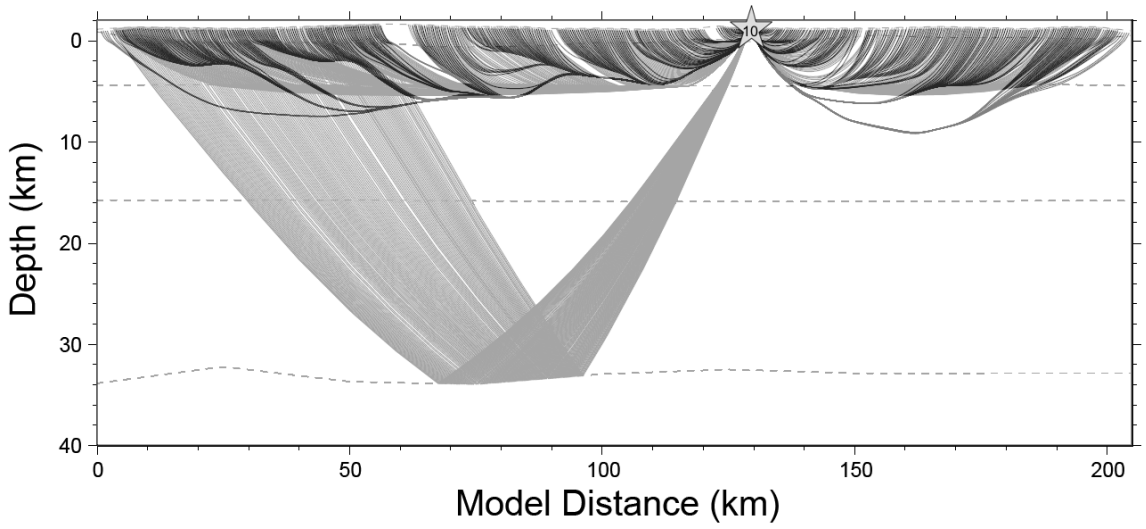

Figure 3.4.

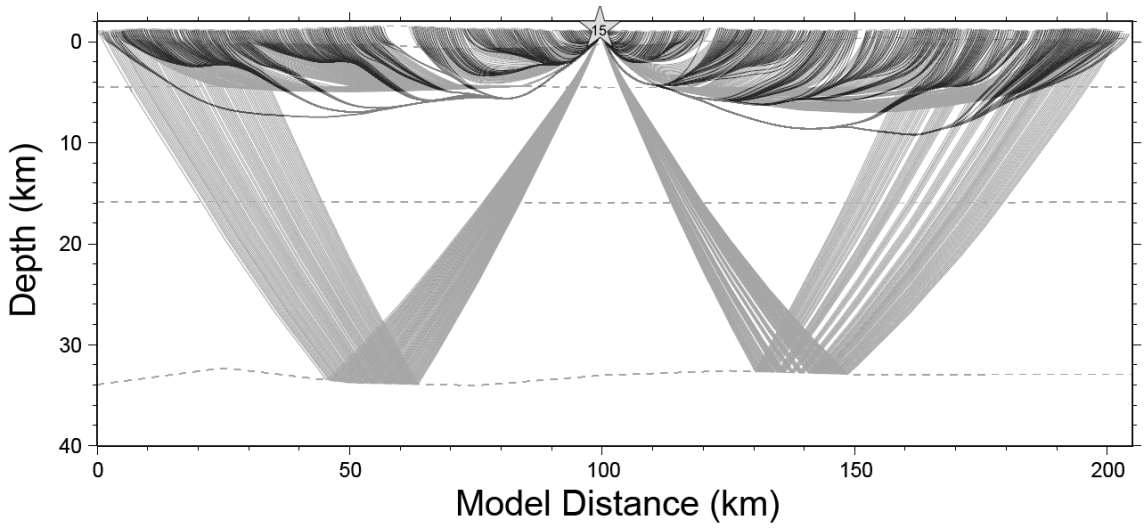

Figure 3.5.

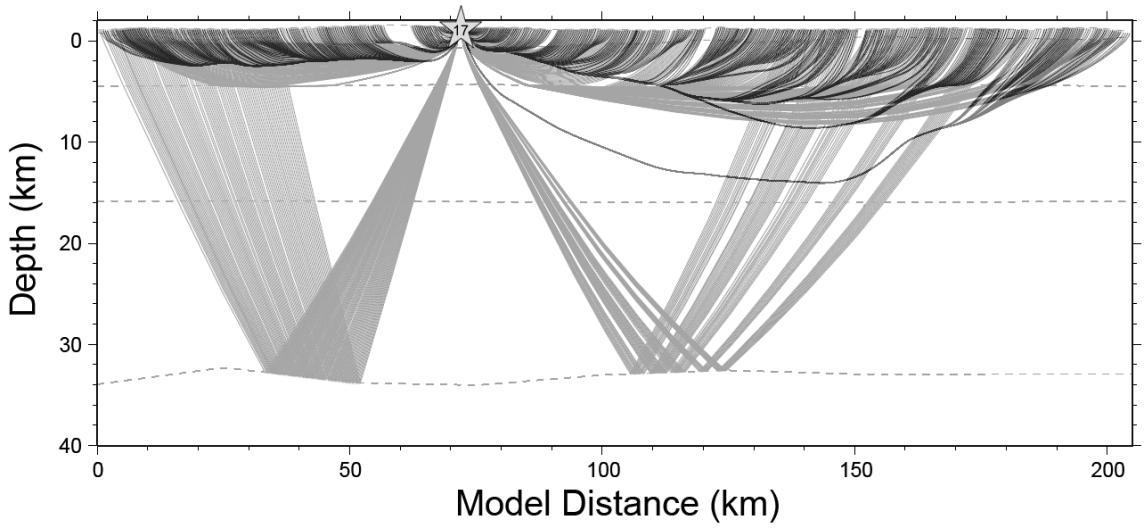

Figure 3.6.

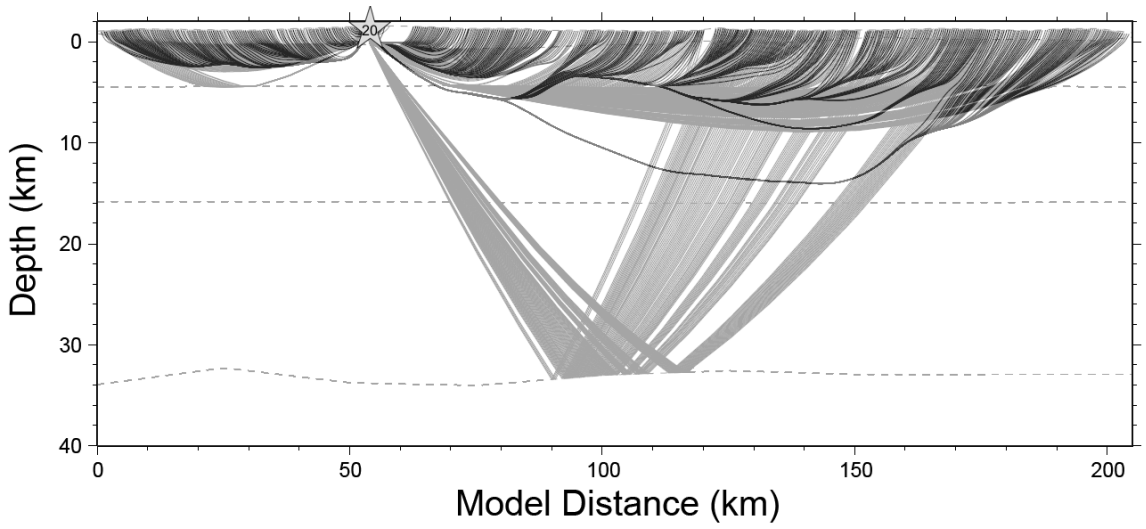

Figure 3.7.

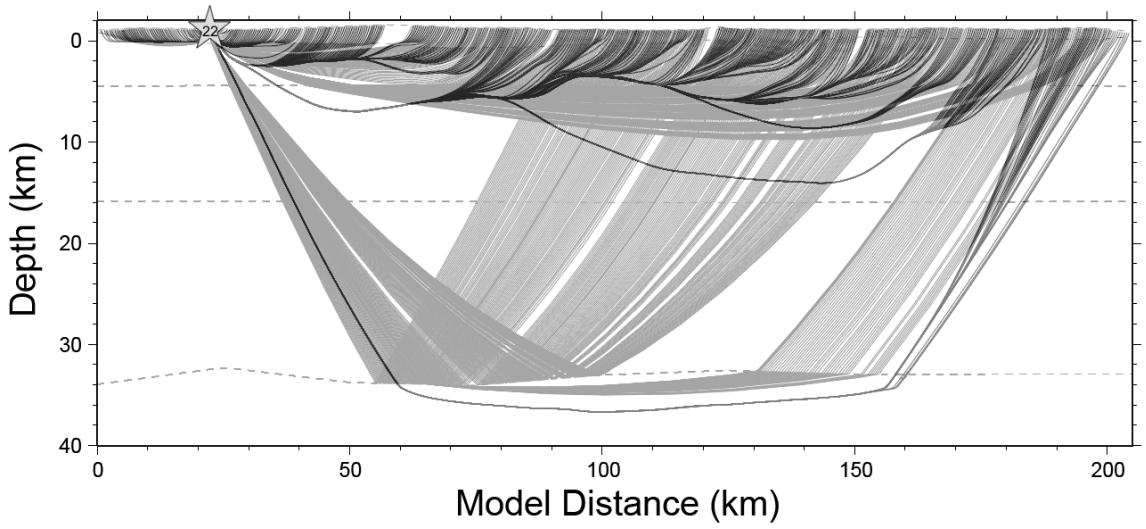

Figure 3.8.

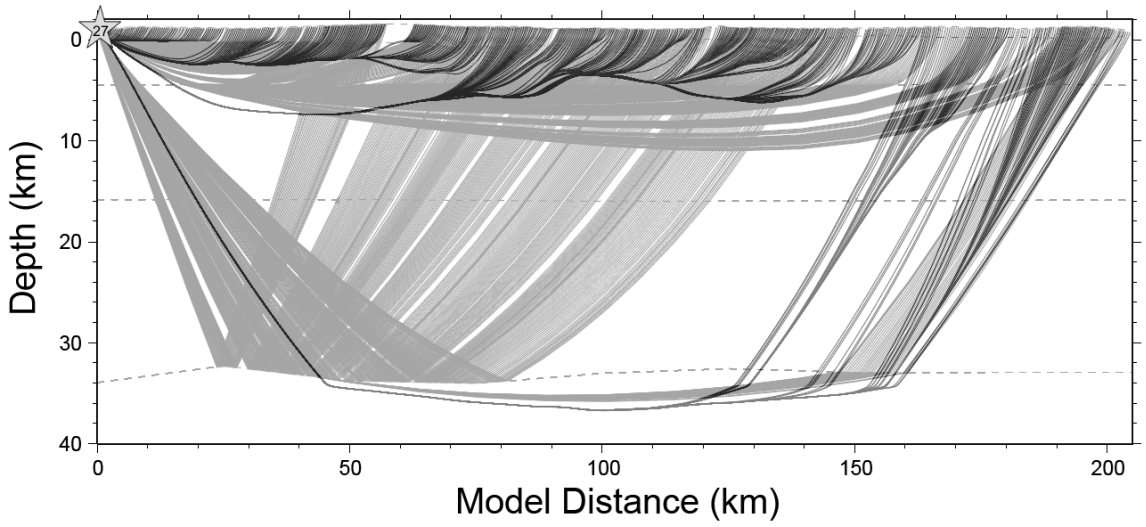

Figure 3.9.

The final model consisted of 92 inter-nodal blocks (Fig. 3.10). An increased level of model parameterization at shallow depths was required to model accurately the near-offset first-arrivals, which provide a very high density of ray coverage (Fig. 3.11*a*). The first and second layers consisted of 27 and 41 blocks, respectively, with the remaining three deeper layers comprising eight blocks each (Fig. 3.10).

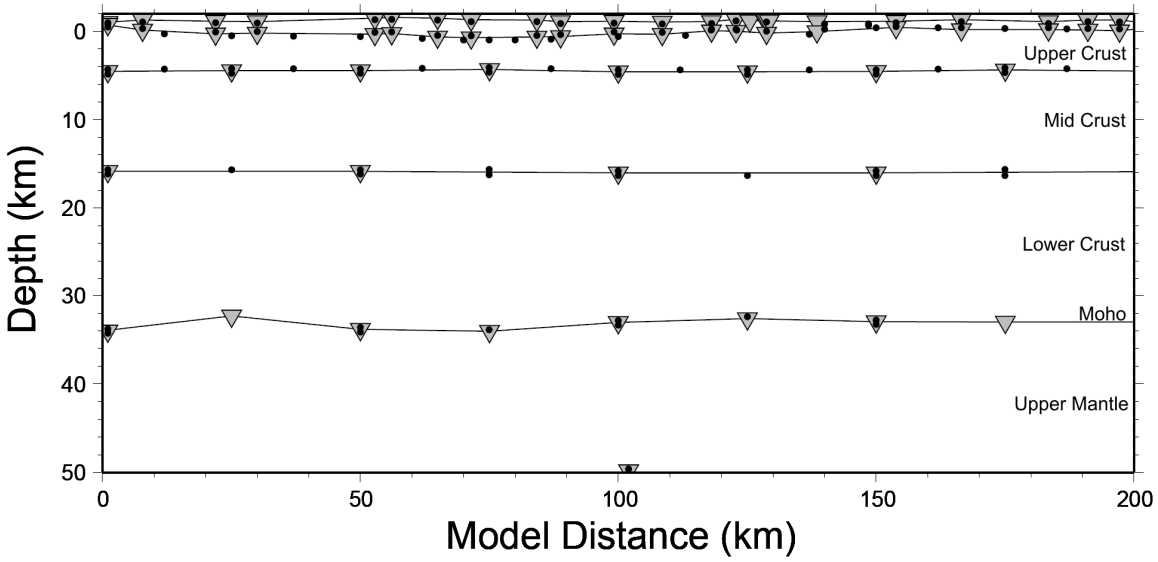

Figure 3.10. Final velocity model parameterization of the layered block-model ray tracing algorithm (modified from Zelt and Smith, 1992). Inverted triangles indicate depth nodes and filled circles indicate velocity nodes. 192 boundary nodes parameterize the final model: 71 depth nodes and 121 velocity nodes. Crustal sections are labelled to the right.

The output velocity model (Fig. 3.11*c*) produced synthetic traveltimes that fit the observed data reasonably well (Fig. 3.11*b*; Table 3.1). For 9418 rays representing all five phases, an RMS traveltime residual of 120 ms gave a χ^2 equal to 2.32. More significantly for shallow structure, 5741 Ps and Pg phases fit the observed data with a traveltime residual of 82 ms, and χ^2 of 1.60. A value of χ^2 larger than 1 means that the traveltime residual is larger than the estimated picking error (65 ms). With receiver stations closely

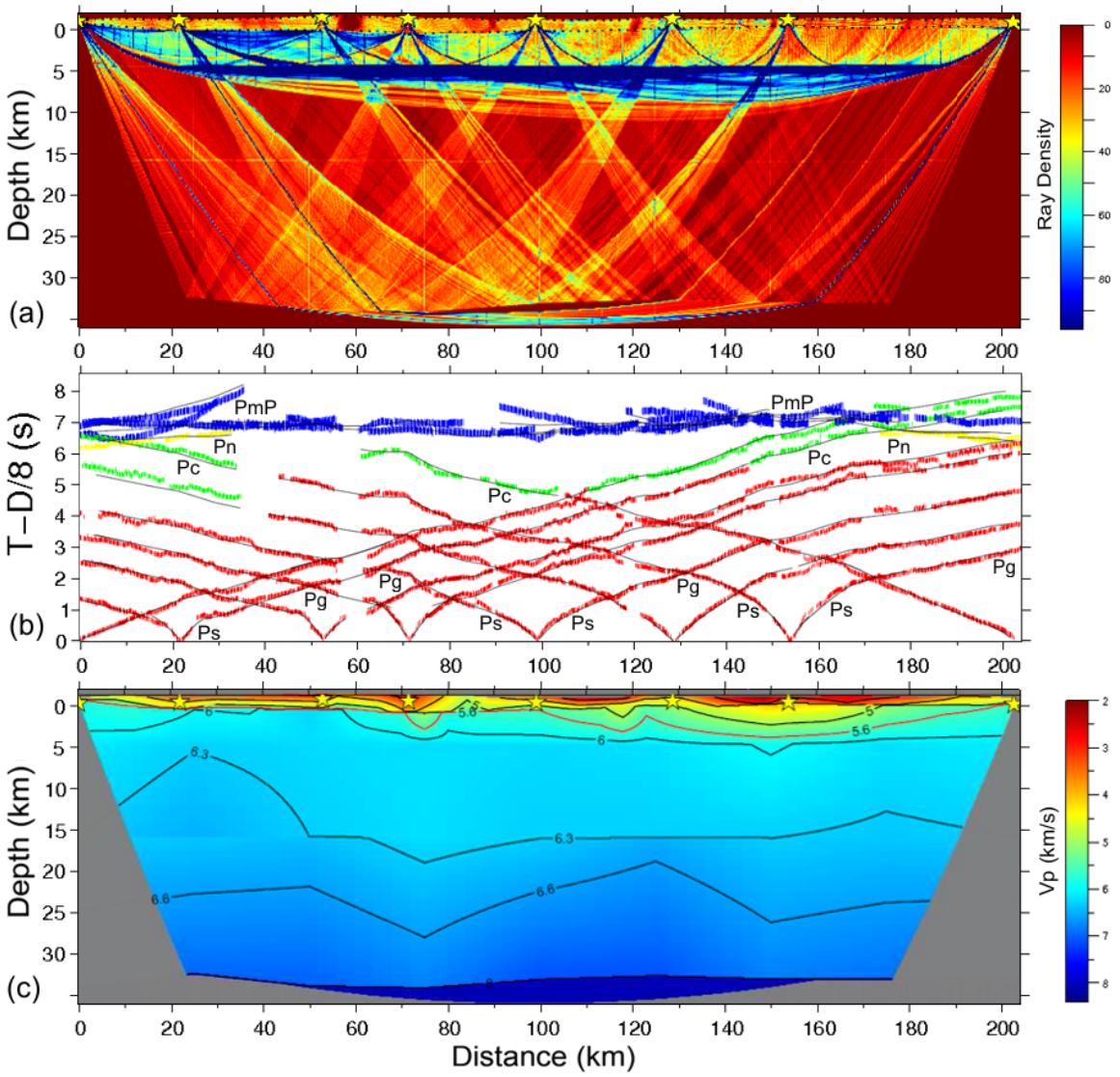

Figure 3.11. *(a)* Ray density provided by block model inversion algorithm, including secondary arrivals (PmP). Layer boundaries are found at ~1 km, ~6 km, ~16 km, and ~35 km depth. *(b)* Synthetic traveltimes produced by layered block model are given by thin black lines. Observed traveltime picks are indicated by coloured dashes of widths equal to twice the estimated pick uncertainty. Plotted with a reducing velocity of 8.0 km/s. Red, refraction through the upper crust (Ps, Pg); Green, refraction through the middle crust (Pc); Yellow, refraction through the upper mantle (Pn); Blue, reflection from the Moho (PmP). *(c)* Layered velocity (Vp) model from first and secondary-arrivals.

spaced at 200 m separation, fine-scale lateral variations in traveltime could be identified. These deviations, produced by lateral variations in shallow velocity structure, could not be modelled precisely and hence produced the larger χ^2 value. Even though we attempted to model the shallow structure with a large number of velocity and boundary nodes, the block model approach of Zelt and Smith (1992) is not ideally suited for such high-resolution modelling of the shallow subsurface. However, the routine has the advantage that it can model wide-angle Moho reflections and thus provide constraints on lower-crustal structure.

TABLE 3.1. Results of traveltime inversion of layered block-model. Number of nodes and modelled fit to the data are given for each layer, with the ray phases traced through each layer given in brackets.

	RMS tt. residual (s)	Normalized χ2 misfit	# of velocity nodes	# of depth nodes
Layer 1 (Ps)	0.069	1.117	48	25
Layer 2 (Pg)	0.074	1.3	37	22
Layer 3 (Pg/Pc)	0.105	2.618	17	9
Layer 4 (PmP)	0.177	3.133	15	5
Layer 5 (Pn)	0.094	2.115	6	9

3.2 Traveltime inversion of first-arrivals over a uniform grid

A second traveltime inversion algorithm was employed in order to produce an improved subsurface 3D velocity model. The First-arrival Seismic Tomography (FAST) algorithm (Zelt and Barton, 1998) uses only well-constrained first-arrivals and an increased degree of parameterization over a uniform velocity grid to produce a higher-resolution velocity model; traveltimes are calculated using a wavefront-based approach (Vidale, 1988; Hole and Zelt, 1995).

The advantage of applying two independent algorithms to a nonlinear inverse problem is that it provides increased confidence in features that are common to both output models (Zelt and Barton, 1998). Since the algorithm requires no specific identification of phases, reduced subjectivity may result in a less biased output. The high degree of automation of the inversion algorithm is also valuable in developing a completely autonomous model with no dependency on previous results. Despite this, starting velocity profiles, inversion parameters, and stopping criterion remain subjective. Since the FAST algorithm is sensitive to first-arrivals only, models lack the deep ray coverage constraint provided by PmP reflections included in the block model (Figs. 3.2-3.9), and are therefore less informative at depth. The algorithm also traces rays in 3 dimensions, utilizing the true source-receiver geometry and nullifying the innate projection error encountered when translating crooked-line geometry onto a 2D profile.

Although the FAST algorithm requires modeller interaction prior to actually running, once initiated it is a highly automated process, with model and inversion parameters only being adjusted between complete inversion cycles. The algorithm utilizes the Vidale scheme for forward modelling of raypaths, which calculates first arrival traveltimes by solving the eikonal equation through finite differentiation. This method has been modified by the technique of Hole and Zelt (1995) to accommodate strong velocity gradients. Raypaths are given by tracing the steepest gradient of the time field from receiver to source (Zelt and Barton, 1998). The regularized inversion uses a jumping method controlled by smoothness or flatness constraints assigned by the modeller. In doing so, the inversion minimizes a combination of data misfit and model roughness (Zelt and Barton, 1998). Since it is characteristically a non-linear problem, a

starting model and iterative approach are again used, with raypaths being re-calculated for each model iteration.

Source and receiver locations were translated onto a rectangular grid, such as to maintain all relative spatial relationships. The velocity model was specified on a regular velocity grid consisting of nodes at a spacing of 250 m horizontally and vertically, or the same approximate size as the receiver spacing. In the 24-km-wide profile-normal dimension, inversion cells were each 4 km in width, since lack of ray coverage away from the main line means that little resolution was available in this direction. The upper surface of all models was defined by actual topography.

In all models produced in 3 dimensions, all first-arrival wave phases, including Pn, were included in the inversion. The reason for this was that these large-offset arrivals were the rays most affected by 2D projection error, since they travelled the largest distance off-line, and thus their inclusion in the 3D inversions provided the most potential for model improvement. However, in all models the large-scale velocity structure remained essentially consistent, independent of inversion or model parameterization.

All model parameterizations were capable of producing models with normalized χ^2 misfits of near 1.0. Initial parameter values were obtained from suggestions in the software documentation, with a trial-and-error approach being used to select more appropriate values. Alpha, the relative weighting of the flattest versus smallest perturbation regularization, was set to 0.99, giving more importance to flatness of the constraint equations. The relative importance of maintaining vertical versus horizontal flatness, defined by Sz, was set to 0.125 in order to emphasize horizontal flatness. Lambda, the tradeoff parameter that controls the weighting of data misfit versus the constraint equations, was initially set to 100, with a reducing factor of 1.414. During

each iteration, the algorithm automatically detects the optimal flatness tradeoff parameter that provides the better normalized data misfit, leading to a final tradeoff parameter value of 2.21. The result on which the inversion converges is ideally the best model – the most featureless structure which fits the data to within the estimated picking error.

The algorithm traced all upper-crustal refractions as turning within the uppermost 15 km of crust. Raypaths calculated by the gridded first-arrival inversion algorithm are shown in black in figures 3.2-3.9. Since lower-crustal structure was not modified from the starting model, only velocities for the upper 20 km are shown in the final velocity model (Fig. 3.12*b*). 7709 rays were traced for the 3D inversion, giving an RMS misfit of 65 ms and χ^2 of 1.01 after eleven iterations (Fig. 3.12*a*). Shallow velocity structure for the upper 5 km (Fig. 3.12*c*) is especially well-represented by the modelled data, since traveltime picking errors are small for the large-amplitude near-shot arrivals and since ray coverage is excellent in this depth range. However, for some larger-offset ranges (particularly for shots 3 and 10, from 0-35 km model distance), there are some systematic differences between modelled and observed traveltimes (Fig. 3.12*a*) produced because first-arrival ray coverage is poor for these lower-crustal arrivals. That is, structure in the lower crust is mainly constrained by PmP arrivals, not modelled using the first-arrival algorithm. The improved overall fit to the traveltime data that the first-arrival-based algorithm provides is qualitatively evident in analysis of several large traveltime anomalies. Locally-variable details of the traveltime curves from 60-85 km and from 140-175 km (shaded regions in Fig. 3.12*a*) have notably smaller misfits under the first-arrival grid algorithm, relative to the previous block model algorithm. Individual comparisons of observed and modelled traveltime curves are displayed in figures 2.6*b*-2.13*b*. Modelled first-arrivals are those produced by the gridded inversion algorithm,

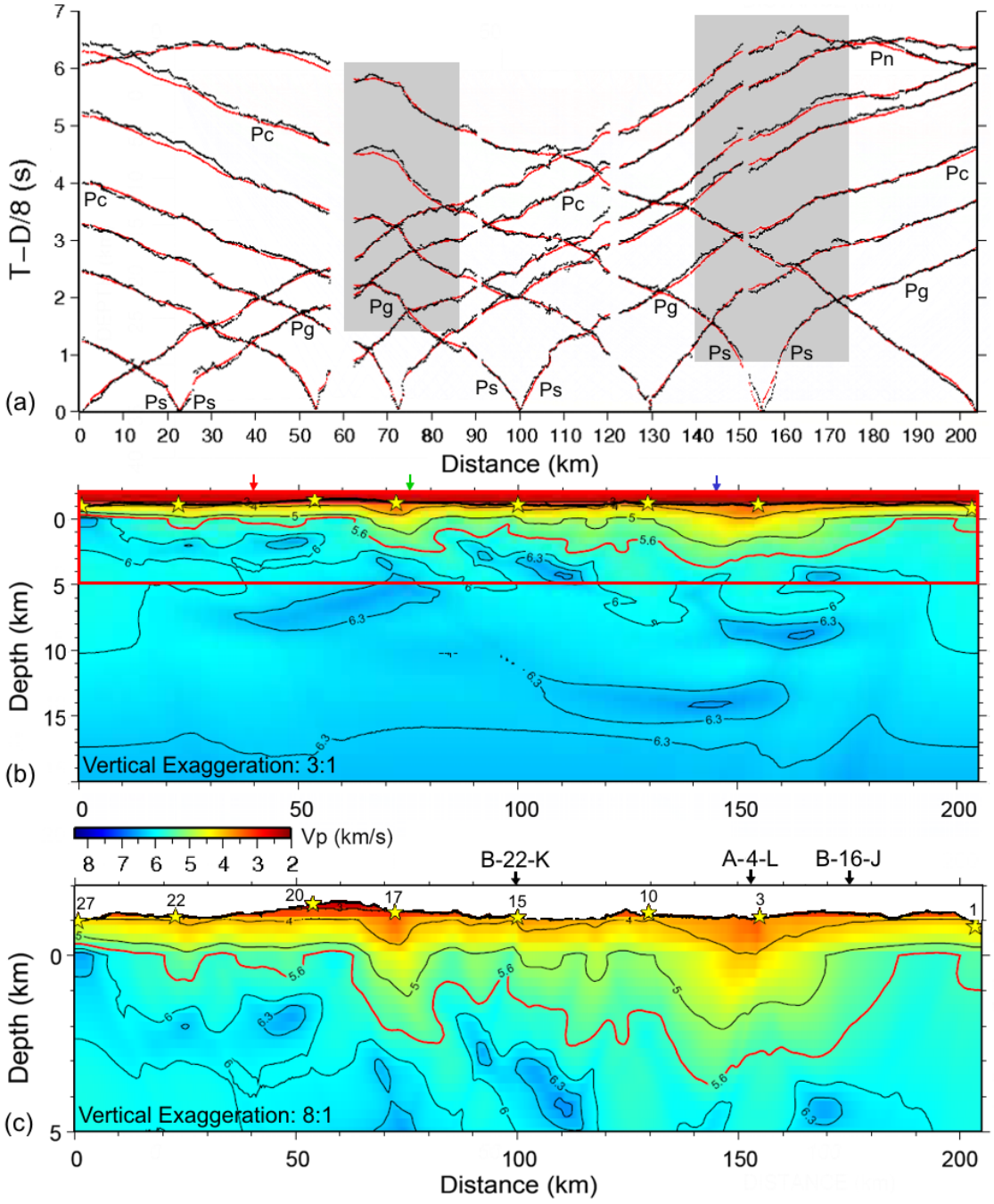

Figure 3.12. *(a)* Observed (black) and modelled (red) traveltimes for first-arrival grid model. Shaded boxes delineate regions of improved fit to the locally-variable traveltime curves. Phases are labelled for shotpoints 3 (22 km), 15 (99 km), and 22 (154 km). Plotted with a reducing velocity of 8.0 km/s. *(b)* Final velocity (Vp) model from first-arrivals. Solid lines indicate velocity contours. The 5.6 km/s velocity contour (thin red line) indicates the interpreted maximum depth of the Nechako Sedimentary Basin. Coloured arrows indicate locations of 1D velocity profiles given in Fig. 4.2. The red box indicates the depth extent of *(c)*, below. *(c)* Final velocity model to 6 km depth from first-arrivals. Projected borehole locations for wells given in Fig. 4.1 are labelled B-22-K, A-4-L, and B-16-J.

while secondary Moho reflections are those synthesized by the layered block model algorithm.

3.3 Lateral resolution of first-arrival velocity model

The final velocity structure is the simplest, most featureless model that fits the observed traveltime data to within the estimated picking error. However, it is necessary to confirm at what scale the features in the model are resolvable, both in terms of spatial size and amplitude. In order to assess the lateral resolution of the output velocity structure, corrugation tests were performed.

To conduct a corrugation test, vertical perturbations of regular and repeating width and amplitude were applied to the output velocity model, forming a corrugated pattern. Variations in slowness of ±10% of velocity values were chosen as being representative of the scale of velocity features observed in the model, corresponding to a 20% total velocity variation. The perturbations were applied to the velocity model at widths varying from 25.5 km to 8.5 km. Random Gaussian noise of 2% was then applied to the velocity model, in order to simulate a real dataset. For a given corrugation width, synthetic traveltimes were generated and used as "observed" data. With the final unperturbed velocity model as an input starting model, the inversion scheme was used to estimate a velocity model from which a set of modelled traveltimes were generated. Lastly, the final unperturbed velocity model was subtracted from the inversion model.

All corrugated output models fit the "observed" perturbation traveltimes with an acceptable RMS misfit of around 65 ms, giving χ^2 of ~1. The reproduced corrugations of all widths exhibit maximum resolvable depths from 100-170 km along the profile, with

reduced resolvability at either end of the survey line (Fig. 3.13). This character corresponds to ray coverage patterns, as expected. Degraded results are to be expected for depths greater than 5-7 km below the surface, as a by-product of greatly reduced ray coverage (Zelt and Barton, 1998). Anomalies of width 25.5 km are resolvable to maximum depths of 4-7 km, the deepest of any of the corrugations tested. As expected, smaller corrugations of 17 km width are resolved to slightly reduced depths of 3-6 km. The narrowest anomalies which are resolvable by the inversion algorithm are 12.75 km in width, imaged to a maximum of 2-5 km depth. Corrugations of width 8.5 km are not clearly resolved by the inversion. Below the depths to which the anomaly pattern is clearly recovered, the corrugations are often observed to maintain the same polarity as the shallower corrugations, but they are usually smeared out along the deep ray paths (Fig. 3.13).

The results of the corrugation tests indicate that the inversion algorithm is capable of resolving features of widths greater than ~13 km, where velocity contrasts are comparable to those observed in the output model. Features larger than 13 km width are resolvable to below-surface depths of at least 5 km in the central slow region, and 2 km at either end of the survey line. Larger features are resolvable to greater depths, with deeper relative resolvability at the slow central-eastern part of the line coinciding with the area of the model with the deepest and most pronounced lateral velocity structure. As expected, the region of deeper resolvability also corresponds to the increased Pg and Pc ray coverage in the model.

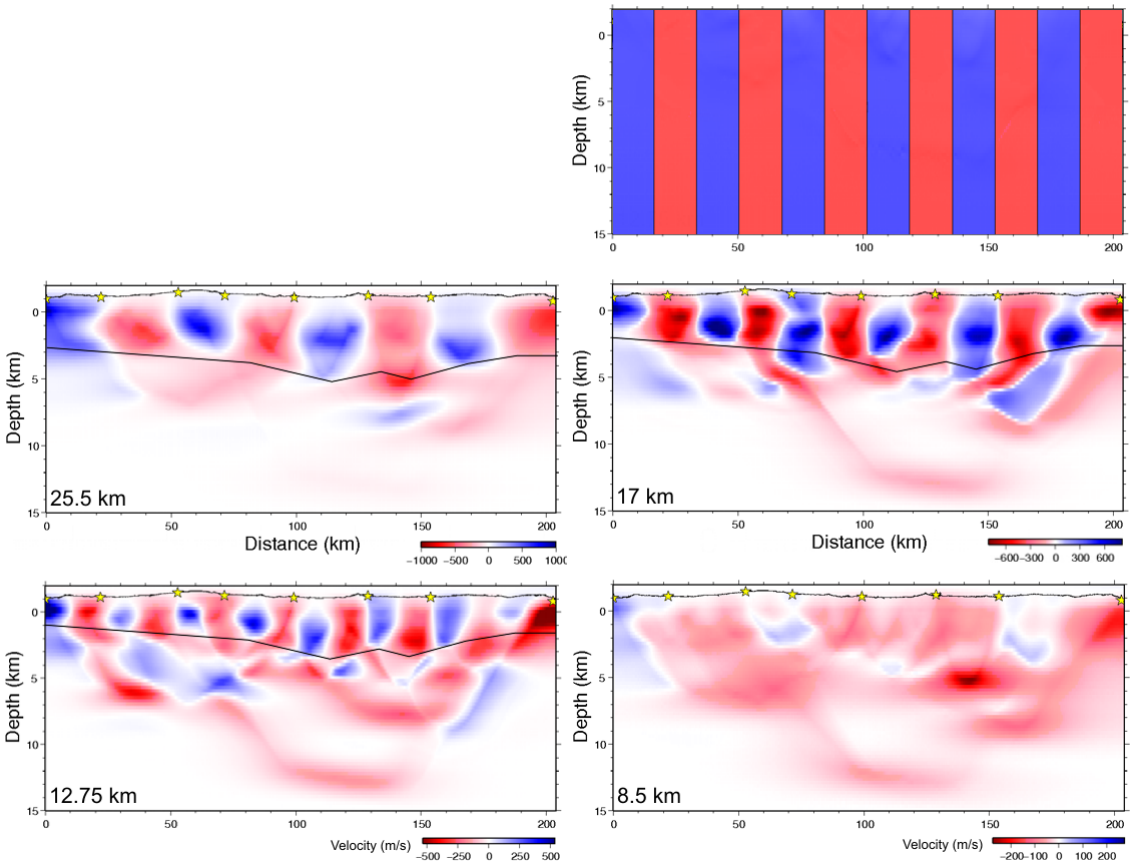

Figure 3.13. Results of corrugation tests for first-arrival grid model. Blue and red corrugations give positive and negative velocity perturbations of 25.5 km, 17 km, 12.75 km, and 8.5 km width. The true corrugation pattern is ±10% of velocity values, shown at the top right for a corrugation width of 17 km. The solid black line gives the approximate maximum depth of resolvability. Note that colour scales increase for increasing corrugation width.

Chapter 4 Velocity model analysis and interpretation

4.1 Near-surface rocks

The output velocity model has surface velocities ranging from 2.5 km/s to 4.2 km/s, generally consistent with shallow tomographic velocity ranges for the Endako and Ootsa Lake groups (2.8-4.6 km/s), sedimentary Taylor Creek Group (2.6-4.6 km/s), and surface Quaternary till (2.0-2.8 km/s) in the vicinity (Hayward and Calvert, 2010*a*). Borehole sonic velocity ranges of the Endako Group (2.8-5.8 km/s), Ootsa Lake Group (2.3-5.1 km/s), and Taylor Creek Group (2.8-4.9 km/s) are much more variable, although they are in general agreement with our near-surface velocities, in an encompassing sense. The Neogene Chilcotin Group basalts are anomalous in that their modelled tomographic velocity range (1.6-3.6 km/s), consistent with our model, is much lower than both borehole sonic (4.2-5.3 km/s) and laboratory sampled (4.5-6.0 km/s) values. The low velocities are attributed to near-surface tomographic sampling of localized porous breccias of the Bull Canyon facies (Hayward and Calvert, 2009*a*).

The lowest surface velocities modelled are ~2.5 km/s, found near 60 km model distance (Fig. 3.12*c*). The thickness of this material is at least 250 m, the depth extent of the near-surface cell. Quaternary till deposits and Chilcotin Group basalts may contribute to these lows. Most near-surface seismic velocities range from 3.3-3.4 km/s, consistent with the results of Hayward and Calvert (2009*a*) from refraction tomographic modelling of 1980's multichannel seismic data. Modelled near-surface velocities are also in good agreement with the sonic logs from boreholes B-22-K, A-4-L, and B-16-J (Fig. 4.1).

No surface volcanic layers were defined in the velocity modelling. Surface volcanic layers are believed to be highly discontinuous both in terms of physical character and thickness, and possibly interbedded with sediments, so it is not surprising that they are not clearly delineated in a model with a 250 m cell size. Also, the velocities of fractured near-surface volcanic rocks are not distinct from shallow sedimentary rocks, and several shotpoints may be located below the base of the volcanics.

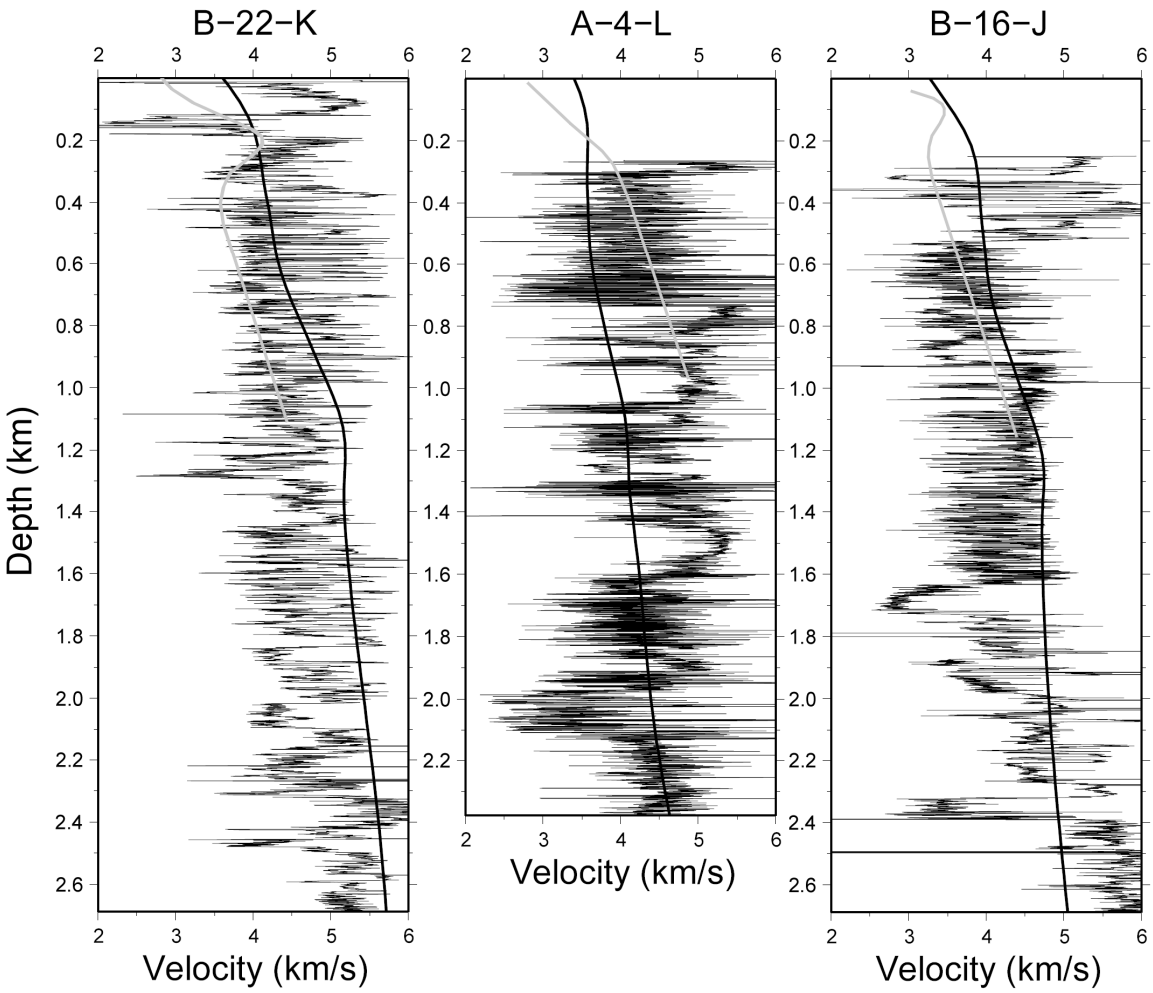

Figure 4.1. Comparison of seismic velocity models with borehole sonic logs. Thin black line shows the borehole sonic log. Thick black line shows 1D velocity profile from Fig. 3.12*c*, taken from the nearest along-strike point of the BATHOLITHS*onland* survey line (indicated by respective borehole numbers along the top of Fig. 3.12*c*). Light gray curves in the upper ~1 km are from the tomographic velocity model of Hayward and Calvert (2010*a*).

4.2 Sedimentary basin and upper crust

4.2.1 Seismic model velocities

The greatest velocity variations are found within the uppermost 5 km of crust (Fig. 3.12*c*), a region that is well-constrained by the highest density of ray coverage in the model. Ray coverage decreases considerably below 5 km depth, especially along the western half of the profile, as a result of a weak velocity gradient with depth rather than survey limitations. Velocity structure is very similar in models developed by two independent methods (Figs. 3.11*c*, 3.12*b*).

In the tomographic velocity model (Figs. 3.12*b, c*), velocities increase rapidly with depth within the uppermost layer. However, the depth to the 5.0 km/s velocity contour varies significantly between model distances 65 km and 175 km, from 2.5 km to about 3.3 km. Similar variations are seen in the depth to the 5.6 km/s contour, which is found ~1-2 km deeper than the 5.0 km/s contour in the central part of the profile (Fig. 3.12c). For velocities higher than ~6.0 km/s the velocity gradient becomes much smaller (Fig. 4.2), with velocities increasing to 6.3 km/s at an average of 17 km depth (Fig. 3.11*c*). As well, the depth to the 6.0 km/s contour exhibits more irregular variations along the profile, compared to the "in-step" variations shown by the near-parallel 4.0, 5.0 and 5.6 km/s contours.

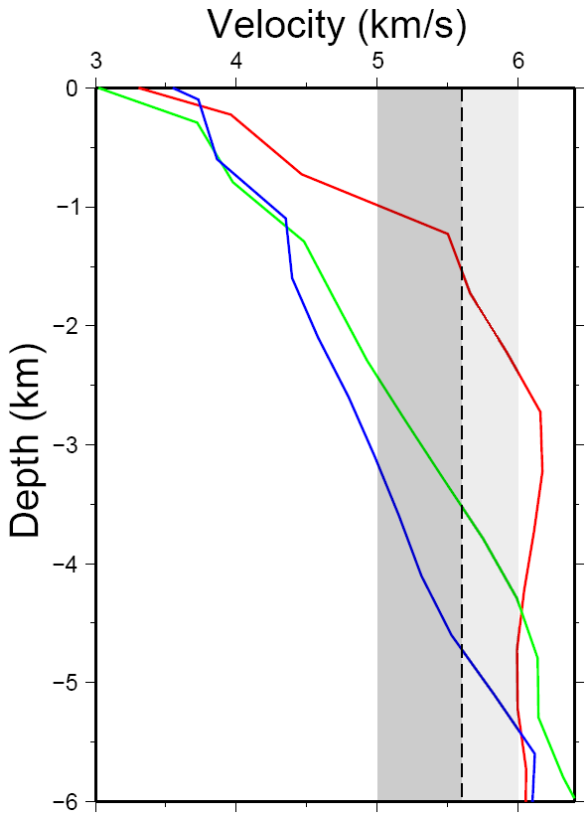

Figure 4.2. 1D velocity profiles taken at model distances of 40 km (red), 75 km (green) and 145 km (blue). Locations are given by coloured arrows along the top of Fig. 3.12*b*. The dashed line corresponds to the red 5.6 km/s contour in Figs. 3.12*b,c*. The gray shaded region between 5.0 km/s and 5.6 km/s represents the possible velocity range of interlayered sediments and volcanics, with light gray from 5.6-6.0 km/s representing continued interbedding or shallow volcanic arc terrane.

4.2.2 Seismic velocities and inferred lithology

We consider that the base of the Nechako Basin sedimentary package corresponds to a seismic velocity of 5.0 km/s, as a maximum (Figs. 3.12*c*, 4.2). Well logging and core data from 1960's and 1980's boreholes provide the most direct control on near-surface lithology, velocity, and density for application to velocity and gravity modelling. Core samples provide absolute thicknesses of the surface volcanics and sedimentary basin, and act as some of the most reliable model constraints.

Four boreholes are located within ~25 km of the BATHOLITHS*onland* profile: B-22-K, D-96-E, A-4-L, and B-16-J (Fig. 2.1). Considerable surface volcanic thicknesses of ~600 m and ~500 m are recorded for boreholes B-22-K and B-16-J (Ferri and Riddell, 2006). These wells are both located within regions of Tertiary volcanic surface cover (Fig. 2.1), but much of this cover may have been eroded and replaced by Quaternary till along the seismic profile to the south, based on lack of surface exposures. The velocity model is in reasonably good agreement with borehole sonic logs for the upper ~2.6 km of crust (Fig. 4.1), although some discrepancies are expected since the wells are located ~10-25 km from the seismic line. Borehole data from the upper kilometre of well D-96-E limits the seismic velocity of the sedimentary Taylor Creek Group to 5.0 km/s, generally consistent with modelled seismic velocities of up to 4.6 km/s based on multichannel seismic data (Hayward and Calvert, 2010*a*). Boreholes D-96-E and A-4-L, those with the thickest verified sedimentary packages of 2950 and 2650 m, respectively (Riddell, 2009), are projected ~15 km onto the thickest sub-basin of the model.

Cumming et al. (1979) analysed data from a 440 km line crossing the Intermontane Belt (dataset "2" – Fig. 4.3). They modelled a ~1.3 km thick surface layer with a velocity of 4.50 km/s, approximately equivalent to the average velocity at depths above our 5.0 km/s contour, or ~1-2 km depth. Zelt et al. (1992) interpreted a thin near-surface layer along SCoRE Line 1 (Fig. 4.3) averaging 2.5 km thickness. The layer was defined by velocities ranging from 2.8-5.4 km/s and averaging 4.5 km/s - parameterized very similarly to our interpreted sedimentary basin. Within borehole D-96-E, the base of the sedimentary rock is located at 2.95 km depth (Riddell, 2009). Translating the

borehole 10 km along-strike, and assuming minimal structural variation over this distance, the basement ties to a modelled seismic velocity of about 5.2 km/s.

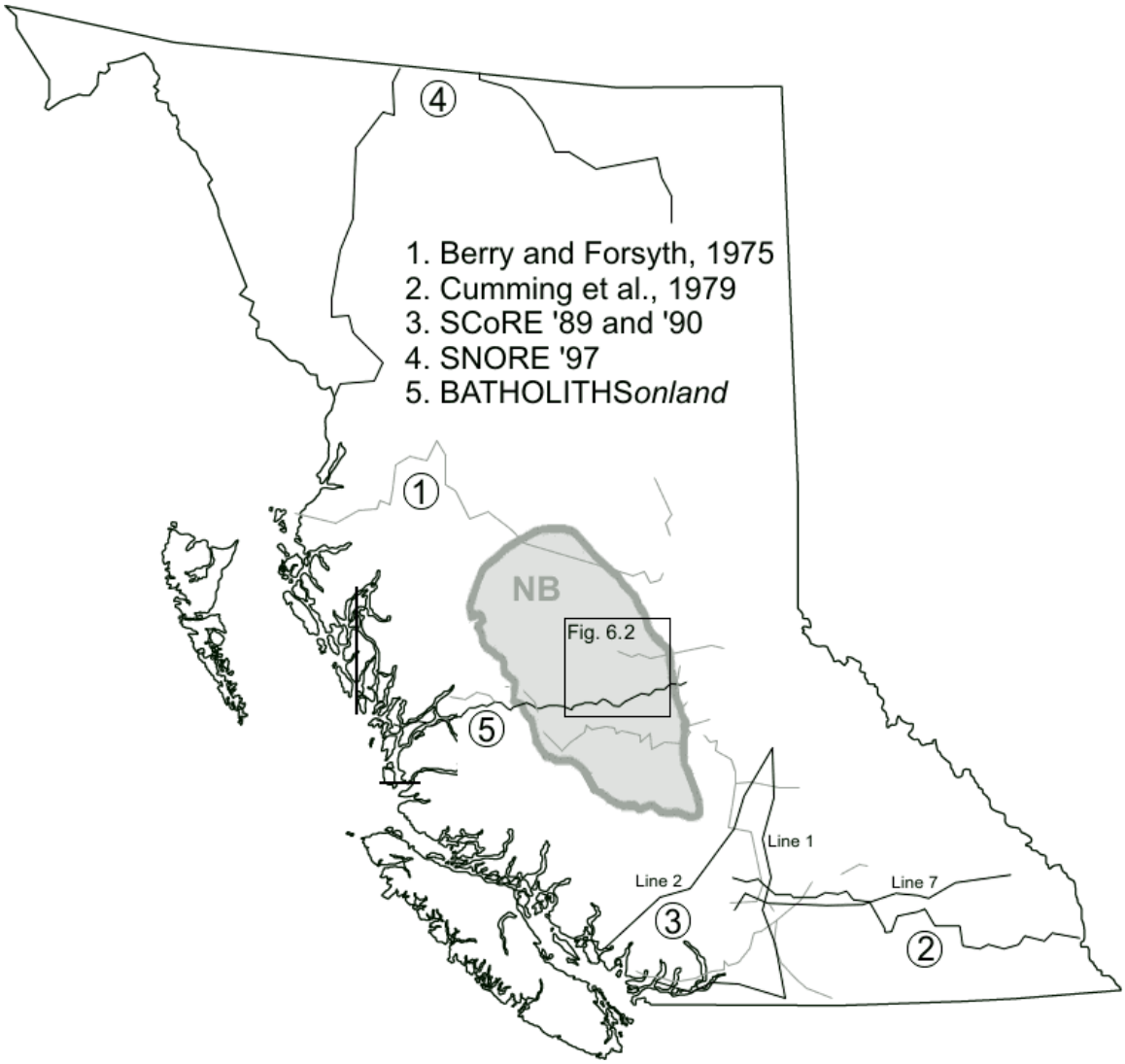

Figure 4.3. Map of seismic refraction experiments within the Intermontane Belt of the Western Canadian Cordillera. The labelled lines 1, 2, and 7 correspond to the SCoRE ’89 and ’90 experiments. NB, Nechako Basin.

For seismic velocities between about 5.0 km/s and 5.6 km/s, it is difficult to distinguish between deep lithified sedimentary rocks and volcanic basement rocks. In the early stages of basin formation, basalts and sedimentary rocks could even be interlayered.

As an example of high velocities suggested for sedimentary rocks, Ramachandran et al. (2004) interpreted velocities up to 5.5 km/s to represent sedimentary rocks in the Insular Belt near Vancouver Island. Zelt et al. (2001) even suggested that deeper Cretaceous sediments in the Nanaimo basin may have velocities up to 6.0 km/s due to compaction and lithification. Similarly, Hammer et al. (2000) attributed velocities of 3.4-5.6 km/s to sedimentary rocks of the Bowser Basin, overlying the Stikine Terrane to the north. In contrast, basalt basement rocks at depths less than 5 km may have seismic velocities in the 4.5-5.5 km/s range (5.5-6.5 km/s at greater depths), based on laboratory, borehole, and seismic tomographic measurements (Van Wagoner et al., 2002).

In our Nechako Basin velocity model, we interpret velocities from 5.0 km/s to 5.6 km/s as interlayered sediments and volcanics (Fig. 4.4). Velocities from 5.6-6.0 km/s may represent continued interbedding, or shallow Stikine Terrane. That is, we suggest that basin formation was accompanied by syn-rift sedimentation and volcanism, as observed for the Bowser Basin and Stikine basement to the north (Hammer and Clowes, 2004). This type of interlayered sediments and volcanics has also been inferred for the Miocene Queen Charlotte Basin, where rifting was accompanied by strike-slip fault formation in a transtensional environmental (Rohr and Dietrich, 1992). In Nechako basin, velocities higher than 6.0 km/s are interpreted as arc volcanic basement rocks of the Intermontane Belt continental crust – likely the Stikine and Cache Creek terranes. In the northern Cordillera, velocities of 6.0-6.2 km/s were associated with shallow (<5 km) Stikine Terrane, representing imbricated sedimentary and volcanic rocks (Hammer and Clowes, 2004).

4.2.3 Nechako Basin sedimentary and basement rocks

The core of the Nechako Basin is bounded laterally by model distances of 65 km and 175 km. Extension associated with re-activated Eocene sub-basin formation was focussed in this core region, in contrast to the neighbouring segments. However, localized increases in basin thickness indicate that extension was laterally variable.

The most prominent features of the model are two large sub-basins located between model distances of 65-85 km and 130-175 km (Fig. 3.12*c*). Velocity-depth profiles in the centres of the sub-basins are shown in Figure 4.2. In the western sub-basin (green curve in Fig. 4.2), velocities increase from 3.0 km/s at the surface to 5.0 km/s at 2.5 km depth. In the eastern sub-basin (blue curve in Fig. 4.2), velocities are 3.6 km/s at the surface and 5.0 km/s at 3.5 km depth. The region between the sub-basins, between model distances of 85 km and 130 km, also exhibits local deepening of the 5.0 km/s velocity contour, although the features are poorly resolved since their widths are slightly less than the 13 km lateral resolution limit. These structures may reflect segmentation in the basin similar to that interpreted by Hayward and Calvert (2009*a*), who inferred that several small sub-basins are separated by north-south strike-slip faults.

The seismic velocity model shows that the western edge of greatest sedimentary thickness is located at a model distance of 65 km (Fig. 4.4). A dramatic thinning of more than 2.0 km is interpreted to occur over a lateral distance of only 10 km, so if the basin does extend west of model distance 65 km, it is at a considerably reduced thickness of less than ~1 km. In previous geological investigations, the western edge of the basin was mapped as extending to approximately 20 km model distance (Fig. 1.2 - BC Ministry of Energy, Mines and Petroleum Resources, 2002). Recent studies of the Dean River

metamorphic belt in the Anahim Lake area appear to be consistent with the interpretation of the seismic velocity model. These studies indicate that the western edge of the basin may be more accurately located east of its previously mapped location, to somewhere between shotpoints 20 and 17 (Figs. 1.2, 4.4), or between model distances of about 55 km and 70 km (J.M. Riddell and M.G. Mihalynuk, personal communication, 2010).

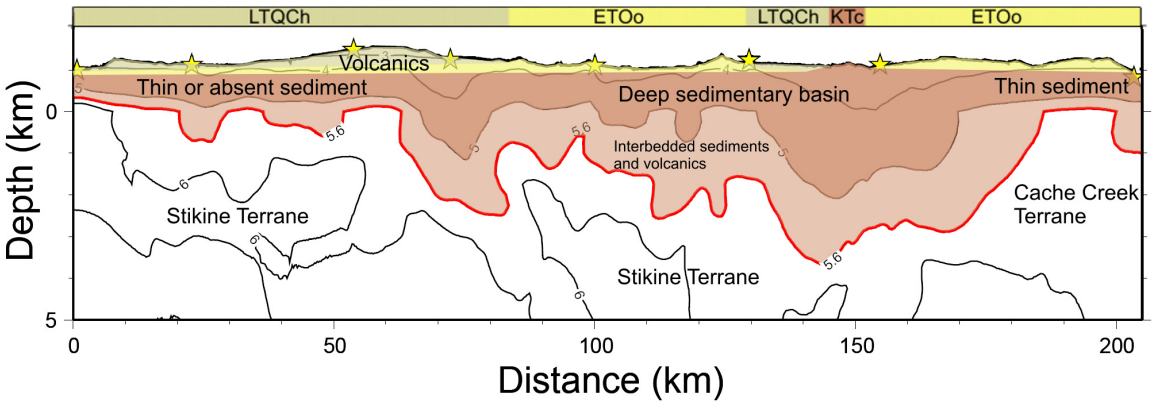

Figure 4.4. Interpreted extent of the Nechako Sedimentary Basin; the thick red line corresponds to a velocity value of 5.6 km/s (Fig. 3.12*c*), above which contours appear to show lateral consistency. The sedimentary package is overlain by Tertiary surface volcanics, and bounded below by the 5.0 km/s velocity contour. Interbedded sediments and volcanics underlie the basin from 5.0-5.6 km/s, forming a transitional zone into volcanic rock of the accreted terranes below. Velocities from 5.6-6.0 km/s may represent continued interbedding, or shallow Stikine Terrane. Simplified surface geology is shown at top, excluding Quaternary cover. ETOo, Ootsa Lake Group volcanics; KTc, Taylor Creek Group sandstones; LTQCh, Chilcotin Group volcanics.

The easternmost 25 km of the profile is likely underlain by Cache Creek terrane; structure is uniform laterally, and the depth to velocities >5.0 km/s is only ~1.0 km (Figs. 3.12*c*, 4.4). In the westernmost 60 km of the profile, underlain by Stikine terrane, the depth to 5.2 km/s is also ~1 km in general. The basement is shallow, with a velocity of 5.0 km/s at a depth of only ~1.0 km (red curve in Fig. 4.2). In two localized regions (~10 km in width) near model distances of 25 km and 45 km, the 5.6 km/s contour deepens slightly, although contours of 5.0 km/s or less are laterally uniform (Fig. 3.12*c*).

4.3 Lower crust and mantle

4.3.1 Seismic model velocities

Lower crustal velocities are defined mostly by modelling of wide-angle Moho reflections and mantle refractions (Fig. 3.11*a*). Modelled crustal structure below 10 km depth is more laterally homogeneous than structure in the upper crust, although this could be due partly to reduced ray coverage and hence reduced information about the lower crust. Regardless, the average vertical velocity gradients are much smaller in the lower crust compared to the upper crust. Velocities increase from ~6.1 km/s at 10 km depth, to 6.5 km/s at 23 km depth. The velocity-depth profile of the volcaniclastic Stikine Terrane is consistent with metamorphosed granitic and basaltic lithologies (Christensen and Mooney, 1995). The Moho discontinuity is modelled at a fairly uniform depth of 33.5-35 km, with little variation observed along the 205-km-long line (Fig. 3.11*c*). Velocities at the base of the crust range from 6.8 km/s to 7.0 km/s, with an average of 6.9 km/s. The velocity of the mantle just beneath the Moho is equal to 8.05-8.10 km/s (Fig. 3.11*c*), consistent with the global average of 8.09 ± 0.20 km/s (Christensen and Mooney, 1995).

Other seismic refraction studies of the Intermontane Belt (Fig. 4.3) suggest similar crustal velocities and mantle depths as those interpreted here, while upper mantle velocities are typically lower (Table 4.1). The earliest major refraction survey was completed in 1971, and consisted of eight shotpoints recorded by 300 receivers (dataset "1" – Fig. 4.3). Berry and Forsyth (1975) modelled an average crustal velocity from 6.30-6.50 km/s for the Intermontane Belt, in general agreement with our results. An upper mantle velocity of 8.06 km/s was interpreted just to the north of the

BATHOLITHS*onland* profile. The results are also consistent with the value of 8.10 km/s obtained by White et al. (1968) for the central-northern Cordillera.

LITHOPROBE's Southern Cordillera Refraction Experiments (SCoRE '89 and SCoRE '90) included one full line (Line 1) and parts of several others (Line 2, Line 7) that crossed the southern Intermontane Belt (Fig. 4.3). Similar upper-crustal velocities of ~6.0-6.3 km/s were obtained along these lines (Zelt et al., 1996; Spence and McLean, 1998). Modelling of wide-angle seismic data 200-400 km to the southeast within the Intermontane Belt has generated comparable average lower-crustal velocities of ~6.7-6.9 km/s, but slightly reduced upper mantle velocities of 7.8-8.0 km/s (e.g., Burianyk and Kanasewich, 1995; Zelt et al., 1996; Spence and McLean, 1998). These low values corroborate the earlier findings of White et al. (1968) and Berry and Forsyth (1975), who interpreted upper mantle velocities of 7.80 km/s and 7.83 km/s, respectively, within the southern Intermontane Belt. In the northern Cordillera, similar crustal velocities are interpreted (Table 4.1), along with upper mantle velocities of 7.7-7.9 km/s (Welford et al., 2001; Creaser and Spence, 2005).

It thus appears that high upper mantle seismic velocities of 8.05-8.10 km/s in the central Cordillera, as represented by the BATHOLITHS*onland* results in the Stikine Terrane, are distinct from mantle velocities of ~7.80 km/s in the Cordillera to the north and south (Fig. 4.5; Table 4.1). The reason for the higher upper mantle velocities in the central Intermontane Belt is uncertain. As discussed by Currie and Hyndman (2006), velocities and corresponding densities must eventually decrease within the mantle to provide isostatic support of the high elevations within the Cordillera, including the Interior Plateau.

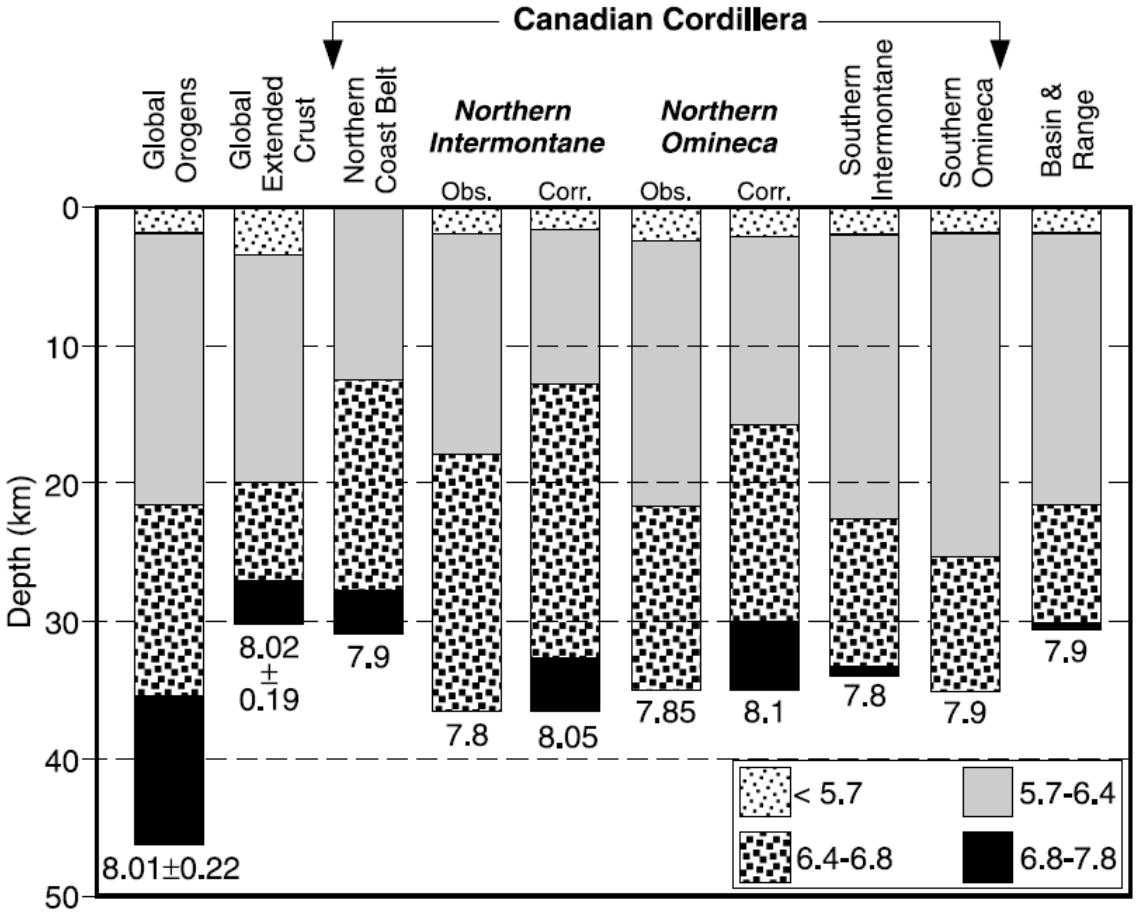

Figure 4.5. Crustal thicknesses and velocities of the Western Canadian Cordillera (Hammer and Clowes, 2004), including the northern and southern Intermontane Belt. P-wave velocities are given in km/s. Obs., observed thermal gradient of ~100 mW/m^2. Corr., thermal correction to a low heat flow of ~40 mW/ m^2.

4.3.2 BATHOLITHS*onland* full-line results

Similar velocities for the lower crust and mantle are obtained in preliminary modelling of the full BATHOLITHS*onland* seismic profile, in which Moho reflections and mantle arrivals from shots in the Coast Batholith (Fig. 1.2) are also included (Wang et al., 2010). Near-surface low velocity zones inferred to represent the largest sedimentary sub-basins are centered at ~145 km and ~65 km (Fig. 4.6), locations that coincide with our results (Fig. 3.12*c*). The interpreted thickness of Mesozoic sedimentary and volcanic rock is

Table 4.1. Lithospheric velocities of the Intermontane Belt from seismic refraction studies. Velocities and Moho depths are approximate averages. Note that upper mantle velocities within the central Cordillera, as highlighted by the box, appear to be higher than in the northern or southern Cordillera. UC, upper crust; LC, lower crust; UM, upper mantle.

	Survey	UC (km/s)	LC (km/s)	Moho (km)	UM (km/s)	Reference
N. Cord.	SNORE '97		6.5-6.7	35	7.8-7.9	Zelt et al., 2006
		6.2-6.4	6.5-6.6	36	7.7-7.9	Creaser and Spence, 2005
		6.2-6.4	6.6-6.7	35-36	7.8	Hammer and Clowes, 2004
C. Cord.	1971 survey (central)	6.1-6.4	6.6	35	8.06	Berry and Forsyth, 1975
	BATHOLITHS*onland*	6.1-6.5	6.8-7.0	33.5-35	8.05-8.10	Stephenson et al., 2010
S. Cord.	1971 survey (south)		>6.5	35	7.83	Berry and Forsyth, 1975
	1973-1975 survey	6.05	6.9	33	7.8	Cumming et al., 1979
	SCoRE '89 and '90	6.0-6.4	6.7-6.8	35	7.9-8.0	Spence and McLean, 1998
		6.0-6.3	6.6-6.8	33-36	7.85	Zelt et al., 1996
		6.0-6.3	6.6-6.7	34	8	Burianyk and Kanasewich, 1995

also consistent at 2-5 km, indicated by velocities of ~4-5 km/s (Wang et al., 2010). However, the near-surface velocities of Wang et al. (2010) are generally lower, with a reduced velocity gradient over the uppermost ~5 km of crust, and a low velocity of 4.5 km/s extending to ~5 km depth within the main basin. Rocks of the underlying Stikine Terrane correspond to velocities of ~5.8-6.2 km/s, to at least 15 km depth (Wang et al., personal communication, 2010). A seismic reflector, absent from our model, was interpreted at ~20 km depth (Fig. 4.6). The reflector was interpreted from just west of the midpoint of the full 400 km line to a location ~35 km from the survey's eastern end. Mid-crustal velocities of ~6.5 km/s and values of ~7 km/s near the base of the crust are comparable to our results. Over the eastern 205 km of the full profile, a significant

amount of variation in the depth to the Moho is interpreted, with values ranging from 36-39 km – deeper and more variable than the values defining our interpreted crust-mantle interface. Upper mantle velocity is modelled at slightly faster than 8.0 km/s for the eastern half of the full BATHOLITHS*onland* survey line (Wang et al., 2010).

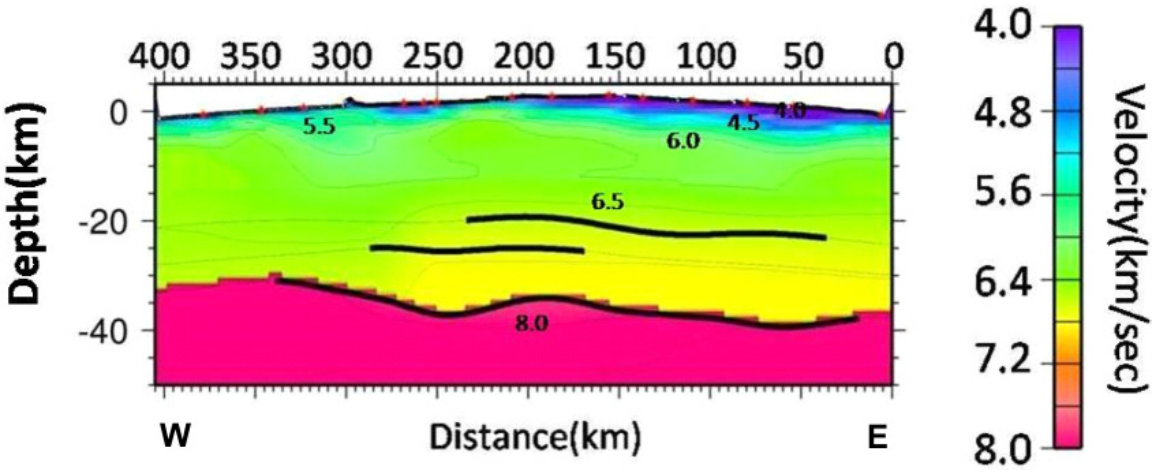

Figure 4.6. BATHOLITHS*onland* full-line velocity model (Wang et al., 2010). Low velocities of the Nechako Basin are observed in the uppermost crust along the eastern half of the survey.

4.3.3 Moho depth

Crustal thickness appears relatively uniform throughout much of the Intermontane Belt. The modelled Moho discontinuity at a depth of ~35 km is consistent with previous interpretations of 35 ± 2 km (Berry and Forsyth, 1975), 33-36 km (Zelt et al., 1996) and 34-35 km (Spence and McLean, 1998), as derived from seismic refraction/wide-angle reflection data. Such uniform mantle depths beneath the basin mean that there is currently no crustal thinning present at the base of the crust, in contrast to what might be expected for an extensional model of basin formation.

Chapter 5 Gravity Modelling

Gravity modelling, with densities constrained by the seismic velocity model, was conducted in order to determine if any anomalous density regions were present within the survey area. The incorporation of gravity data provides additional control on the interpretation of upper-crustal structure.

5.1 Description of gravity data

Using regional Bouguer gravity data gridded at 2 km (Fig. 5.1*b,* Natural Resources Canada - Geoscience Data Repository), three linear and parallel profiles were extracted from the approximate line of best fit of the receiver line, as well as from 10 km to either side (Fig. 5.1). All receivers were located within the ~20 km section bounded by the two outside profiles. The three gravity profiles were averaged in order to obtain a gravity profile most representative of the survey line (Fig. 5.1*a*), minimizing the impact of the considerable north-south gravity heterogeneity. The gravity data display a subdued relief, with generally small short-wavelength perturbations of less than ~15 mGal. Near the eastern end of the line, a larger wavelength Bouguer anomaly with an amplitude of ~20 mGal is observed (Fig. 5.1*a*). Since the 2.5D profile used for modelling is an average, the strongest anomalies are produced in locations where gravity highs or lows are laterally consistent across the three profiles (ie. Fig. 5.1, near shotpoint 17 and east of shotpoint 3).

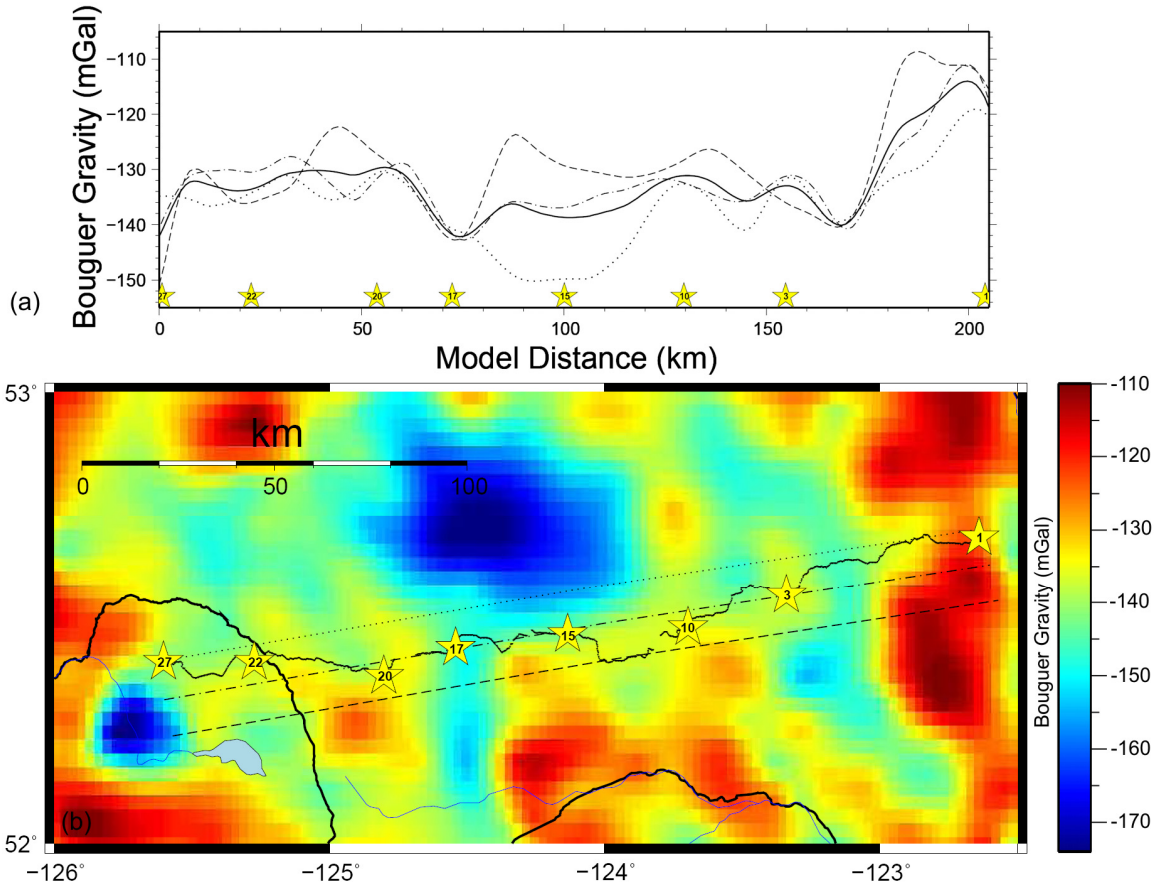

Figure 5.1. *(a)* Bouguer gravity profiles averaged for 2.5D modelling of gravity data. The averaged profile is indicated by a solid line, with the locations of the three constituent lines shown on the Bouguer gravity anomaly map in *(b)*. Gravity values are from NRCan's 2 km Bouguer grid.

5.2 Methodology

Gravity modelling was performed with Grav2dc, a 2.5D modelling program (Cooper, 2003). The final gridded velocity model was converted to a density model, with modelled layer boundaries controlled by a smooth version of the velocity boundaries, and densities controlled by the velocity-density relation of Barton (1986). Small-scale adjustments were made to density, since the modelled velocities have uncertainties and the velocity-density relation has error bounds (Fig. 5.2). A sort of reverse layer-stripping

approach was followed, in which deeper structure was modelled first since it controls the broad-scale features of the gravity data. The final density model consists of 6 layers, with layer thicknesses generally increasing with depth (Fig. 5.3*c*; Table 5.1). Since the Bouguer anomaly corrects for elevations, the top surface of the model is flat and assigned to an elevation of ~1.1 km, approximately equal to the average elevation along the profile. The model was extended by 200 km on either end of the survey line, in order to mitigate edge effects.

Table 5.1. Gravity modelling results including layer composition, velocity, and density.

	Lithology	Velocity (km/s)	Density (g/cc)
surface LVZ's	Quaternary till	2.00-2.80	2.100
Layer 1	Nechako Basin sedimentary rock	~4.50	2.545
Layer 2	overlapping sediments/volcanics	5.00-5.60	2.560
Layer 3	Stikine/Cache Creek terrane	~5.80	2.700
Layer 4	Stikine volcanic arc terrane	~6.00	2.690
Layer 5	Stikine volcanic arc terrane	~6.55	2.795
Layer 6	upper mantle	8.05-8.10	3.350

5.2.1 Starting density model constraints

The base of the uppermost layer of the block model (Layer 1) was approximated by the 5.00 km/s contour (Fig. 5.3*b*). Near-surface densities were constrained by density logs from boreholes B-22-K and B-16-J, to depths of 3.12 km and 2.6 km, respectively. From the surface to the 5.00 km/s velocity contour, a density of 2.545 g/cm^3 for sedimentary rock of the Nechako basin was selected as optimal for forward modelling. The value falls near the middle of the borehole range of 2.30-2.60 g/cm^3 obtained for the upper 3 km of crust. For an average velocity of ~4.50 km/s between the 5.00 km/s contour and the

surface (Fig. 4.1), the output density value is also consistent with the velocity-density relation curve (gray circles and shaded region on Fig. 5.2).

The region between the 5.00 km/s and 5.60 km/s velocity contours is interpreted as a transition zone between sediment of the Nechako Basin and underlying accreted terrane. As discussed in Chapter 4, it perhaps represents imbricated sediments and volcanics (Hammer and Clowes, 2004). A density of 2.560 g/cm^3 was obtained for this intermediary zone denoted Layer 2, consistent with all velocities across the 0.60 km/s-wide velocity range (Fig. 5.2). The density is also in agreement with the log data from boreholes B-22-K and B-16-J, where a density of 2.560 g/cm^3 is found at an average depth of 2.2 km. When projecting the boreholes 10-25 km to the south, onto the density model, the depth of 2.2 km is observed to be located within this layer.

A density block model interface was fitted to the 5.60 km/s contour, approximating the top of interlayered igneous basement rock (Fig. 5.3*b*). The density model region between the 5.60 km/s velocity contour and 5 km depth is interpreted as accreted terrane of the Cache Creek and Stikine arcs, with potentially some of the deepest interlayered sediments and volcanics in the upper part of the layer, between the 5.6 km/s and 6.0 km/s contours. Layer 3 has an average velocity around 5.80 km/s. The density of the upper-crustal Cache Creek Terrane was derived from measurements of mafic rocks made in the southern Yukon by Tempelman-Kluit and Currie (1978) and Lowe et al. (1994). A density value of 2.700 g/cm^3 for this region (Layer 3) is in agreement with that of Creaser and Spence for the Cache Creek Terrane (2.720 g/cm^3), and consistent with the velocity-density curve for the corresponding range of velocity values (Fig. 5.2). For Layers 1-3, the thin layers are consistent with the strong velocity gradient characterizing

the final velocity model (Fig. 3.12*c*), representing strong lithological contrasts in the near-surface.

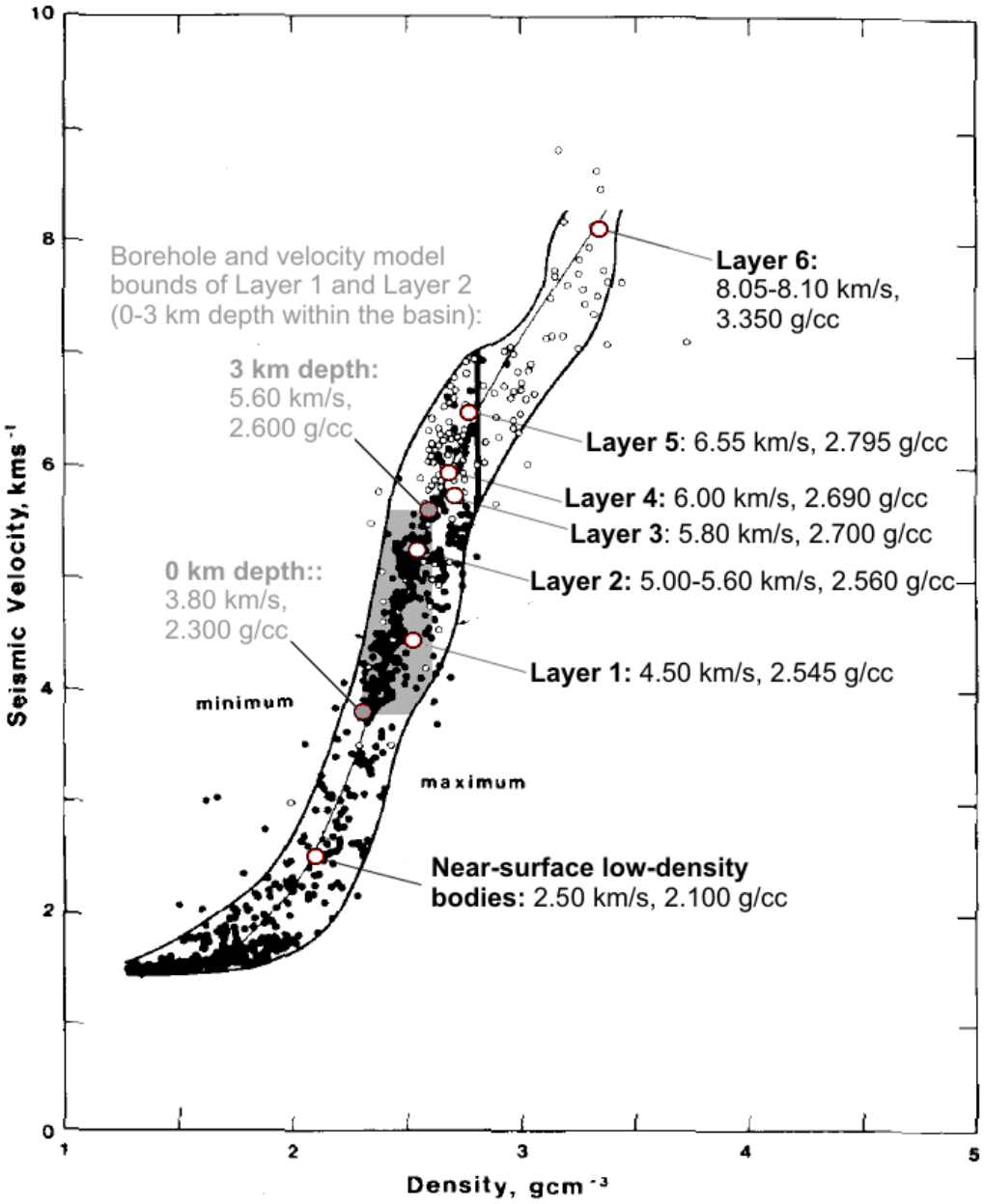

Figure 5.2. P-wave seismic velocity-density relation from observations of continental crust (modified from Barton, 1986). Open circles correspond to measurements made from metamorphic and igneous rocks, and filled circles represent sedimentary rocks. Velocities and densities parameterizing the five-layer density model are plotted and labelled as large open circles, all of which fall on or near the mean velocity-density relationship curve (thin solid line). The gray zone represents the borehole constraint on Layer 1, from the surface to 3 km depth.

Mid-to-lower crustal densities were estimated using the velocity-density relation provided by Barton (1986), in conjunction with the P-wave velocities of the two final velocity models (Figs. 3.11, 3.12). A ~10 km thick Layer 4 from ~5-15 km exhibited minimal variation from an average velocity of 6.00 km/s. A density of 2.690 g/cm^3 is consistent with the constraints provided by Barton's velocity-density relation (Fig. 5.2).

A lower crustal density of 2.795 g/cm^3 was obtained via trial and error forward modelling, as constrained by the velocity-density relation curve (Barton, 1986) and an average velocity of 6.55 km/s (Fig. 3.11). Because the velocity varies by less than 0.7 km/s over the 20 km depth range of Layer 5, a single assigned density was sufficient for modelling purposes. A small amount of structure was inserted within the upper boundary of this layer, with the western half deepening by 1-2 km in order to better fit the general gravity trend, and counteract the effect of the low-density basinal rocks thickening to the east (Fig. 5.3*c*). The deepening had no effect on consistency with the velocity model (Fig. 5.3*c*), because the low velocity gradient ensured that velocities both above and below the relocated density interface remained well within the bounds of the relation curve (Fig. 5.2).

Moho structure of the density model was obtained directly from the layered block velocity model (Fig. 3.11*c*). A mantle density of 3.350 g/cm^3 for Layer 6 was similar to the 3.330 g/cm^3 value given by Barton (1986), and equal to the value modelled by Creaser and Spence (2005) in the northern Cordillera.

5.3 Results

5.3.1 Direct conversion model analysis

The six-layer direct conversion model (Fig. 5.3*c*) provides a reasonable fit to the general gravity trend of the line (Fig. 5.3*a*), and an especially good fit to gravity features which are laterally continuous across the three averaged profiles, such as the gravity lows at 75 km and 145 km model distance (Fig. 5.3*a*). The direct conversion model also provides a good fit to the 20 mGal high anomaly along the eastern end of the profile, inferred to represent shallow high-velocity Cache Creek Terrane bounding the eastern edge of the deep part of the Nechako Basin. High relative gravity values along the western ~65 km of the profile coincide well with our interpreted extent of shallow Stikine Terrane, bounding the western edge of the sedimentary basin. In regions where gravity values vary considerably across the three averaged profiles, misfit of the direct conversion model is larger, as expected, due to the less representative gravity values provided by the averaged profile. The most obvious example of this is found between model distances of 85 km and 120 km, where gravity values taken along the northernmost profile are much lower than those of the southernmost line (Fig. 5.1). These short wavelength oscillations were unlikely to be fit by the direct conversion model (Fig. 5.3*a*), since they likely result from small-scale features in the near surface.

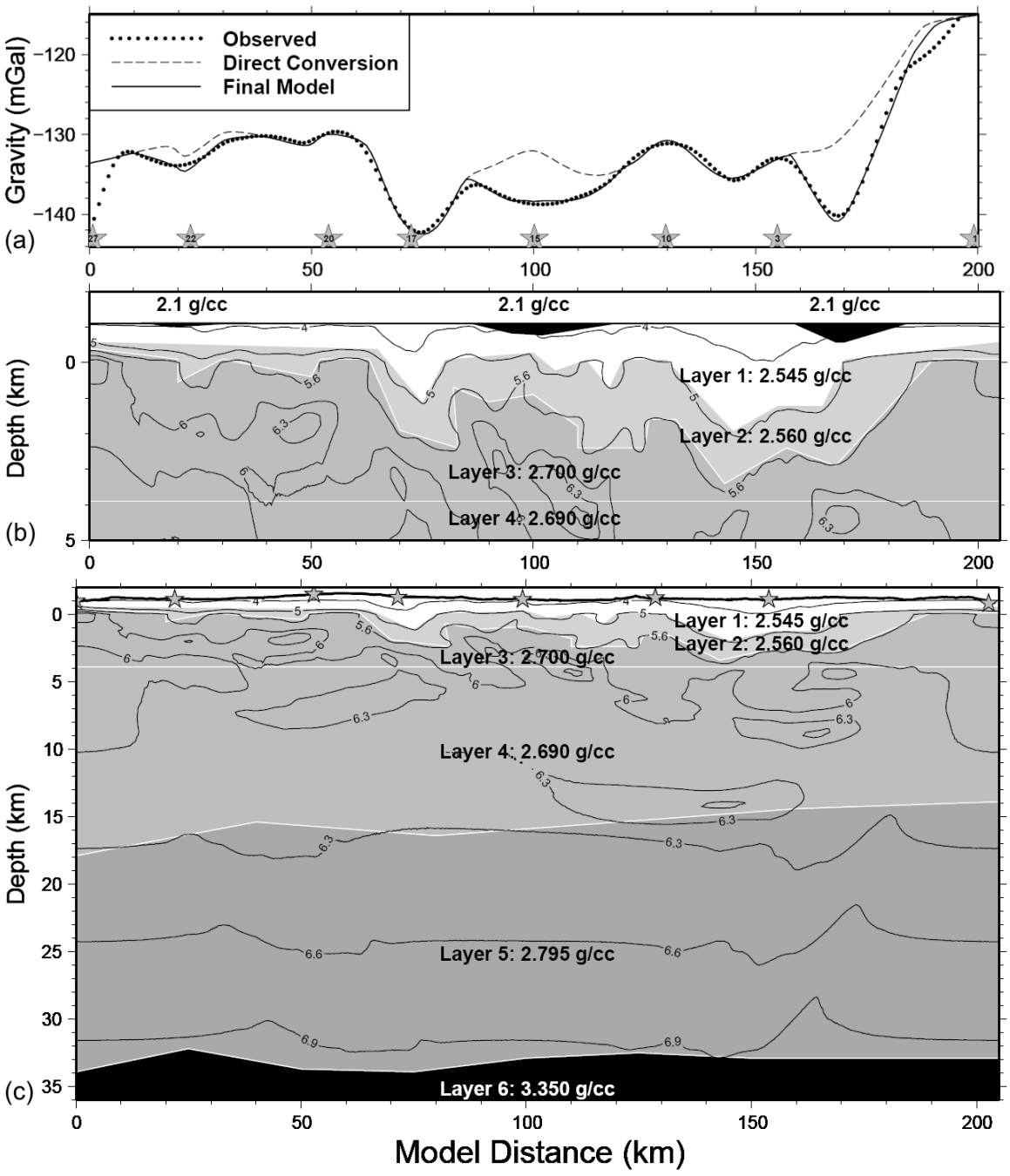

Figure 5.3. *(a)* Observed and synthetic gravity values. Measured gravity values are from NRCan's 2 km Bouguer grid. The direct conversion curve represents the synthetic gravity values produced by the five-layer direct density conversion of the velocity model, given in *(c)*. The final model provides a good fit to the observed data, improved with inclusion of three polygonal near-surface low density bodies illustrated as solid black polygons in *(b)* and inferred as Quaternary till. The boundary between Layer 5 and Layer 6 of the gravity model (shown in *(c)*) is defined by the Moho structure of the layered block velocity model, as derived from PmP and Pn arrivals. Density model block boundaries are indicated by thin white lines, while velocity contours used to generate the density model are shown beneath, in black.

5.3.2 Model perturbation

In order to obtain a better fit to the observed data in three particular regions of the poorest model fit (Fig. 5.3*a*), a few simple low density features were added to the near-surface of the direct conversion model to provide gravity lows (Fig. 5.3*b*). The features were given the general shape of an inverted triangle, with a density of 2.100 g/cm^3, consistent with that of Quaternary till deposits (Hayward and Calvert, 2010*a*). From 10-25 km model distance, a near-surface body with a maximum thickness of 120 m was inserted to effectively reduce the smallest of the three misfit regions. A wider and deeper anomaly was inserted between model distances of 85 km and 120 km, extending to 350 m depth, and improving fit to the region of model misfit at the center of the survey line. A 550 m thick low density volume was inserted between surface offsets of 158-185 km, improving model fit near the eastern end of the line (Fig. 5.3*a*).

Necessity of the 2.100 g/cm^3 density volumes is a by-product of the inherent non-uniqueness of the gravity model. The final model likely represents one out of many possible models which would provide equally satisfactory fits. Other acceptable models could utilize different layer thicknesses, or different density values also found within the acceptable range of the velocity-density relation curve of Barton (1986). However, the short wavelength of the features (<20 km) implies that the most likely source is quite shallow, e.g. perhaps variations in the upper 5 km of crust.

5.4 Interpretation

Following the final stages of forward modelling, the three near-surface anomalies were found to correspond almost exclusively to areas of mapped Quaternary surface cover (red receivers - Fig. 5.4). The features, although thin, can have a dramatic influence on gravity values due to their near-surface location, as observed by the significant improvement they provided to the model misfit (Fig. 5.3*a*).

5.4.1 Effect of shallow low velocity features on traveltime fit

The shallow low density features should have a nearly indistinguishable influence on recorded seismic traveltimes, since their thickness is a small fraction of the total distance that most of the (near vertically-incident) waves will have travelled. Although low velocity near-surface anomalies were not distinctly present in the final velocity model, features significantly smaller than the grid size (250 m) cannot be resolved, whether they represent low velocity Quaternary infill or high velocity surface volcanics.

To test the influence that the presence of such features would have on modelled traveltimes, three 2.50 km/s bodies spatially coincident with the density anomalies were introduced into the final layered block velocity model (Fig. 5.5). The three seismic low velocity zone thicknesses were 120 m, 350 m, and 550 m, respectively, equal to those of the density model anomalies. A velocity of 2.50 km/s lies near the middle of the range of acceptable velocity values for a modelled density of 2.100 g/cm^3 (Fig. 5.2), and is consistent with the velocity range of 2.00-2.80 km/s observed for Quaternary till (Hayward and Calvert, 2010*a*). Updated raypaths were traced and synthetic traveltimes

calculated, using the same iterative inversion scheme as for generation of the original block model.

The final layered block velocity model (Fig. 5.5) provided a decrease in RMS misfit, from 119 ms to 118 ms, and a negligible increase in χ^2, from 2.32 to 2.38, when allowed to iterate toward the best model with the anomalous bodies inserted into the starting model. This seemingly paradoxical change resulted from an improvement in fit to the greater-uncertainty PmP reflections coupled with a slight increase in first-arrival misfit. The near-surface low velocity zones remained present in the final model, indicating that the particular inversion scheme is not sensitive to features of such a thin vertical scale – they are not resolvable in the model. Rather, the compensation for their very minor slowing effect was dispersed elsewhere throughout the model. This allowed the model to reach an essentially equivalent level of fit, suggesting that the presence of such features in the actual subsurface would have a nearly indiscernible influence on the final velocity model, which represents an equally valid alternative model.

5.5 Comparison with previous gravity studies

Estimates of crustal thickness were made by Stacey (1973), based on Bouguer gravity values, with the crust-mantle boundary being located at a consistent ~34-35 km for the southern Intermontane Belt. Hayward and Calvert (2010*a*) compared Bouguer gravity maps to near-surface velocity models, observing that there was no direct relation between observed gravity and velocity anomalies. They concluded that the gravity anomalies are likely to be dominantly controlled by density heterogeneities at depths greater than the ~1 km penetration of the reflection data. This explanation aligns with our gravity modelling

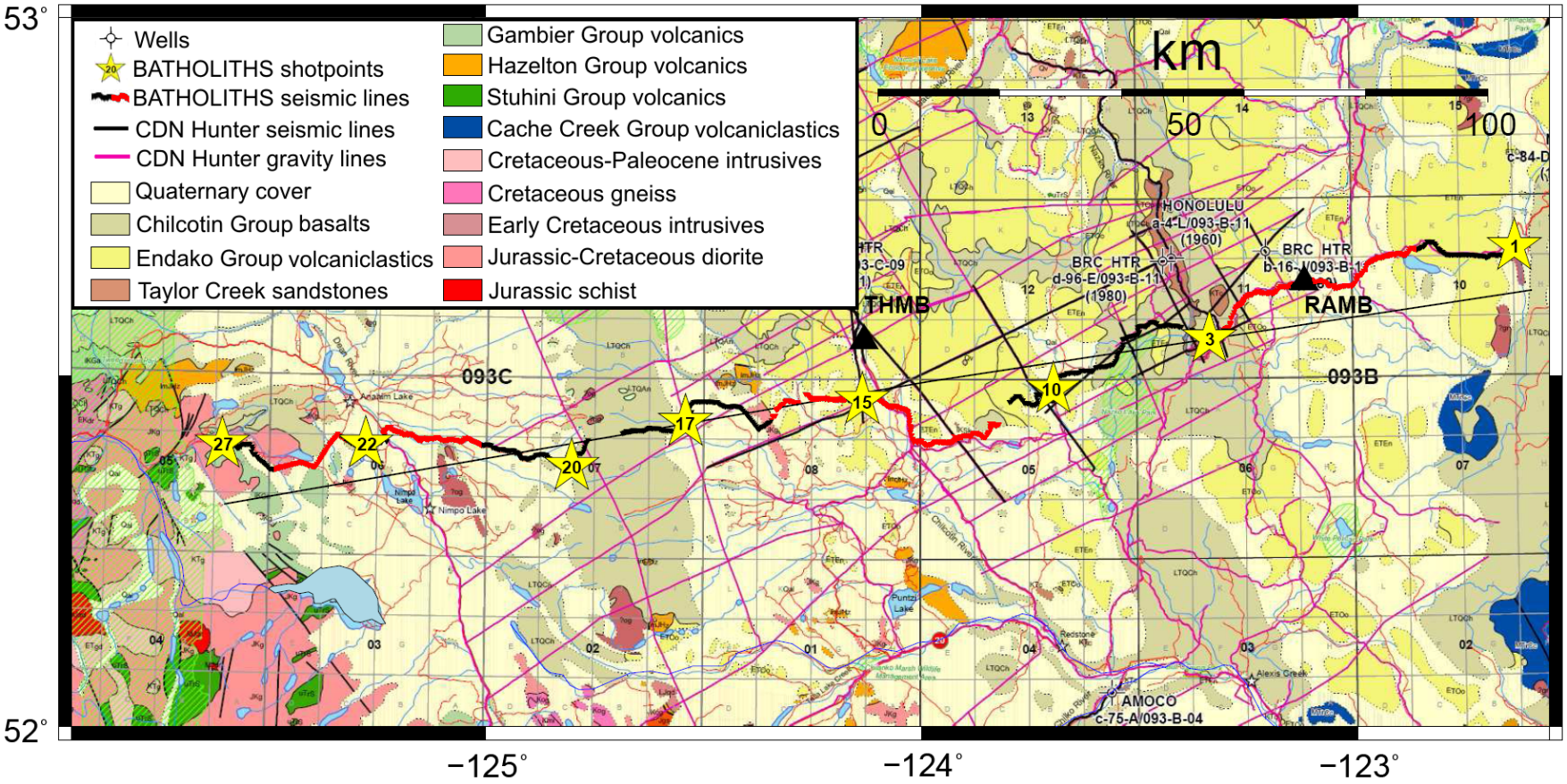

Figure 5.4. Comprehensive surface geology map including shotpoints and receiver lines of the BATHOLITHS*onland* survey (modified from Riddell, 2006). Red receiver line segments indicate locations of the three near-surface low density anomalies included in the gravity model (Figs. 5.3*b*), corresponding almost exclusively to Quaternary cover on the map.

and lithological interpretations, with the long-wavelength gravity anomalies resulting primarily from density contrasts within the entire upper ~5 km of crust. Lateral transitions from shallow volcanic arc terrane into thick sedimentary packages are inferred to be the primary control on Bouguer anomalies, rather than variations within the surface volcanic cover. Near-surface rocks of the Stikine Terrane (0-65 km) and Cache Creek Terrane (180-205 km) produce long-wavelength gravity highs, while the thickest part of the low density Nechako Basin (65-180 km) results in low gravity values (Figs. 4.4, 5.3). The interpreted basin extent corresponds exclusively to moderate-low observed gravity values (Fig. 5.1). Long wavelength Bouguer gravity anomalies are therefore useful in indicating the presence or absence of a thick sedimentary package.

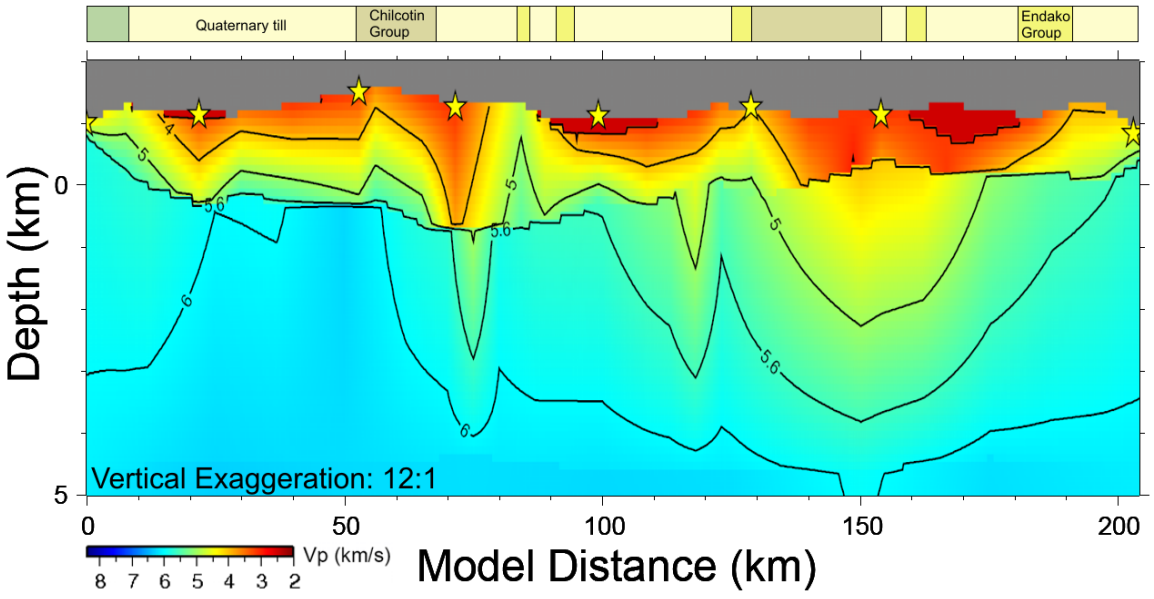

Figure 5.5. Sensitivity test measuring the influence of the near-surface low density bodies necessitated by the gravity model on the fit of the layered block velocity model. Three low velocity zones (2.5 km/s) with thicknesses of 120 m, 350 m, and 550 m are centered at model distances of 20 km, 100 km, and 170 km, respectively. Simplified surface geology is indicated along the top, with the low velocity zones coinciding almost exclusively with Quaternary till at the surface.

Chapter 6 Comparison with results from previous geophysical studies

Results of previous geophysical studies in the southern Intermontane Belt provide an array of complementary information about the thickness and extent of the Nechako Basin, lithospheric velocities, and the depth to the Moho discontinuity. A compilation in which the seismic velocity model is compared to a few of the most relevant datasets is illustrated in Figure 6.1.

6.1 Seismic reflection

In addition to refraction data, deep seismic reflection data were also gathered in the southern Canadian Cordillera during the LITHOPROBE program. The survey provided improved imaging of Moho structure across over 400 km of the Intermontane Belt (dataset "3" - Fig. 4.3). The crust-mantle transition was clearly evident on almost all LITHOPROBE reflection profiles, denoted by either a strong reflector, or a distinct transition from the high coherent reflectivity of the crust into the contrasting low reflectivity of the mantle below (Cook, 1995). A flat, subhorizontal Moho was imaged by Cook et al. (1992, 1995) beneath reflection Line 7 in the Intermontane Belt. Using crustal velocities from LITHOPROBE refraction studies, the Moho was found at relatively shallow depths of 31-33 km. This is in good agreement with the depths of 32-33 km, from the refraction model of Zelt et al. (1992) beneath Line 1 (Fig. 4.3).

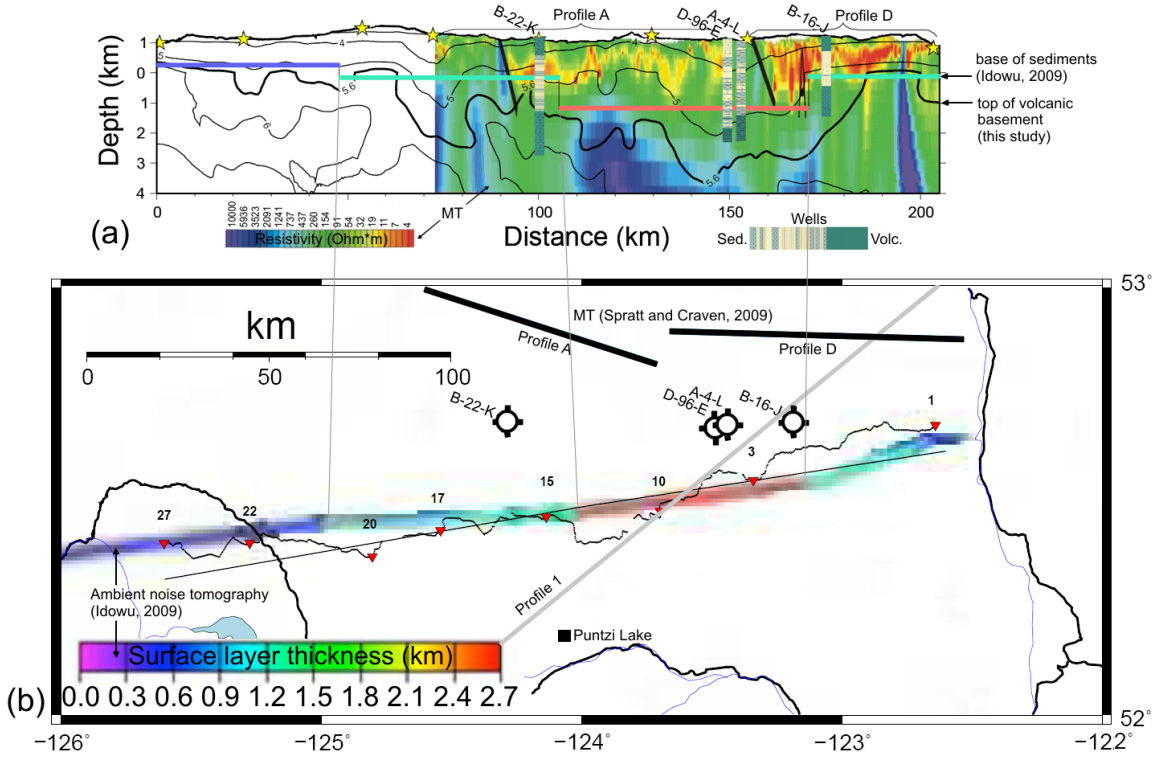

Figure 6.1. Integration of the final velocity model with several geophysical datasets. *(a)* Compilation of three datasets with the final velocity model (contoured). The resistivity profiles A and D of Spratt and Craven (2009) have been projected onto the eastern two-thirds of the survey line; note that the top of the purple high-resistivity region (interpreted as top of volcanic basement) corresponds well to the 5.6 km/s velocity contour representing the top of volcanic basement. The base of the surface sediment layer interpreted by Idowu (2009) is indicated by the overlain horizontal bars, with colours corresponding to the thicknesses detailed in *(b)*. Overlying both datasets are the four boreholes: B-22-K, D-96-E, A-4-L and B-16-J, projected approximately along strike and onto the survey line (Idowu, 2009; modified from Ferri and Riddell, 2006). Sedimentary and volcanic layers from the borehole data are represented by beige and green depth segments, respectively. *(b)* Map showing the location of the roughly coincident ambient noise passive seismic model of Idowu (2009), with interpreted surface layer thickness. Also included are the locations of the four nearest boreholes, and three magnetotelluric (MT) profiles of Spratt and Craven (2007, 2009) included in Figure 6.5.

More recently, 1300 line-kilometres of shallow seismic reflection data from the 1980's has been re-processed and re-interpreted in consideration of modern gravity and conductivity data. The dataset consists of ~35 lines across the Nechako basin, ranging in length from ~10-70 km (Fig. 6.2). The profiles were originally collected as part of a petroleum exploration program, and have since been supplemented by data from a 2008

vibroseis survey conducted by Geoscience BC, consisting of 330 line-kilometres over seven lines (Calvert et al., 2009). Hayward and Calvert (2008, 2009*a*, 2010*a*) inverted first-arrivals from the reflection shot-gathers in a 2D traveltime tomography. With the ray-tracing models constrained by borehole data, the depth of maximum ray density was found to correspond to the base of surface volcanics, usually at <300 m depth (Hayward and Calvert, 2009*c*). Surface velocities of ~2.5-4.0 km/s, averaging ~3.4 km/s (Hayward and Calvert, 2010*a*) are in agreement with our model. 1D velocity profiles for the upper kilometre of inter-basin boreholes B-22-K, A-4-L, and B-16-J are generally consistent with both the well log data and our velocity model (Fig. 4.1), reaching ~4.3-4.5 km/s at 1 km depth (Hayward and Calvert, 2010*a*). Using the modelled shallow velocity structure in conjunction with seismic reflection imaging, Hayward and Calvert (2009*b*) interpreted a Nechako Basin that is segmented into several sub-basins, divided by steep northwest and northeast-trending faults.

6.2 Passive source seismology

Seismic velocity modelling using earthquake-generated energy has been conducted extensively in the Western Canadian Cordillera. Wickens (1977) used regional surface wave traveltime data to produce shear-wave velocity profiles, several of which were located primarily within the Intermontane Belt. The profile closest to the BATHOLITHS*onland* line had a Moho depth of ~35 km. Slightly further to the south, a crustal thickness of ~33 km was interpreted. A line segment ~100-300 km to the north gave a Moho depth of ~20-24 km, contrasting with refraction studies but perhaps partially explained by the presence of a low velocity layer in the crust (Wickens, 1977).

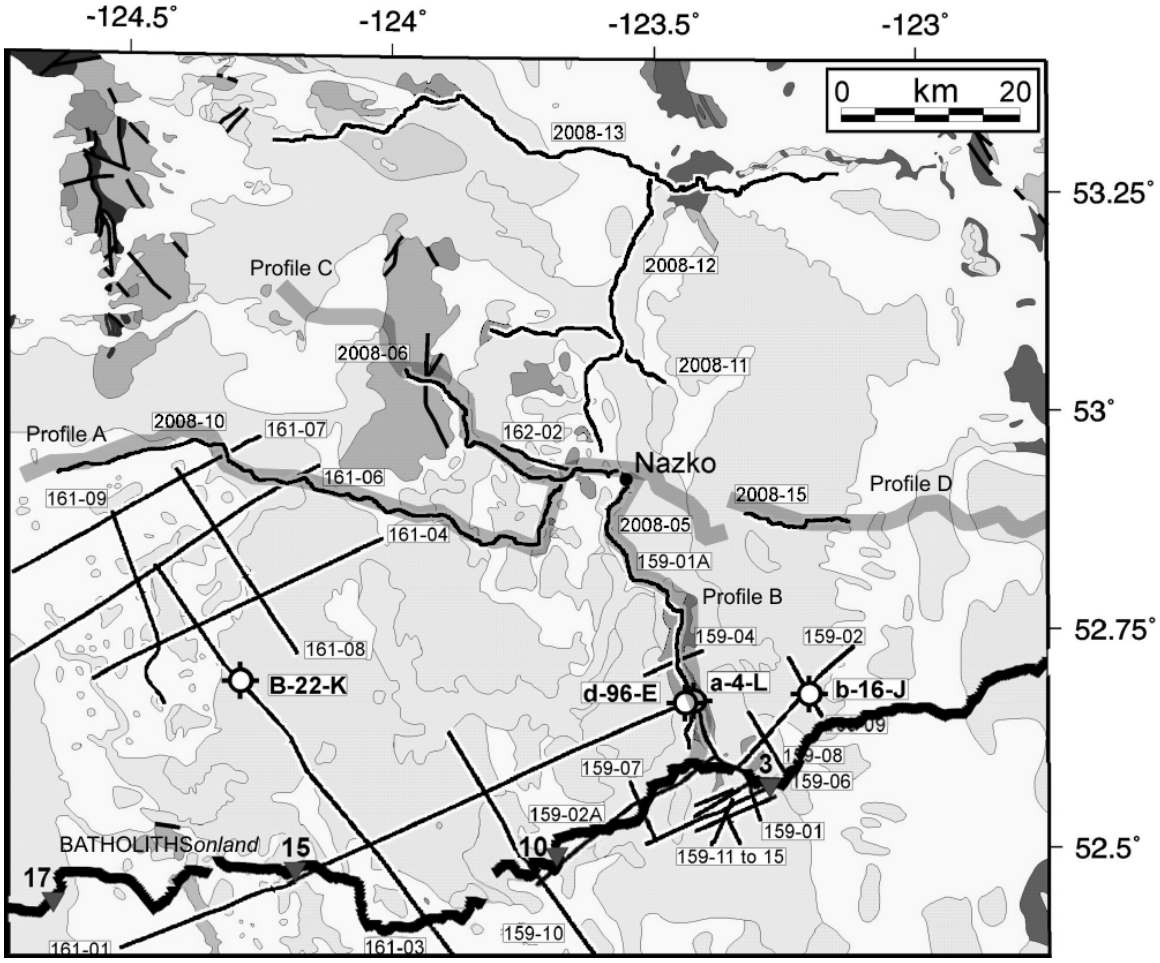

Figure 6.2. Map of seismic reflection and magnetotelluric experiments within the Nechako Basin (modified from Calvert et al., 2009). The location of the map is indicated in Figure 4.3. Black lines beginning with "159" or "161" represent reflection data collected by Canadian Hunter in the 1980's. Black lines beginning with 2008 represent reflection data collected by Geoscience BC (Calvert et al., 2009). Thick gray lines denoted Profile A, B, C, and D represent magnetotelluric data (Figs. 6.1, 6.5) gathered and interpreted by Spratt and Craven (2009). Part of the BATHOLITHS*onland* profile is shown in the south as a thick black line.

Recent teleseismic studies in the Nechako Basin utilized data from eight 3-component broadband seismic stations deployed for between 25 and 44 months from 2006 to 2009. In the peripheral southern part of the basin, ambient noise tomography suggested a sedimentary thickness of 1-1.5 km (Idowu, under review). Near the center of the basin, the sedimentary package thickness of ~2.5 km (Idowu, 2009) is consistent with

our interpretation and likely representative of averaging between sub-basins of varying thicknesses (Fig. 6.3*b*). From a 1D model of all paths within the Nechako Basin, Idowu (2009) interpreted a maximum basin depth of ~4.8 km, consistent with magnetotelluric results (Fig. 6.5). Ambient noise tomography along a profile roughly coincident with the BATHOLITHS*onland* receiver line (Fig. 6.1) yielded a surface volcanic thickness of ~500-600 m and a sedimentary layer thickness of ~1-2.7 km (Idowu et al., 2009). Most notably, a segment of prominently thickened sediment between stations THMB and RAMB (Fig. 2.1) projects onto the seismic line at model distances between 105 km and 170 km, corresponding to the thickest part of the basin in the seismic velocity model (Fig. 6.1 – red segment). The thinnest surface sediments were found at the western and eastern ends of the survey line (Fig. 6.1), corresponding to the shallowest volcanic basement and an absent or thin sedimentary layer in the velocity model.

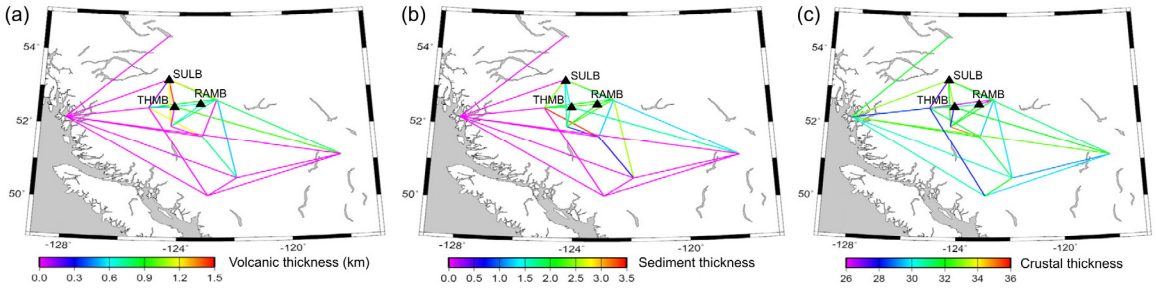

Figure 6.3. Tomographic velocity models of the Nechako Basin based on ambient seismic noise (modified from Idowu, 2009), including: *(a)* surface volcanic thickness, *(b)* sedimentary package thickness, and *(c)* crustal thickness.

A ~3 km thick sedimentary basin was supported by complementary receiver function modelling of data from the same receiver array (Kim et al., 2009*a*). Crustal thickness from the tomographic model was interpreted to be ~30.5-33.0 km along the nearly coincident line (Fig. 6.3*c*), averaging ~31 km for the entire Nechako Basin region

(Idowu, 2009). Our modelled Moho discontinuity at a depth of ~35 km compares favorably with the ~36 km result from site-specific modelling of receiver functions for station THMB, located 30 km north of shotpoint 15, and station SULB (Fig. 6.4), located ~65 km further north (Fig. 6.3 - Kim et al., 2009*b*).

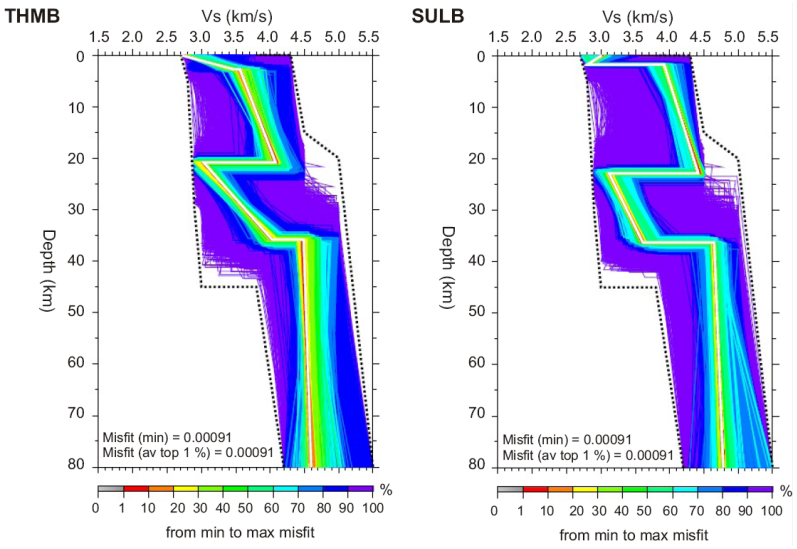

Figure 6.4. S-wave velocity profiles calculated from a single receiver function for stations THMB and SULB (Kim et al., 2009b). Both profiles include a low S-wave velocity zone in the lower crust, and ~36 km deep Moho. The locations of the two receiver stations are indicated on Figure. 2.1.

6.3 Magnetotelluric

Magnetotelluric data collected in the 1980's were re-interpreted by Spratt et al. (2006) using modern techniques. Surface volcanic rocks are interpreted to correspond to a shallow resistive layer, while high conductivity values delineate the subsurface extent of a ~4.5-5.0 km thick Nechako Basin sedimentary package (Spratt et al., 2006). The boundary between the conductive sediments and contrasting resistivity of underlying Cache Creek Terrane is especially evident, making magnetotelluric data highly useful for the mapping of sedimentary basin depth and extent. The correlation between high conductivity in the near surface and low observed gravity values likely results from the

high porosity of the sedimentary rock (Spratt et al., 2008). Notably, the southwestern boundary of the deep zone of high conductivity corresponding to the basin was located only ~10 km northwest of Puntzi Lake (Profile 1 - Figs. 6.1*b*, 6.5). This is considerably further east than the previously demarcated western boundary of the basin, and approximately consistent with our interpreted western edge between shotpoints 17 and 20, 40 km to the north in a roughly along-strike direction. Spratt et al. (2006) interpret the continuation of the basin for another ~30 km to the southwest, but at a greatly reduced thickness of <1 km, consistent with our interpretation west of shotpoint 20 (Fig. 4.4)

Having tested the usefulness of modern magnetotelluric methods in distinguishing between different lithologies, Spratt and Craven (2009) collected over 200 km of data along four profiles located 30-40 km north of the BATHOLITHS*onland* line (Fig. 6.2). Limited lateral extent of the thin resistive surface layer led to the conclusion that near-surface volcanics are either too thin to be detected by magnetotelluric methods, or less widespread than previously thought (Spratt and Craven, 2009). This is consistent with our velocity model, which was unable to clearly resolve a surface volcanic layer within the 250 m grid size. Analysis of the magnetotelluric data supported basin depths ranging from 1 to 3 km (Figs. 6.1*a*, 6.5), and thickening toward the eastern edge of the basin, as in our model (Spratt and Craven, 2009).

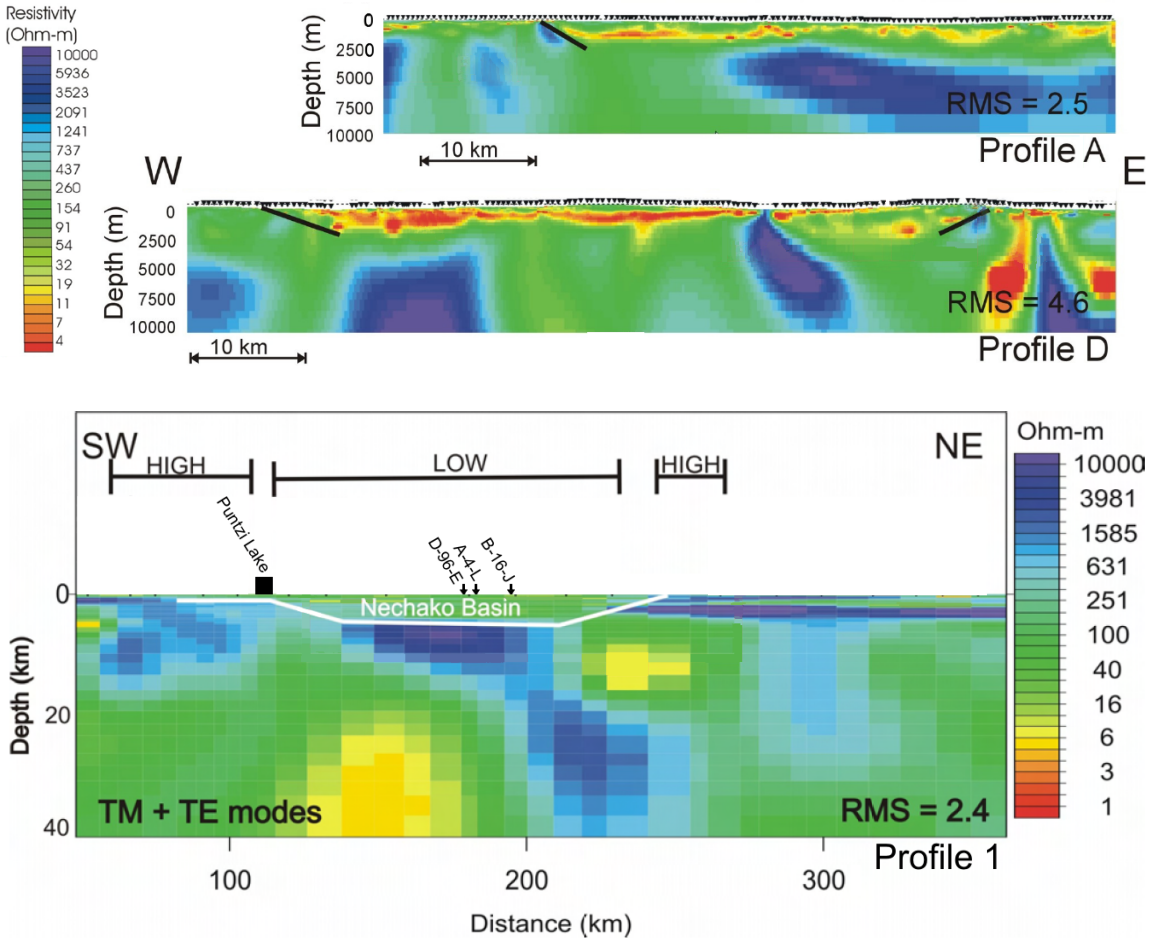

Figure 6.5. 2D resistivity profiles across the Nechako Basin (modified from Spratt and Craven, 2009; Spratt et al., 2007). Low resistivities in the upper ~5 km correspond to porous sedimentary or volcanic rock. Profile locations are included on figures 6.1 and 6.2. Projected borehole locations for wells given in Fig. 4.1 are labelled B-22-K, A-4-L, and B-16-J, also indicated on Fig. 6.1.

Chapter 7 Discussion and Conclusions

7.1 Velocity model

Using 3D first-arrival seismic tomography, a P-wave velocity model has been constructed which fits the data to within the estimated picking error, and provides the most featureless structure attainable. The Nechako Basin sedimentary rocks correspond to seismic velocities of 3.0-5.0 km/s and high velocity gradients. Velocities from 5.0-6.0 km/s may represent interbedded sedimentary and volcanic rocks formed at the early stages of basin formation. At greater depths below the basin, basement rocks of the Stikine terrane are identified by velocities greater than 6.0 km/s and small velocity gradients. Velocities are in good agreement with both borehole sonic logs and previous seismic-derived models in the area. Based on the known velocity range of proximal sedimentary rock and a previously measured and interpreted sedimentary package thickness of 1-3 km from borehole, magnetotelluric, and passive seismic data, the Nechako Sedimentary Basin is mapped as a 110 km-wide low velocity body composed of several 20-50 km-wide sub-basins of variable thickness, generally increasing eastward. The greatest sedimentary thicknesses are found on the western and eastern edges of the basin, which extends to depths of 2.5 km and 3.3 km, respectively.

Along the westernmost 65 km of the model, seismic velocities at depths greater than ~1 km are too high to correspond to sedimentary rock of the basin. The velocity profile in this western segment is similar to that of the eastern 35 km of the seismic line, believed to be located outside of the basin. The high velocities at depths of 1 km and deeper are interpreted to represent volcanic basement of the Stikine accreted arc in the

west and the Cache Creek accreted arc in the east. The P-wave seismic velocity model supports the interpretation that the western margin of the Nechako Basin – at least the portion of the basin of significant thickness – is located ~40 km east of its currently mapped location, reducing the total areal extent of the basin.

The Moho is mapped at a depth of 33.5-35 km, with no thinning at the base of the crust as would be expected for an extensional model of basin formation. Upper mantle velocities are 8.05-8.10 km/s, considered high for supporting the topographic elevations of the Interior Plateau.

7.2 Gravity model

The velocity-converted density models fit the Bouguer gravity data well except for two localized regions where the observed gravity was up to 10 mGal smaller than the modelled values. Gravity misfit between the observed and direct conversion synthetic datasets can be explained by the presence of three thin near-surface low density anomalies, potentially representing Quaternary infill. Although these bodies have a large influence on the measured gravity values, they minimally affect the seismic traveltime fit and are not resolvable by the layered block model inversion scheme. Insertion of thin low density bodies at the surface of the gravity model was sufficient to mitigate the observed misfit. It was demonstrated that the ray-tracing techniques employed in traveltime inversion and production of the velocity model would not be sensitive to such thin features, offering a possible explanation for their absence from the final velocity model. The net result of gravity modelling is additional support for the seismic velocity model.

7.3. Recommendations for future work

The next logical step proposed is integration of the results of this study with the velocity model of the full 400 km-long line. Doing so should confirm upper-crustal velocity structure along the eastern half of the survey line, while providing improved constraint for continued modelling of lower-crustal structure.

Qualitative analysis of trace amplitudes reveals a strong decay with offset for upper-crustal turning rays, suggesting a high velocity gradient within the first few kilometres of crust. Large-amplitude Moho reflections present in all shot gathers indicate that the crust-mantle transition is likely abrupt and representative of a large velocity discontinuity. By performing modelling of trace amplitudes, these observations could be quantified and used as added constraint to the traveltime inversion velocity model.

As part of the BATHOLITHS*onland* seismic survey, S-wave arrivals were also recorded at 2 km intervals. Velocity modelling of these data, in conjunction with receiver function-based S-wave velocity profiles, could potentially provide values of Poisson's ratio and lithological implications, improving delineation of the sedimentary sub-basins.

Two shotpoints and over 100 receivers located 150-280 km north of the western end of the survey line are intended to provide along-strike structural control. Analysis and modelling of these data may reveal information about the lithospheric velocity structure and character of the Moho to the north of the main BATHOLITHS*onland* survey line.

Bibliography

Andrews, G.D.M. and Russell, J.K. 2007. Mineral exploration potential beneath the Chilcotin Group (NTS 092O, P; 093A, B, C, F, G, J, K), south-central British Columbia: preliminary insights from volcanic facies analysis. Geological Fieldwork 2006, BC Ministry of Energy, Mines and Petroleum Resources, Paper 2007-1, pp. 229-238.

Barton, P.J. 1986. The relationship between seismic velocity and density in the continental crust – a useful constraint? Geophysical Journal of the Royal Astronomical Society. **87**: 195-208.

BC Ministry of Energy, Mines and Petroleum Resources. 2002. Nechako Basin: oil and gas opportunities in central British Columbia. BC Ministry of Energy, Mines and Petroleum Resources; information brochure.

Berry, M.J., and Forsyth, D.A. 1975. Structure of the Canadian Cordillera from Seismic Refraction and Other Data. Canadian Journal of Earth Sciences, **12**: 182-208.

Burianyk, M.J.A., and Kanasewich, E.R. 1995. Crustal velocity structure of the Omineca and Intermontane Belts, southeastern Canadian Cordillera. Journal of Geophysical Research, **100**: 15 303-15 316.

Calvert, A.J., Hayward, N., Smithyman, B.R., and Takam Takougang, E.M. 2009. Vibroseis survey acquisition in the central Nechako Basin, south-central British Columbia (parts of 093B, C, F, G). Geoscience BC Summary of Activities 2008, Geoscience BC, Report 2009-1, pp. 145-150.

Cassidy, J.F., Kim, H., Idowu, O., Kao, H., Dosso, S., Frederiksen, Mercier, J-P., Bostock, M., Frassetto, A., and Zandt, G.A. 2010. Passive source seismic studies of the sediments, crust and mantle beneath the Nechako Basin, south-central British Columbia (NTS92O, 093B, C, F, G). Geoscience BC Summary of Activities 2009, Geoscience BC, Report 2010-1, pp. 235-244.

Christensen, N.I., and Mooney, W.D. 1995. Seismic velocity structure and composition of the continental crust: A global view. Journal of Geophysical Research, **100**: 9761-9788.

Cook, F.A., Clowes, R.M., Snyder, D.B., van der Velden, A.J., Hall, K.W., Erdmer, P., and Evenchick, C.A. 2004. Precambrian crust beneath the Mesozoic northern Canadian Cordillera discovered by Lithoprobe seismic reflection profiling. Tectonics, **23**, TC2010, doi:10.1029/2002TC001412.

Cook, F., Varsek, J., Clowes, R., Kanasewich, E., Spencer, C., Parrish, R., Brown, R., Carr, S., Johnson, B., and Price, R. 1992. LITHOPROBE crustal reflection cross section of the southern Canadian Cordillera I: Foreland thrust and fold belt to Fraser River fault. Tectonics, **11**: 12-35.

Cooper, G.R.J. 2003. GRAV2DC for Windows V.2.10. School of Geosciences, University of the Witwatersrand, Johannesburg, South Africa.

Creaser, B., and Spence, G.D. 2005. Crustal structure across the northern Cordillera, Yukon Territory, from seismic wide-angle studies: Omineca Belt to Intermontane Belt. Canadian Journal of Earth Sciences, **42**: 1187-1203.

Cumming, W.B., Clowes, R.M., and Ellis, R.M. 1979. Crustal structure from a seismic refraction profile across southern British Columbia. Canadian Journal of Earth Sciences, **16**: 1024-1040.

Currie, C.A., and Hyndman, R.D. 2006. The thermal structure of subduction zone backarcs. Journal of Geophysical Research, **111**, B08404. doi:10.1029/2005JB004024.

Ducea, M.N. 2002. Constraints on the bulk composition and root foundering rates of continental arcs: A California arc perspective. Journal of Geophysical Research, **107**, B11, 2304, doi:10.1029/2001JB000643.

Evenchick, C.A., McMechan, M.E, McNicoll, V.J., and Carr, S.D. 2007. A synthesis of the Jurassic-Cretaceous tectonic evolution of the central and southeastern Canadian Cordillera: Exploring links across the orogen. *In* Whence the mountains? The contributions of Raymond A. Price. *Edited by* J.W. Sears, T.A. Harms, and C.A. Evenchick. Geological Society of America Special Papers, **433**(0): xi-xviii, pp. 117-146.

Ferri, F., and Riddell, J. 2006. The Nechako Basin Project: new insight from the southern Nechako Basin. Summary of Activities 2006, BC Ministry of Energy, Mines, and Petroleum Resources, pp. 89-124.

Gabrielse, H., Monger, J.W.H., Wheeler, J.O., and Yorath, C.J. 1991. Part A, Morphological belts, tectonic assemblages, and terranes. *In* Geology of the Cordilleran Orogen of Canada. *Edited by* H. Gabrielse and C.J. Yorath. Geological Survey of Canada, no. 4, pp. 329-371.

Geoscience BC. 2008. 2008 Nechako Seismic Survey: A regional survey in a volcanic-covered basin. Geoscience BC; information brochure.

Hammer, P.T.C., and Clowes, R.M. 2004. Accreted terranes of northwestern British Columbia, Canada: Lithospheric velocity structure and tectonics. Journal of Geophysical Research, **109**, B06305. doi:10.1029/2003JB002749.

Hannigan, P., Lee, P.J., Osadetz, K.G., Dietrich, J.R., and Olsen-Heise, K. 1994. Oil and gas resource potential of the Nechako-Chilcotin area of British Columbia (report). Petroleum Resources Subdivision, Institute of Sedimentary and Petroleum Geology – Geological Survey of Canada, pp. 130-167.

Harris, M.J., Symons, D.T.A., Hart, C.J.R., and Blackburn, W.H. 1998. Jurassic plate motions of the Stikine Terrane, southern Yukon: A paleomagnetic and geothermometric study of the Teslin Crossing Pluton (105E/7). Geological Fieldwork, Yukon Exploration and Geology 1998, pp. 155-156.

Hart, C.J.R. 1996. Geology and geochemistry of the Teslin Crossing Pluton: A gold-rich alkalic porphyry target. Yukon Exploration and Geology 1996, Exploration and Geological Services, Yukon, Indian and Northern Affairs Canada, pp. 131-137.

Hayes, B.J.R., Fattahi, S., and Hayes, M. 2003. The Nechako Basin – frontier potential close to home (abstract). Unpublished paper presented at Canadian Society of Petroleum Geologists 2003 Annual Convention. Available from http://www.cspg.org/conventions/abstracts/2002abstracts/extended/051S0118.pdf. [accessed May 2010].

Hayward, N. and Calvert, A.J. 2008. Structure of the south-eastern Nechako Basin, British Columbia: Results of seismic interpretation and first-arrival tomographic inversion (abstract). Unpublished paper presented at Canadian Society of Petroleum Geologists 2008 Annual Convention. Available from http://www.cseg.ca/conventions/abstracts/2008/2008abstracts/027.pdf. [accessed May 2010].

Hayward, N. and Calvert, A.J. 2009*a*. Eocene and Neogene volcanic rocks in the southeastern Nechako Basin, British Columbia: interpretation of the Canadian Hunter seismic reflection surveys using first-arrival tomography. Canadian Journal of Earth Sciences, **46**: 707-720.

Hayward, N. and Calvert, A.J. 2009*b*. Structure of the south-eastern Nechako Basin, British Columbia: Results of seismic interpretation and first-arrival tomographic inversion. GSC Pacific Seminars, Pacific Geoscience Centre, Sidney, BC, February 26, 2009 (Powerpoint presentation).

Hayward, N. and Calvert, A.J. 2009*c*. Near-surface volcanic rocks in the SE Nechako Basin, BC: Results of interpretation of seismic data using first-arrival tomographic inversion. Mineral Exploration RoundUp Meeting, Vancouver, BC, January 26-29, 2009 (poster).

Hayward, N. and Calvert, A.J. 2010*a*. Near-surface volcanic rocks in the southeastern Nechako Basin, south-central British Columbia (parts of NTS 092N, O, 093B, C): interpretation of the Canadian Hunter seismic reflection surveys and first-arrival tomographic inversion. Geoscience BC Summary of Activities 2009, Geoscience BC, Report 2010-1, pp. 203-226.

Hayward, N. and Calvert, A.J. 2010*b*. Structure of the South-eastern Nechako Basin, British Columbia: Interpretation of the Canadian Hunter Seismic Reflection Surveys. Canadian Journal of Earth Sciences: Pine Beetle Special Volume. In review.

Hole, J.A., and Zelt, B.C. 1995. Three-dimensional finite-difference reflection travel times. Geophysical Journal International, **121**: 427-434.

Idowu, O. 2009. Surface wave tomography of the Nechako Basin, British Columbia, using ambient seismic noise. MSc thesis, University of Manitoba, Winnipeg, Manitoba.

Idowu, O.A., Frederiksen, A.W., and Cassidy, J. 2009. Seismic tomography of the Nechako Basin, British Columbia, using ambient seismic noise. Mineral Exploration RoundUp Meeting, Vancouver, BC, January 26-29, 2009 (poster).

Jackson, J.L., Gehrels, G.E., Patchett, P.J., and Mihalynuk, M.G. 1991. Stratigraphic and isotopic link between the northern Stikine terrane and an ancient continental margin assemblage, Canadian Cordillera. Geology, **19**: 1177-1180.

Johnston, S.T., and Borel, G.D. 2007. The odyssey of the Cache Creek terrane, Canadian Cordillera: Implications for accretionary orogens, tectonic setting of Panthalassa, the Pacific superwell, and break-up of Pangea. Earth and Planetary Science Letters, **253**: 415-428.

Kim, H-S., Cassidy, J.F., Dosso, S.E., and Kao, H. 2009*a*. Mapping the sedimentary rocks and crustal structure of the Nechako Basin, British Columbia (NTS 092N, O, 093B, C, F, G), using teleseismic receiver functions. Geoscience BC Summary of Activities 2008, Geoscience BC, Report 2009-1, pp. 163-170.

Kim, H-S., Cassidy, J.F., Dosso, S.E., and Kao, H. 2009*b*. Mapping crustal structures of the Nechako Basin using teleseismic receiver functions. Mineral Exploration RoundUp Meeting, Vancouver, BC, January 26-29, 2009 (poster).

Lowe, C., Horner, R.B., Mortensen, J.K., Johnston, S.T., Roots, C.F. 1994. New geophysical data from the northern Cordillera: preliminary interpretations and implications for the tectonics and deep geology. Canadian Journal of Earth Sciences, **31**: 891-904.

MacIntyre, D.G., Villeneuve, M.E., and Schiarizza, P. 2001. Timing and tectonic setting of Stikine Terrane magmatism, Babine-Takla lakes area, central British Columbia. Canadian Journal of Earth Sciences, **38**: 579-601.

Monger, J.W.H., Price, R.A., and Tempelman-Kluit, D.J. 1982. Tectonic accretion and the origin of the two major metamorphic and plutonic welts in the Canadian Cordillera. Geology, **10**: 70-75.

Osadetz, K., Ferri, F., Stasiuk, L., Reyes, J., and Thorsteinsson, E. 2007. Indications for active petroleum systems in Nechako Basin, Intermontane Belt. Intermontane Basin Workshop 2007 (Powerpoint presentation).

Ramachandran, K., Dosso, S.E., Zelt, C.A., Spence, G.D., Hyndman, R.D., and Brocher, T.M. 2004. Upper crustal structure of southwestern British Columbia from the 1998 Seismic Hazards Investigation in Puget Sound. Journal of Geophysical Research, **109**, B09303. doi:10.1029/2003JB002826. Available from http://www.agu.org/pubs/crossref/2004/2003JB002826.shtml. [accessed June 2010].

Riddell, J.M. (compiler). 2006. Geology of the southern Nechako Basin, NTS 92N, 92O, 93B, 93C, 93F, 93G. BC Ministry of Energy and Mines and Petroleum Resources, Petroleum Geology Map 2006-1, 3 sheets, 1:400 000 scale.

Riddell, J. 2009. Evaluation of potential petroleum systems in the Nechako Basin. Geoscience Reports 2009, BC Ministry of Energy, Mines and Petroleum Resources, pp. 53-63.

Rohr, K., and Dietrich, J.R. 1992. Strike-slip tectonics and development of the Tertiary Queen Charlotte Basin, offshore western Canada: evidence from seismic reflection data. Basin Research, **4**: 1-19.

Smithyman, B.R., and Clowes, R.M. 2010. Improved near-surface velocity models from the Nechako Basin seismic survey, south-central British Columbia (parts of NTS 093B, C, F, G), part 1: traveltime inversions. Geoscience BC Summary of Activities 2009, Geoscience BC, Report 2010-1, pp. 227-234.

Spence, G.D., and McLean, N.A. 1998. Crustal seismic velocity and density structure of the Intermontane and Coast belts, southwestern Cordillera. Canadian Journal of Earth Sciences, **35**: 1362-1379.

Spratt, J.E. and Craven, J.A. 2009. Preliminary images of the conductivity structure of the Nechako Basin, south-central British Columbia (NTS 092N, O, 093B, C, F, G) from magnetotelluric methods. Geoscience BC Summary of Activities 2008, Geoscience BC, Report 2009-1, pp. 175-182.

Spratt, J.E., Craven, J., Jones, A.G., Ferri, F., and Riddell, J. 2007. Utility of magnetotelluric data in unravelling the stratigraphic-structural framework of the Nechako Basin (NTS 092N; 093C, B, G, H), south-central British Columbia, from a re-analysis of 20-year-old data. Geological Fieldwork 2006, Ministry of Energy, Mines and Petroleum Resources, Paper 2007-1, pp. 395-404.

Spratt, J., Craven, J., Riddell, J., and Ferri, F. 2008. Initial results of a test survey in the Nechako Basin, B.C., designed to determine the usefulness of the magnetotelluric method in oil and gas exploration. Interior Basins Workshop 2008 (Powerpoint presentation).

Stacey, R.A. 1973. Gravity anomalies, crustal structure and plate tectonics in the Canadian Cordillera. Canadian Journal of Earth Sciences, **10**: 615-628.

Tempelman-Kluit, D.J., and Currie, R.G. 1978. Reconnaissance rock geochemistry of Aishihik Lake, Snag and Stewart River map areas in the Yukon Crystalline Terrane. Geological Survey of Canada, Paper 77-8.

Van Wagoner, T.M., Crosson, R.S., Creager, K.C., Medema, G., Preston, L., Symons, N.P., and Brocher, T.M. 2002. Crustal structure and relocated earthquakes in the Puget Lowland, Washington, from high-resolution seismic tomography. Journal of Geophysical Research, **107**, B12, 2381. doi:10.1029/2001JB000710.

Vidale, J.E. 1988. Finite-difference calculation of travel times. Bulletin of the Seismological Society of America, **78**: 2062-2076.

Wang, K., Hole, J.A., Stephenson, A.L., Spence, G.D., Miller, K.C., Harder, S.H., Kaip, G.M., and Clowes, R.M. 2010. Controlled-source seismic investigation of the generation and collapse of a batholith complex, Coast Mountains, Western Canada. IRIS Workshop (poster).

Welford, J.K., Clowes, R.M., Ellis, R.M., Spence, G.D., Asudeh, I., and Hajnal, Z. 2001. Lithospheric structure across the craton – Cordilleran transition of northeastern British Columbia. Canadian Journal of Earth Sciences, **38**: 1169-1189.

Wheeler, J.O., Brookfield, A.J., Gabrielse, H., Monger, J.W.H., Tipper, H.W., and Woodsworth, G.J. 1991. Terrane map of the Canadian Cordillera. Geological Survey of Canada, Map 1713, 1:1 000 000 scale.

White, W.R.H., Bone, M.N., and Milne, W.G. 1968. Seismic refraction surveys in British Columbia – a preliminary interpretation. American Geophysical Union, Geophysical Monograph, **12**: 81-93.

Wickens, A.J. 1977. The upper mantle of southern British Columbia. Canadian Journal of Earth Sciences, **14**: 1100-1115.

Zandt, G., Gilbert, H., Owens, T.J., Ducea, M., Saleeby, J., and Jones, C.H. 2004. Active foundering of a continental arc root beneath the southern Sierra Nevada in California. Nature, **431**: 41-46.

Zelt, B.C., Clowes, R.M., Ellis, R.M., and Hole, J.A. 1996. Inversion of three-dimensional wide-angle seismic data from the southwestern Canadian Cordillera. Journal of Geophysical Research, **101**: 8503-8529.

Zelt, B.C., Ellis, R.M., Clowes, R.M., Kanasewich, E.R., Asudeh, I., Luetgert, J.H., Hajnal, Z., Ikami, A., Spence, G.D., and Hyndman, R.D. 1992. Crust and upper mantle velocity structure of the Intermontane belt, southern Canadian Cordillera. Canadian Journal of Earth Sciences, **29**: 1530-1548.

Zelt, B.C., Ellis, R.M., Zelt, C.A., Hyndman, R.D., Lowe, C., Spence, G.D., and Fisher, M.A. 2001. Three dimensional crustal velocity structure beneath the Strait of Georgia, British Columbia. Geophysical Journal International, **144**: 695-712.

Zelt, C.A. and Barton, P.J. 1998. Three-dimensional seismic refraction tomography: A comparison of two methods applied to data from the Faeroe Basin. Journal of Geophysical Research, **103**: 7187-7210.

Zelt, C.A. and Smith, R.B. 1992. Seismic traveltime inversion for 2-D crustal velocity structure. Geophysical Journal International, **108**: 16-34.